Characterization of the Vacuum Assisted Resin Transfer Molding Process for Fabrication of Aerospace Composites

Brian W. Grimsley

Thesis Submitted to the Faculty of the
Virginia Polytechnic Institute and State University
In partial fulfillment of the requirements for the degree of

Master of Science
In
Materials Science and Engineering

Dr. A. C. Loos
Dr. B. J. Love
Dr. M. W. Hyer

November 29, 2005
Blacksburg, Virginia

Keywords: VARTM, Compaction, Infusion, Permeability, Carbon-Fiber, Epoxy-Resin

Characterization of the Vacuum Assisted Resin Transfer Molding Process for Fabrication of Aerospace Composites

Brian W. Grimsley

Abstract

This work was performed under a cooporative research effort sponsored by the National Aeronautics and Space Administration (NASA) in conjunction with the aerospace industry and acedemia. One of the primary goals of NASA is to improve the safety and affordability of commercial air flight. Part of this goal includes research to reduce fuel consumption by developing lightweight carbon fiber, polymer matrix composites to replace existing metallic airframe structure. In the Twenty-first Aircraft Technology Program (TCAT) efforts were focused on developing novel processing methods to fabricate tailored composite airframe structure. The Vacuum Assisted Resin Transfer Molding (VARTM) processing technique offers a safer, more affordable alternative to manufacture large scale composite fuselages and wing structures. Vacuum assisted resin transfer molding is an infusion process originally developed for manufacturing of composites in the marine industry. The process is a variation of Resin Transfer Molding (RTM), where the rigid matched metal tooling is replaced on one side with a flexible vacuum bag. The entire process, including infusion and consolidation of the part, occurs at atmospheric pressure (101.5 kPa). High-performance composites with fiber volumes in the range of 45% to 50% can be achieved without the use of an autoclave. The main focus of the VARTM process development effort was to determine the feasibility of manufacturing aerospace quality composites with fiber volume fractions approaching 60%.

A science-based approach was taken, utilizing finite element process models to characterize and develop a full understanding of the VARTM infusion process as well as the interaction of the constituent materials. Achieving aerospace quality composites requires further development not only of the VARTM process, but also of the matrix resins and fiber preforms. The present work includes an investigation of recently developed epoxy matrix resins, including the characterization of the resin cure kinetics and flow behaviors. Two different fiber preform architectures were characterized to determine the response to compaction under VARTM conditions including a study to determine the effect of thickness on maximum achievable fiber volume fraction. Experiments were also conducted to determine the permeabilities of these preforms under VARTM flow conditions. Both the compaction response and the permeabilities of the preforms were fit to empirical models which can be used as input for future work to simulate VARTM infusion using process models.

Actual infusion experiments of these two types preforms were conducted using instrumented tools to determine the pressures and displacements that occur during VARTM infiltration. Flow experiments on glass tooling determined the fill-times and flow front evolution of preform specimens of various thicknesses. The results of these experiments can be used as validation of process model infusion simulations and to verify the compaction and permeability empirical models. Panels were infused with newly developed epoxy resins, cured and sectioned to determine final fiber volume fractions and part quality in an effort to verify both the infusion and compaction experimental data.

The preforms characterized were found to have both elastic and inelastic compression response. The maximum fiber volume fraction of the knitted fabrics was dependent on the amount of stacks in the preform specimen. This relationship was found in the determination of the Darcy permeabilities of the preforms. The results of the characterization of the two epoxy resin systems the show that the two resins have similar minimum viscosities but significantly different curing behaviors. Characterization of the VARTM process resulted in different infusion responses in the two preform specimens investigated. The response of the saturated preform to a recompaction after infusion indicated that a significant portion of the

fiber volume lost during infusion could be recovered. Fiber volume and void-content analysis of flat composite panels fabricated in VARTM using the characterized resins and preforms resulted in void-free parts with fiber volumes over 58%. Results in the idealized compaction tests indicated fiber volumes as high as 60% were achievable with the knitted fabric. The work over the presented here has led to a more complete understanding of the VARTM process but also led to more questions concerning its feasibility as an aerospace composite manufacturing technique.

I dedicate this work to my wife, Stacey, and my parents, Mike and Bobbi, for their unwavering support.

Acknowledgements

I express my appreciation to Professor Loos for his guidance and support during my thesis research efforts. I also thank Professor Hyer and Professor Love for donating their time and expertise in reviewing my thesis.

I thank Professor Hubert at McGill University for his assistance and guidance with our early efforts to develop VARTM process characterization techniques at NASA.

I also acknowledge the tremendous amount of support given to me over the last eight years through my undergraduate and graduate work by the researchers and technical staff of the Advanced Materials and Processing Branch at NASA Langley Research Center. During my tenure at NASA I worked on various projects which afforded me the oppurtunity to collaborate with many of the research staff. I hold them all in the highest regard but I especially wish to thank Sean Britton, Bert Cano, Tan Hou, Brian Jensen and Erik Weiser for their special attention during my development as an engineer.

As a final note, I express my gratitude to Dr. Norm Johnson and Dr. Joe Marchello who recognized my potential and hired me into NASA as a student grantee.

Contents

List of Figures

.

List of Tables

Chapter 1

Introduction

Continuous-fiber reinforced, polymer matrix composites (CFRP) are becoming the materials of choice to replace metals and other materials in many structural applications. First incorporated in large scale applications during WWII by the military, the yearly global use of composites in manufacturing has grown from 158,000 metric tons in 1960 to 6.1 million metric tons in 2004 [1]. A CFRP includes the continuous, reinforcing fiber which is commonly comprised of glass, carbon/graphite, boron, or aramid material. The fibers are embedded in a polymer resin matrix. The matrix can include either thermoplastic or thermosetting polymer resins. The fibers bear the majority of the structural loads carried by the composite. The resin acts to transmit these loads to the fibers and protect the fibers from the environment [2]. The decision to introduce or replace existing materials with composites is influenced by several factors, including material property advantages, advanced design capability, improvement over existing technology and cost. CFRP's have a high strength-to-weight ratio when compared to commonly used metals such as aluminum or steel. CFRP's by their nature are anisotropic which can be advantagous in design of certain structures. In addition, the ability to easily form complex shapes using CFRP materials further decreases cost when compared to metal structures which must be either machined or cast at high temperatures. Today, CFRP's find application in the fabrication of recreational products such as skis, snowboards and bicycles. Almost all tennis rackets and many golf club shafts

are produced using high performance carbon fiber composites. The bike frame that Lance Armstrong rode to his sixth Tour de France victory was made almost entirely of carbon fiber CFRP materials. The OCLV 55™ composite frame weighs approximately 0.907 kg versus an estimated 1.360-1.587 kg if the frame were fabricated using an aluminum alloy [3].

The hulls and decks of most commercially available recreational boats and many luxury yachts are fabricated using glass CFRP materials. The use of these materials offers tremendous cost savings in production labor versus fabrication of these structures using conventional materials such as wood or steel. In addition, the final product is much more durable when considering the effects of corrosion from long term exposure to salt water. Since the 1970s, the U.S. Navy has used fiber-glass composites to fabricate the hulls of mine sweepers due to the advantages of glass CFRP non-magnetic properties. With new and different threats emerging in the 21st century, naval architects are turning to CFRP material for the design of light-weight, stealthy attack vessels. The Kokums Karlskrona Shipyard in Sweden recently delivered two Visby-class ships built entirely of stuctural carbon CFRP materials [4]. The natural damping and insulating properties of the CFRP materials make these vessels more difficult to detect with sonar.

Integration of composites to produce automotive parts has grown steadily sinced the late 1970s. With the future of petroleum resources uncertain, consumers will eventually demand more fuel-efficient vehicles. Concept vehicles which meet these demands have entire inner and outer frames built of lightweight, strong carbon CFRP materials. Many CFRP components such as interior frames, exterior panels, towing packages, etc. are currently in production and in the market. New Toyota and Honda truck beds are made from CFRP materials as is the rear decklid inner of the Ford 2005 GT. The part weighs half that of the aluminum part and saves Ford almost $3 million in tooling costs [5]. The U.S Army has incorporated CFRP materials including carbon, boron, and aramid fibers in many of its ground assault and transport vehicles [6]. These materials become an integral part of armor design and offer advantages over other materials due to the ease of in-field repair applications.

The lightweight, stiff characteristics of CFRP materials also have tremendous potential for cost savings in the fabrication of aerospace vehicles. These materials have found application mostly in the production of small, private airplanes comprising general aviation, such as Lancair's Columbia 400, a single-engine four seater with 100% CFRP airframe. The U.S. military has capitilized on the strength-to-weight advantages of CFRP material in the fabrication of attack fighters. The exterior skin of the airframe structure of both the F-22 Raptor and the F-35 Joint Strike Fighter are produced by Lockheed-Martin using CFRP materials [7]. Design and production of future unmanned aerial vehicles (UAV) using lightweight materials ensure a future growth market for advanced CFRP materials. The use of CFRP material for manufacture of large airframe structures associated with commercial jetliners has still not met its potential. Problems associated with safety and reliability of CFRP material versus existing FAA approved metallic structure and production/fabrication costs associated with fabrication of such large-scale CFRP structures have, until recently, restricted their use.

The National Aeronautics and Space Administration (NASA) at the Langley Research Center has partnered with industry and academia to reduce the cost and improve the safety of commercial air travel. Since the mid 1970s a major focus of that effort has been to develop CFRP materials to replace the aluminum used in highly loaded components such as fuselage and wing structures. In an early study to optimize the design of an aircraft built from CFRP materials, it was concluded by both analytical and experimental methods that up to a 50% weight savings could be realized by replacing aluminum in the structure [8].

Boeing Aerospace and Airbus Aerospace have incorporated stuctural composites in the airframe of two commercial jetliners. The Boeing 777 has carbon fiber reinforced polymer matrix composites located in the vertical and horizontal tail sections. The Airbus A300-310 also has carbon fiber CFRP composites as primary structure in the jet's vertical tail section. The structural composite parts on each of these jetliners are processed by curing under elevated temperature and pressure in a pressure chamber, or autoclave.

During the early to mid 90s NASA partnered with industry to focus research on the development of High Speed Civil Transport (HSCT) built largely from CFRP materials. The

proposed commercial jetliner would be capable of carrying up to 300 passengers at speeds of Mach 2.4 at altitudes of 18.3 km for 9,260 km [9]. The High Speed Research (HSR) program at NASA during this time period developed high-temperature polyimide resins that could perform under the environmental demands a high speed composite airframe would experience during flight. The research effort was successful in developing pre-impregnated carbon fiber tapes (prepreg) containing these high performance polyimide resins. To process the tapes into multi-layered, multi-axial composite structure with the desired properties, the material had to be processed at high temperatures (>370 C) and pressures up to 1.03 MPa. Well consolidated, high fiber volume (60 %), low void content composites were developed that met the HSCT performance requirements [10]. However, Boeing determined that the market demand for such a vehicle was not sufficient to support the expense of fabrication. The major portion of this expense was in the infrastructure required to process these materials in autoclaves during fabrication of the large wing and fuselage structures.

NASA's composites research effort during the 90s, the Advanced Composites Technology (ACT) program, began to address the cost factors inherent to fabrication of large-scale, high performance composites. In this program a full-scale wing box was fabricated using a recently developed preform stitching technology and a new processing method called resin film infusion (RFI). In this process a dry fiber preform is infused with a molten resin, consolidated and cured all in one step. Dry preform in the form of either woven or non-woven mats is combined with films or sheets of resin in a vaccum bag. The bagged part is placed in an autoclave where heat is applied to reduce the viscosity of the resin so that it will flow under presure to fill the dry fibers. While flow and consolidation still require pressure supplied by an autoclave, the RFI technique eliminates the expense involved in the extra step to process the prepreg tape. The ACT program culminated in the fabrication of the wing at Boeing, Long Beach and a very successful test of the full-scale wing at NASA [11]. The research concluded that incorporating stitched/RFI wing technology in future aircraft would reduce weight by up to 25% and, depending on the size of the aircraft, a 4 to 14% reduction in fuel consumption [12].

During the last four years NASA has funded advancements in CFRP technology for application on the next generation of commercial jetliners. Under the Twenty-First Century Aircraft Technology program (TCAT), work has focused on developing an aircraft wing that will passively morph during takeoff and decent. The idea is to tailor the arrangement of the continuous carbon fibers so that the wing can adjust its load carrying capabilities to meet the changing stresses encountered during flight. Finite element analysis (FEA) was performed to determine the ideal fiber architecture to allow a wing to passively morph. Other efforts focused on the development of the constitutive materials and processing methods to facilitate a tailored structural composite. Ideally the composite would allow for the highest strength at the lowest weight and lowest manufacturing cost to the commercial fabricator. With this in mind efforts were focused to develop a CFRP processing method to fabricate aerospace quality structural components without the use of an autoclave.

Resin infusion processes such as RFI and resin transfer molding (RTM) have demonstrated capabilities to manufacture high quality, high performance composite structural components. As previously described, RFI typically requires an autoclave to achieve the high fiber volumes necessary for aerospace components. The RTM process, depicted in Figure 1.1, has been in use for fabrication of structural components since the late seventies. It involves infusion of a dry fiber preform held within a rigid metal mold. High performance composites parts of just about any shape and configuration can be fabricated by RTM without the use of an autoclave. The desired preform fiber volume is achieved by placing a measured amount of woven fabric in the mold and mechanically fastening the top portion of the rigid mold to the bottom portion. This usually results in a preform with low permeability and therefore the resin must be injected into the mold under elevated pressures using some type of hydraulic or electromotive piston injector. A large amount of effort has been focused in the past on perfecting the method including fiber and resin characterization as well as part-fill time prediction using mathamatical models in FEA. While RTM is well suited for the manufacturer of smaller components such as aircraft cargo doors, the costs assocated with matched metal tooling make it less attractive for fabrication of larger scale components such as fuselage and wing structure.

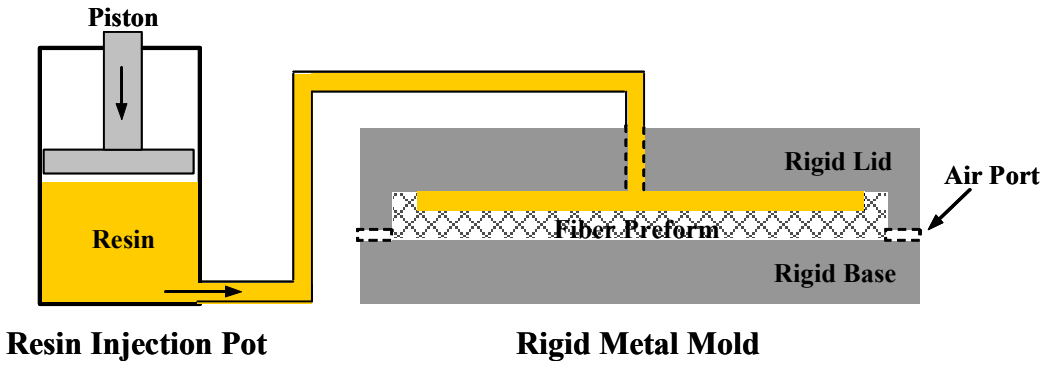

Figure 1.1: Resin Transfer Molding.

Vacuum assisted resin transfer molding (VARTM) is a variation of the RTM infusion process. Originally, a vacuum was introduced to the RTM mold to lessen the required injection pressure and remove air voids in the final processed composite laminate [13]. The process was developed further by marine composite hull manufacturers at Seemanns Composite Corporation by eliminating the rigid top portion of the mold and replacing it with a flexible polymer vacuum bag. The woven preform could be placed on a rigid tool having the shape of the desired composite part. The fabric is sealed to the tool with the vacuum bag and an adhesive tape. The bagged part is then evacuated via a vacuum port which protrudes from the sealed bag. A typical VARTM lay-up is shown in Figure 1.2.

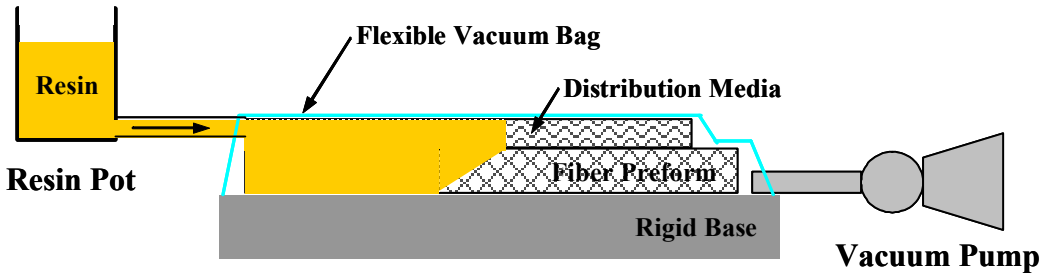

Figure 1.2: Vacuum Assisted Resin Transfer Molding (VARTM).

With the part fully evacuated, the compaction pressure on the preform is approximately 1 atm. Using low viscosity resins, typically less than 0.5 Pa·sec, the resin is introduced to the

evacuated preform via a resin port, or multiple resin ports depending on the size and shape of the part. The resin is forced into the preform using only atmospheric pressure, due to the difference in pressure between the evacuated preform and the resin contained outside of the bag at 1.0 atm (101.5 kPa). Because of the low injection pressure and resulting long fill-times, Seemans invented a means by which the resin could be transferred more quickly into the compacted preform. A distribution media layer, or SCRIMP® cloth for Seemanns Composite Resin Injection Molding Process [14, 15], is placed on the top surface of the fiber preform within the vacuum bag. The SCRIMP® cloth has a high permeability compared to the woven fiber. This allows resin to flow quickly across the surface of the part and then filter down into the dry fabric. This is ideally suited for many composite parts, such as boat hulls or the skins of an aircraft wing, because the thickness dimension is much smaller than the length and width dimensions. This allowed entire boat hulls to be fabricated in one infusion step with resin entering the part from various resin port locatons. The composites are infused without any externally supplied pressure and the part can be cured either at room temperature or in an oven, depending on the resin system. The cost of matched metal tooling is eliminated and, since the entire part is contained within a vacuum bag, there is little exposure to the volatile organics involved in handling of other raw materials, such as prepreg. Proper degassing of the resin system and a leak-free vaccum bag ensures high quality, void-free laminate fabrication. Because VARTM is an infusion process, a high level of part integration can be achieved without the tremendous tooling costs associated with prepregged and autoclaved composites. This also reduces the number of fasteners that are necessary in assembly of the same aluminum structure. These advantages found in the SCRIMP® process make it attractive for the fabrication of large composite airframe structure.

Since the concept of the VARTM, or SCRIMP®, process was first patented in 1990, the aerospace industry has expressed interest in its use for the fabrication of aerospace components. One of the most significant disadvantages is the achievable level of fiber volume fraction typical of most parts fabricated by VARTM. In the marine composites industry, the level of fiber volume is not as stringent as that required for aircraft structure.

Fiber volumes in the range of 45% to 50% satisfy the strength and weight requirements for marine composites, whereas safe and cost effective replacement of metals in aircraft structure requires fiber volumes at or near 60%. Because in VARTM all flow and compaction occurs under atmospheric pressure alone, it is difficult to achieve the 60% fiber volume level using this process with conventional woven fabric architectures. As part of the current composites development program, research has been conducted to investigate and develop the VARTM process for manufacture of tailored airframe components. The approach in the process development is threefold. The first goal was to develop and characterize low-viscosity epoxy resin systems that met the toughness requirements for airframe structure. The next goal was to investigate and develop carbon fiber preform architectures that could be used in the VARTM process to achieve higher fiber volumes in the final composite part. The third goal was to fully characterize the VARTM process and determine which, if any, parameters could be modified to achieve higher fiber volumes.

From the beginning, a scienced-based approach was taken using finite element process models as tools to aid in characterization of the VARTM process and its constituent materials. Work was ongoing at the time to modify existing RTM process models, such as the 3DINFIL© model developed at Virginia Tech, to acurately predict the VARTM infiltration [16, 17]. One of the key differences between the two processes is due to the flexible bag which replaces the rigid tooling used in RTM. Because the infiltration occurs under flexible tooling in VARTM, the thickness of the preform changes dynamically during infusion. Because the porosity and permeability of the preform are related to the thickness, it becomes very difficult to accurately model the flow of resin using the conventional finite element, control-volume technique. This effect is discussed in more detail in later chapters. In addition, the process model can only work as well as the empirical data that is used in the computations. This requires accurate characterization of both the resin and fiber preforms to be used in the VARTM fabrication of aerospace components.

An important initial discovery was made by researchers at a leading aerospace manufacturing company which led to improved fiber volume of composites fabricated by VARTM. The modifcation to the process involves small variations in the processing

parameters, however; the process itself is inherently the same. A flexible bag is still used and the part is compacted and infused under atmospheric pressure alone. Part of the research at NASA focused on further developing this variation of the VARTM process. Parts were fabricated using this modified VARTM process with newly developed epoxy resins and novel fiber preforms. The resulting laminates have fiber volumes at or above 60%, void content below 0.5% and excellent mechanical properties [18]. While the specific details of the modified VARTM process will not be discussed in proceeding chapters due to the proprietary nature of the development, it is important to realize that high-fiber volume, aerospace quality laminates are now achievable using this process.

The work that is presented in the following chapters is a culmination of a cooperative research effort performed during the past four years in an effort to develop and understand the VARTM process under the NASA TCAT program. It includes the results of experiments to characterize the constituent materials that may be used to fabricate aerospace structure, including recently developed epoxy resins and fiber preforms. In addition, experiments were performed to characterize both flow and compaction during conventional VARTM, or SCRIMP®, infiltration of fibrous preforms. The results of both the material and VARTM process characterizations are applicable to the modified VARTM process discussed above. The following chapters offer insight into the potential of VARTM in aerospace composites as well as data for future validation of process models.

Chapter 2

Preform Characterization: Compaction

In order to fully understand the flow mechanisms found in the VARTM process, finite element analysis can be used to simulate infiltration under various conditions. A modified 3DINFIL© process model has been applied to the VARTM process by coupling the existing flow sub-model to a new compaction sub-model [17,19]. This is critical to accurately predicting the particular resin flow behavior caused by the presence of a flexible bag and low compaction pressures found in VARTM. One key material input property required by VARTM flow simulation models is the preform compaction behavior. The compaction response and the preform permeability are coupled by the state of the preform, such as the fiber volume fraction and the saturation. In this work, the compaction of preform specimens containing one, two, four, eight and sixteen stacks of the SAERTEX® multi-axial, warp-knit (MAWK) carbon fabric preforms and specimens containing ten and twenty layers of 5-harness satin, biaxial woven carbon fabric were characterized. The experiments were conducted over the range of compaction pressures found in typical VARTM conditions. The resulting experimental data was fit to empirical equations which can be used as material input parameters in process model simulations.

2.1 Background

Previous work [20-24] has led to a better understanding of the unique compaction phenomena associated with the VARTM process. In VARTM, the following equation accounts for the transverse equilibrium inside the mold cavity during impregnation:

$$P_{ATM} = P_R + P_F \tag{2.1}$$

where P_{ATM} is the applied atmospheric pressure, P_R is the resin pressure and P_F is the fiber pressure (pressure supported by the preform). Figure 2.1, a), shows that in the dry condition the preform essentially supports the external pressure, $P_F = P_{ATM}$, and a dry maximum debulking deformation of the preform is reached.

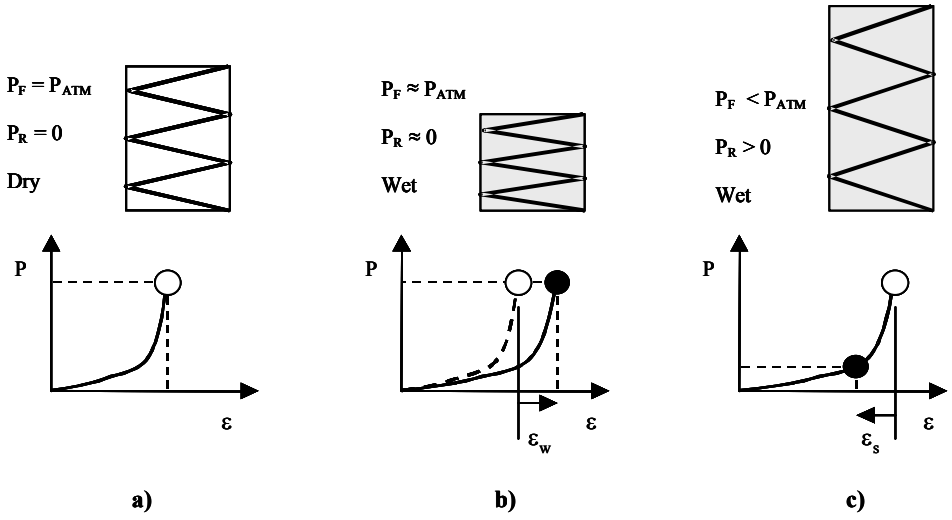

Figure 2.1: VARTM compaction mechanisms, a) dry compaction, b) wetting compaction and c) spring-back.

During infiltration, two deformation mechanisms are present in the wet area of the preform: the wetting compaction and the spring-back. The wetting compaction is caused by a change of the arrangement or state of the fiber network, which is created by the lubrication of the wetting fluid. Under a given external pressure, the lubrication of the dry preform causes an increase in the preform compaction by an additional amount of wetting deformation, Figure

2.1, part b. In VARTM, this mechanism is observed at high fiber pressure ($P_F \approx P_{ATM}$) and low resin pressure ($P_R \approx 0$). The preform spring-back mechanism occurs when the local resin pressure increases. According to Equation 2.1, the total pressure is fixed, therefore; the fiber pressure must decrease when the resin pressure increases. Consequently, the preform compaction decreases by an amount of spring-back deformation due to the reduced pressure carried by the preform. The deformation experienced during spring-back includes both elastic and time-dependent, viscoelastic recovery [25, 26]. In Figure 2.2 a typical compaction test data set are shown including dry compaction, dry unloading and wet unloading modes. The independent variable "Pressure" is plotted on the ordinate to provide ease of view. The fiber lubrication is noted by the increase in fiber volume fraction, V_f, at 101 kPa after the fabric specimen is wetted. The wet unloading portion of the curve is a quasi-static representation of the infusion of the fabric during a VARTM infiltration. The hysteresis phenomenon is evidenced by the difference in the starting point of the dry loading, or compaction, curve at $V_f = 47\%$ and the ending point of the dry unloading curve at $V_f = 52\%$. This difference of 5% represents the permanent or inelastic deformation of the fabric. The region of the dry unloading curves from $V_f = 55\%$ to 52% represents the elastic response of the fabric. The curves exhibit a permanent deformation due to nesting of the fabric.

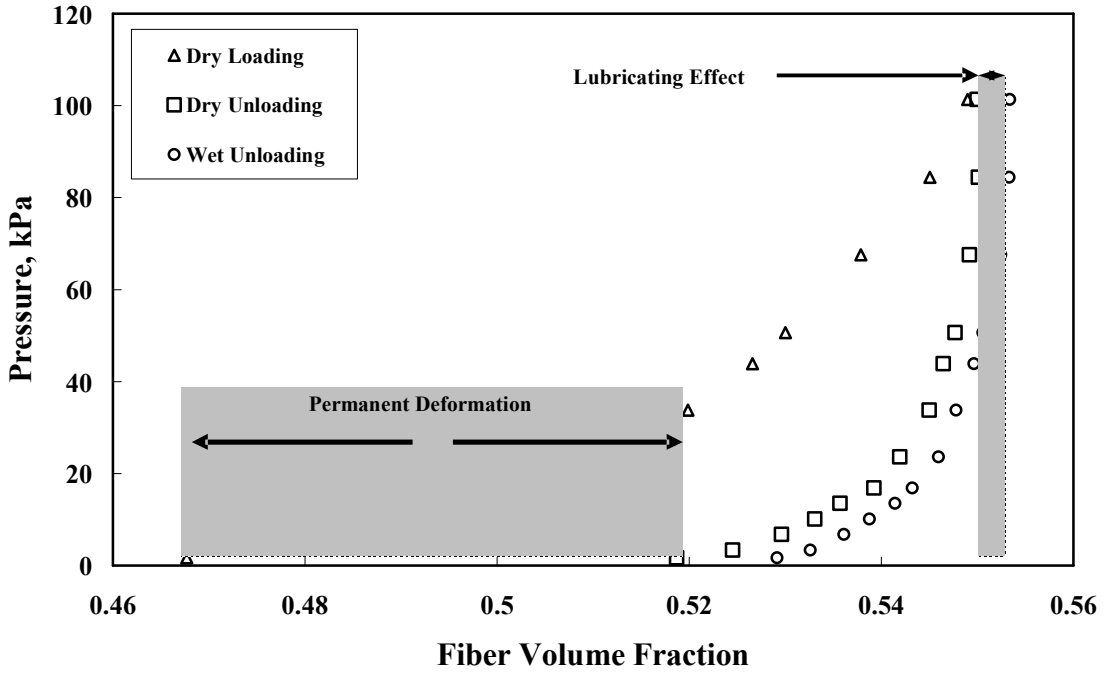

Figure 2.2: Typical compaction behavior of a fibrous preform.

At any time during the infiltration process, the net compaction of the preform depends on the relative magnitude of the wetting and the spring-back deformation mechanisms. Other work [27] to characterize the compaction of non-crimp, knitted carbon fabrics has shown that the fiber volume of the specimens at pressures ranging from 50 kPa to 700 kPa was influenced by the number of layers or "stacks" of the knitted performs in the specimen. It was found that the amount of nesting increases with the amount of stacks in a specimen. The evidence of this inter-stack influence on fiber volume would require compaction characterization specific to the stacking sequence and thickness of the preform to be infused.

2.2 Materials

The carbon fabrics studied in this work are multi-axial warp-knit (MAWK) fabric supplied by SAERTEX® and a 5-harness satin biaxial woven fabric composed of Hexcel 6k IM-7

fiber tows supplied by Textile Products, Inc. The balanced fabric depicted in Figure 2.3 had a tow count of 16 tows in the warp and fill directions and a fiber areal weight of 280 g/m^2.

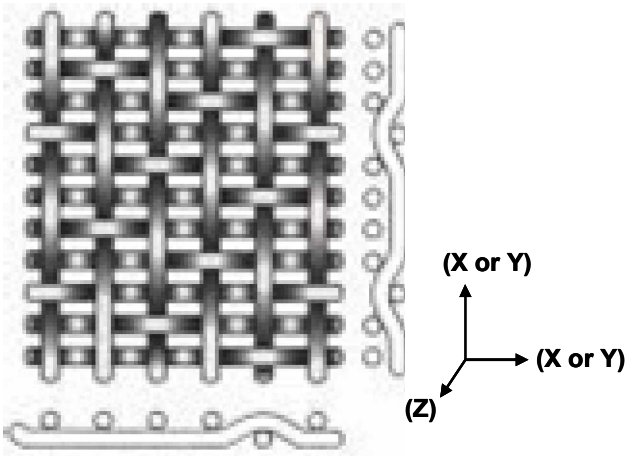

Figure 2.3: Graphical depiction of a 5-harness satin biaxial woven fabric.

The MAWK material is depicted in Figure 2.4. It is composed of seven plies of both AS-4 and IM-7 carbon fibers with a single-stack, total areal weight of of 1423 g/m^2. The plies are stacked, not woven, and then knitted with an alternating polyester tricot/chain knit thread in

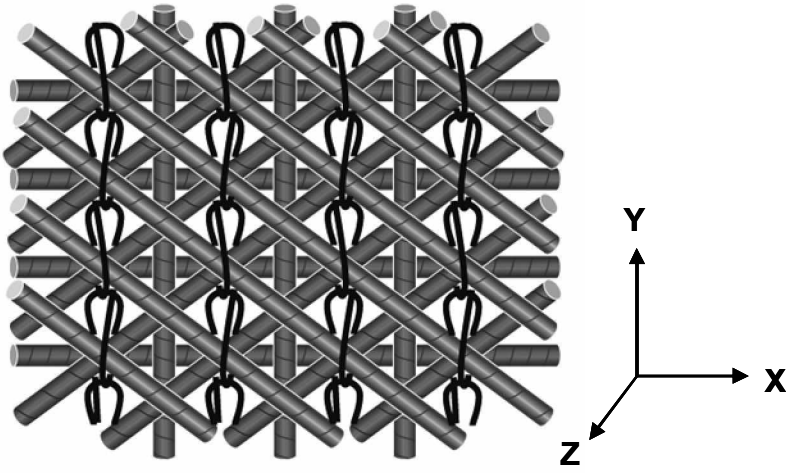

Figure 2.4: Graphical depiction of a multi-axial warp knit (MAWK) fabric.

the stacking sequence described in Table 2.1. In this work, the 0° fiber tows are designated as the fabric x-direction. A fiber density of 1.78 g/cc was used for both the biaxial and

MAWK fabrics. In addition to the carbon fabrics studied, the compaction behavior of the VARTM constitutive processing materials were determined, including the distribution media, or scrimp cloth, as well as the release layer and bagging film. The distribution media was composed of three layers of nylon mesh called Plastinet (Applied Extrusion Technology, Inc). The release layer was a 38 μm thick woven glass mat coated with Teflon and called Release Ease®#234. The vacuum bagging film is composed of 76 μm thick nylon and desiganted Ipplon DP1000. Both of these materials were supplied by Airtech Advanced Materials Group.

The wetting fluid used in the experiments was an SAE 40 motor oil. The fluid was chosen for its relative ease of use, safe handling and low cost. Prior to each test, the viscosity was measured using a Brookfield viscometer. For oil temperatures ranging from 21.4°C to 25.4°C, the Brookfield viscosity varied from 0.34 Pa•sec to 0.24 Pa•sec, respectively.

Table 2.2: Ply Stacking Sequence in SAERTEX MAWK Fabric.

Ply Number	**Yarn Material**	**Yarn Orientation**	**Areal Weight g/m^2**
1	3K-AS4	+45°	156
2	3K-AS4	-45°	156
3	12K-IM7	0°	314
4	6K-AS4	90°	171
5	12K-IM7	0°	314
6	3K-AS4	-45°	156
7	3K-AS4	+45°	156

2.3 Experimental

The vacuum bag compaction experiments were conducted in both dry and wet conditions to gauge the compaction response of the carbon fabrics at the low pressures experienced during VARTM processing. A schematic diagram of the vacuum bag test bed is shown in Figure 2.5. An instrumented aluminum tool was used to measure pressure and displacement of the preform. Pressure sensors (Omega Engineering, Inc., Series PX102) were mounted at the tool surface beneath the fiber preform. A linear variable displacement transducer (LVDT), Omega Engineering, Inc., Series 400, as well as a laser gauging sensor (L-Gage® Banner Technologies) were suspended above the vacuum-bagged preform by a rigid beam. Sensor outputs were recorded by a PC-based data acquisition system using LabVIEW® software.

Preform specimens were carefully cut into 15 cm x 27 cm rectangles, weighed and placed on the tool. For the sake of continuity, the compaction specimens were laid-up on the tool and bagged similar to a conventional VARTM infiltration. The distribution medium, containing three layers of nylon mesh screen, was placed beneath the resin inlet distribution tubing and atop the preform to a point within 2.54 cm of the LVDT and pressure sensor.

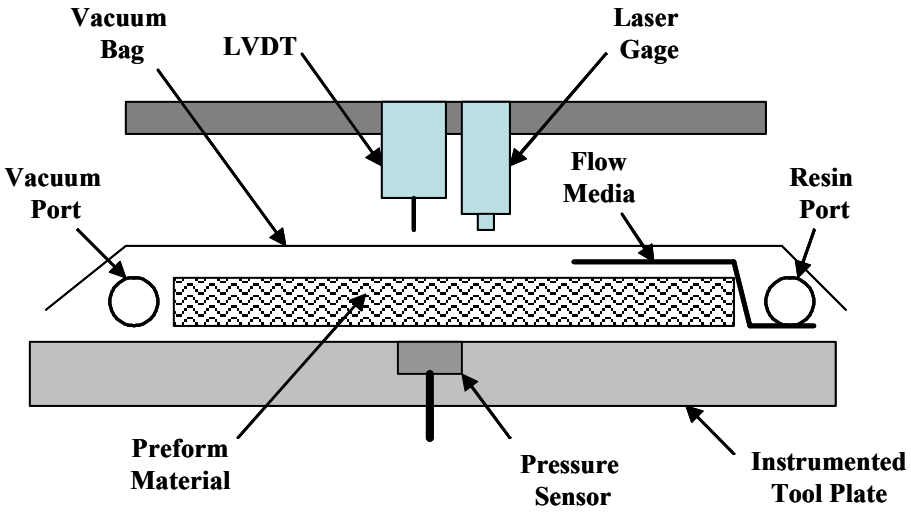

Figure 2.5: Schematic of vacuum-bag compaction test bed.

Therfore, the thickness of the media was not included in calculation of the resulting curves. The specimens were placed on the tool surface so that the advancing flow front would contact the pressure sensor at the same time that the preform under the LVDT was wetted.

For the dry preform tests, the bagged preform was evacuated via one port located approximately 12 cm from the preform. The displacement was recorded at preset pressure levels from 1.70 kPa to 101.5 kPa after allowing the displacement to reach steady state at each of these compaction levels (approximately 200 seconds). In the wet compaction test, the resin and vacuum lines were placed following the procedure for a typical VARTM infiltration. The vacuum bag was initially evacuated to 12.7 mm Hg (1.7 kPa compaction pressure) to zero the LVDT. For the dry preform test, the vacuum bag was then steadily evacuated to full vacuum, 760 mm Hg (101.5 kPa compaction pressure). Once the preform displacement stabilized, the bag was steadily vented back to 12.7 mm Hg.

In the wet preform compaction test, the bagged preform was initially impregnated with wetting fluid by applying a small pressure gradient to the preform. Once the preform was fully impregnated, full vacuum was applied to the bag until a steady state compaction deformation was measured. Then, the bag was slowly vented by opening the inlet and allowing resin to flow back into the preform. The results are displayed in the next section.

For the sake of comparison, a separate approach was taken to determine the dry compaction behavior of several of the preform specimens as well as a starting thickness at some predetermined pressure. To accomplish this, a SATEC® T1000 test frame with a Transducer Techniques® 2.2×10^{-2} kN load cell was utilized. The fixture consisted of two circular parallel plates with a diameter of 1.60 cm and 10.1 cm for the top and bottom plate respectively. After zeroing the fixture, a 2.54 cm x 2.54 cm specimen was placed between the two plates. The fixture was closed until the slightest load was registered, i.e., less than 2.2×10^{-3} N. The test was then started when the specimen was loaded at a strain rate of 1.3×10^{-3} mm/s until the load reached the predetermined loading point, in this case 0.334 N which corresponds to 1.70 kPa (0.5 in Hg). At this point the strain rate was decreased to 1.3×10^{-4} mm/s to allow for the viscoelastic response in the fabric. The strain rate was cycled at these rates between

0.311 N and 0.334 N until the load overcame the relaxation and continued to increase above the 0.334 N limit. Cycling the strain rate between the upper and lower bounds of load simulated a pressure hold at 1.70 kPa inside the vacuum bag. The loading continued at 3.11 N (5.0 kPa) intervals until the final loading was reached at 62.8 N (101.5 kPa).

2.4 Results

Figure 2.6 shows the typical raw data taken using the L-Gage and pressure sensor. The fiber volume fraction, V_f, is calculated by the following equation:

$$V_f = \frac{FAW}{t * \rho_F} \tag{3.2}$$

where, FAW is the fiber areal weight of each specimen, t is the measured thickness, and ρ_f is the desity of the carbon fiber. The FAW is found by weighing a preform specimen of known area and dividing the area by the weight. The FAW would therefore increase in value for each specimen as stacks or layers were increased. The resulting dry compaction and wet unloading plots of V_f vs. pressure for one, two, four, eight and sixteen stacks of MAWK as well as the results for 10- and 20-layer specimens of the biaxial fabric are included in the Appendix as Figures A1-A14. Included in these plots are the curves resulting from the test frame experiment for one, two and four stacks MAWK and 10 layers of biaxial fabric.

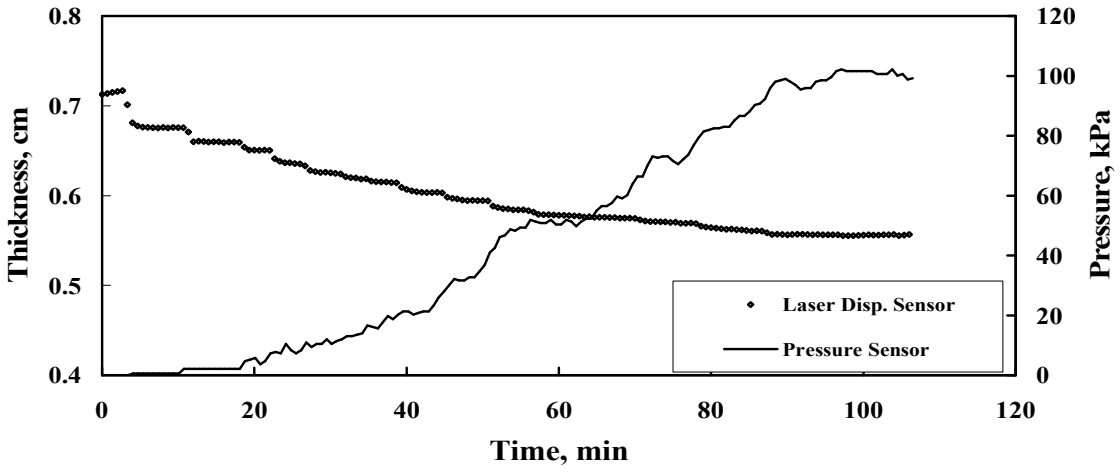

Figure 2.6: Typical raw data of a vacuum bag compaction test.

Both the shape of the curves and the maximum V_f found using the test frame procedure were found to differ from the experiments conducted under a vacuum bag. This is likely due to the time difference in the test. In the vacuum bag compaction test, the pressure was held at each increment for approximately 200 seconds. Presumably, this allowed the fabric to fully nest at the given level of compaction. As described in Section 2.3, the frame test was conducted so that the machine itself would continue to the next load increment after it sensed that the cyclic load had overcome the relaxation of the fabric. This resulted in less than 200 second holds at each increment during the frame tests. At the end of each of the frame tests it was observed that when the specimen reached the maximum load and the test was finished by holding the platens at the final displacement level. The load sensed by the transducer immediately began to decrease. This indicates further relaxation and therefore that the specimen, given time at the final load level, would continue to decrease in thickness.

Since no general constitutive model is available to describe the compaction behavior of these types of preform materials, the relationship between the compressive strain in the preform and the applied pressure is obtained by fitting the compaction curve data shown in Figures A2.1-A2.13 to an empirical model. Equation 2.3 shows the relationship between the fiber volume fraction, V_f and the strain, ε, where ϕ is the initial preform porosity.

$$V_f = \frac{1-\phi}{1-\varepsilon} \tag{2.3}$$

Prior to a VARTM infusion the fiber preform is compacted beneath the vacuum bag. Thus, the compressive strain of the preform can be calculated by curve fitting to the dry compaction results. As the flow front moves through the preform, thus wetting the fabric, the local net pressure applied to the preform decreases according to Equation 2.1. Therefore the strain in the wet preform is determined by fitting an empirical model to the wet unloading test results. The resulting equations (2.4) and (2.5) were fit to the data from the vacuum-bag, dry-compaction and wet-unloading tests:

$$\varepsilon_{dry} = a_{dry}(1 - e^{(b_{dry} * P_f)}) \tag{2.4}$$

$$\varepsilon_{wet} = a_{wet} + b_{wet}\left(\frac{P_f}{c_{wet} + P_f}\right) \quad (2.5)$$

where P_f is the net compaction pressure applied to the preform. The results of curve fitting both the dry and wet compaction model equations as well as the statistical deviation based on the multiple LVDT and L-Gage tests performed for each stacking scheme are plotted in Figure 2.7 through 2.13. The averaged constants of these empirical equations are tabulated for all the specimens characterized in Table 2.2 below.

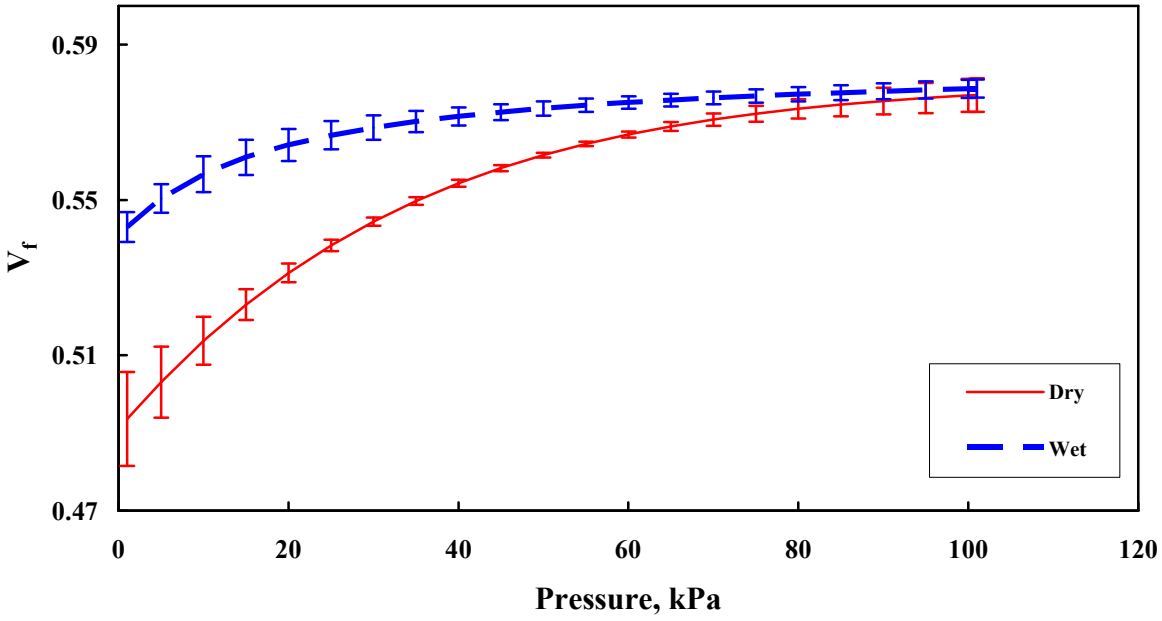

Figure 2.7: Resulting relations and error bars from dry and wet compaction model equations for MAWK one stack.

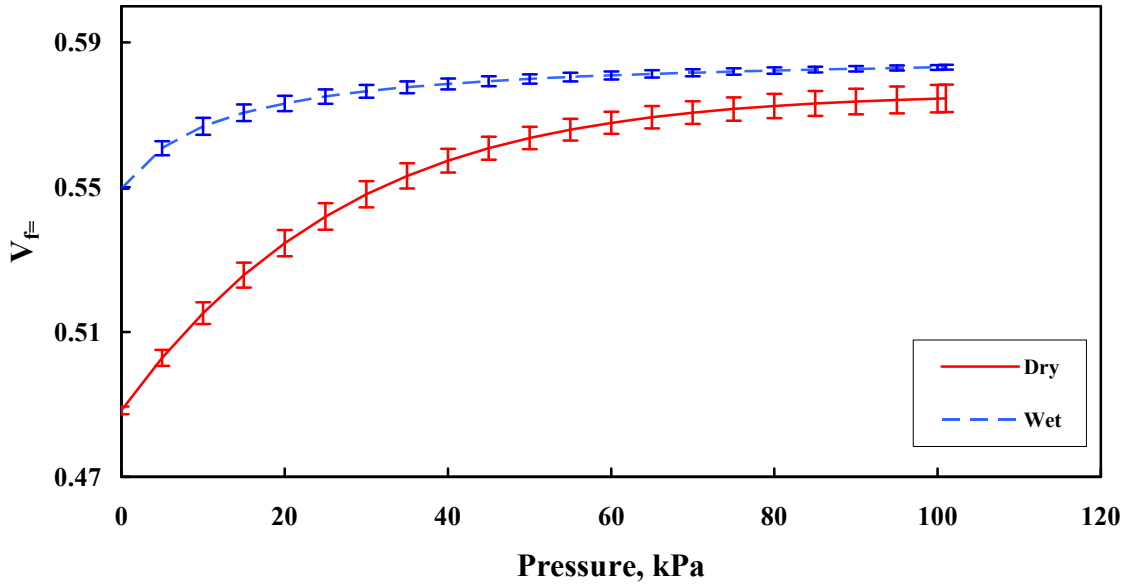

Figure 2.8: Resulting relations and error bars from dry and wet compaction model equations for MAWK two stacks.

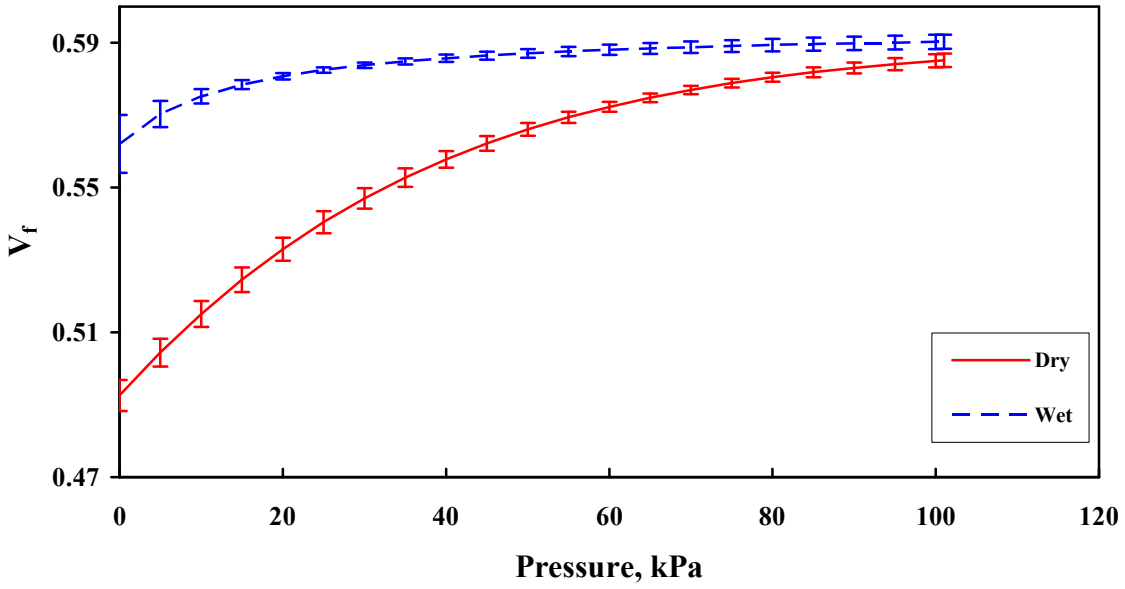

Figure 2.9: Resulting relations and error bars from dry and wet compaction model equations for MAWK four stacks.

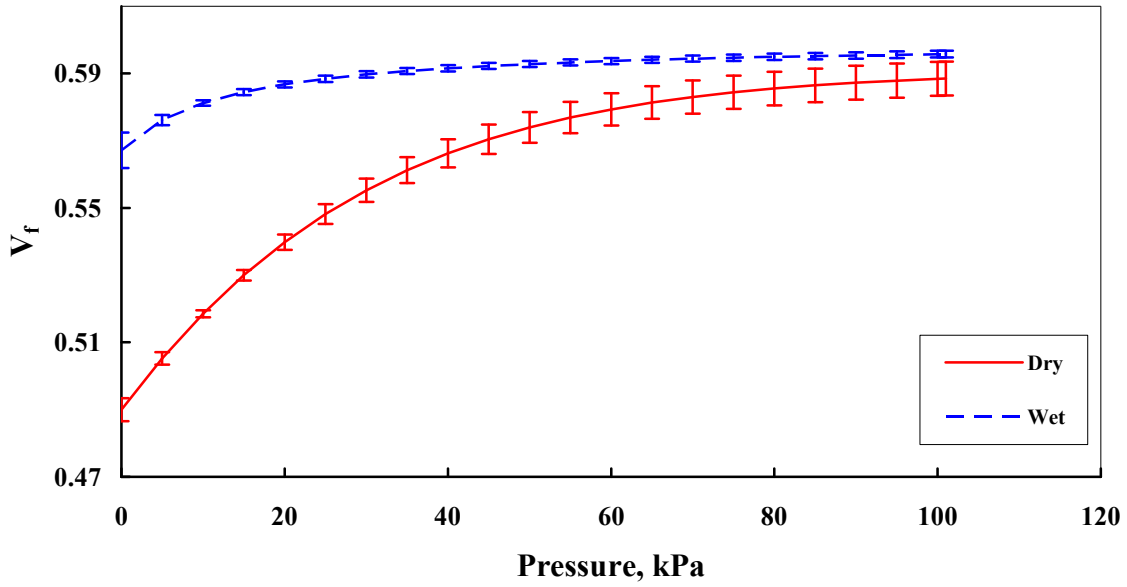

Figure 2.10: Resulting relations and error bars from dry and wet compaction model equations for MAWK eight stacks.

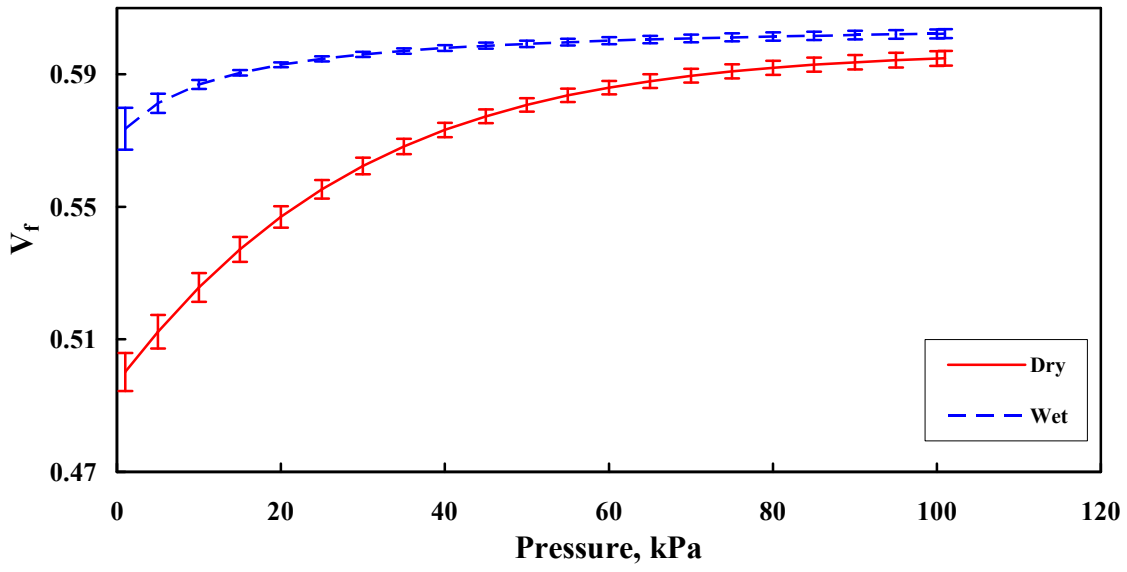

Figure 2.11: Resulting relations and error bars from dry and wet compaction model equations for MAWK sixteen stacks.

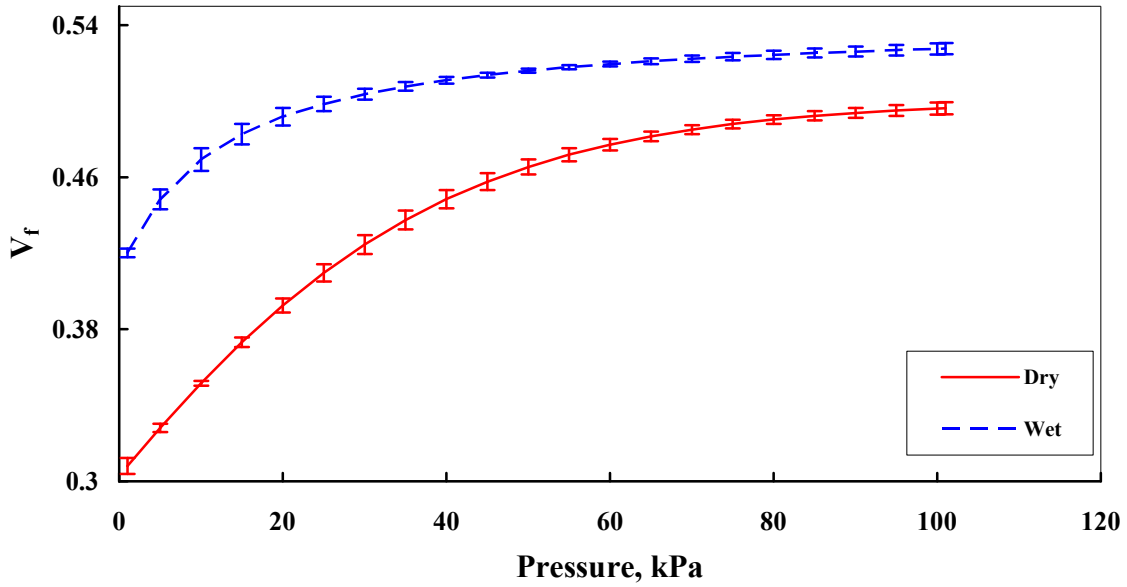

Figure 2.12: Resulting relations and error bars from dry and wet compaction model equations for biaxial 10 layers.

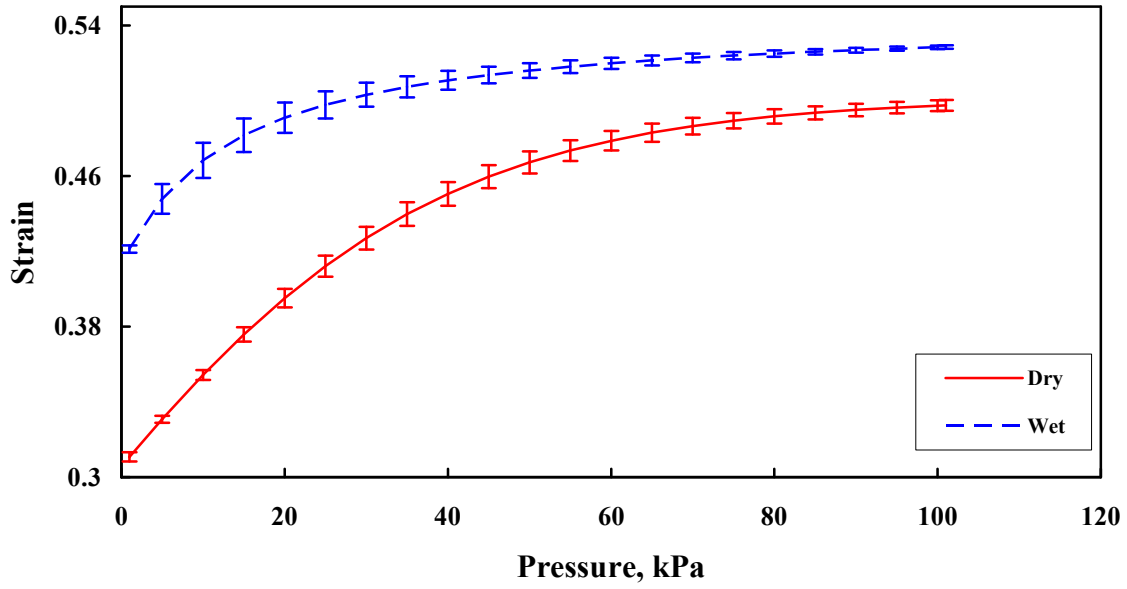

Figure 2.13: Resulting relations and error bars from dry and wet compaction model equations for biaxial 20 layers.

In each of the compaction relations represented in Figures 2.7-2.13, the fiber lubrication is noted by the increase in fiber volume fraction at 101 kPa after the fabric specimen is wetted. This lubrication phenomenon is more prevelant in the biaxial fabrics noted by the larger shift in V_f at 101.5 kPa in Figures 2.12 and 2.13. In addition, the hystereris effect noted previously is evident in all the figures by the difference in V_f at the 1 kPa portion of the curves.

Figures 2.14 and 2.15 display the combined curve-fit plots for the MAWK fabric in dry and wet conditions, respectively. It is evident from these curves that as the number of stacks are increased, a shift in the curve results and the final, or maximum, fiber volume fraction attainable is increased. This increase may be due to the influence of the interstack region where the surface of one stack rests against a subsequent stack. In this region the fibers may be able to nest more easily than within the stack itself. The knitting used to hold the plys together in each stack may act to restrict displacement of the fibers within the stack. Between the stacks, however, the knitting appears to provide a surface that is more conducive to nesting. The increase in fiber volume due to an increase in the number of MAWK stacks is also evident in the specimens compacted using the test frame procedure as shown in Figure 2.16.

Table 2.2: Compaction Model Parameters.

		Curve-Fit Constants				
		Dry Compressive Strain, ε_{dry}		Wet Compressive Strain, ε_{wet}		
Preform Material	**Average FAW, g/cm^2**	**a_{dry}**	**b_{dry}**	**a_{wet}**	**b_{wet}**	**c_{wet}**
MAWK, one stack	**0.145**	**0.154**	**0.034**	**0.092**	**0.070**	**16.78**
MAWK, two stack	**0.289**	**0.152**	**0.042**	**0.113**	**0.056**	**11.06**
MAWK, four stack	**0.581**	**0.166**	**0.031**	**0.127**	**0.047**	**13.74**
MAWK, eight stack	**1.157**	**0.171**	**0.039**	**0.136**	**0.047**	**12.26**
MAWK, sixteen stack	**2.318**	**0.168**	**0.039**	**0.129**	**0.050**	**11.12**
Biaxial, ten layers	**0.285**	**0.395**	**0.043**	**0.262**	**0.179**	**9.31**
Biaxial, twenty layers	**0.569**	**0.391**	**0.043**	**0.258**	**0.179**	**10.19**

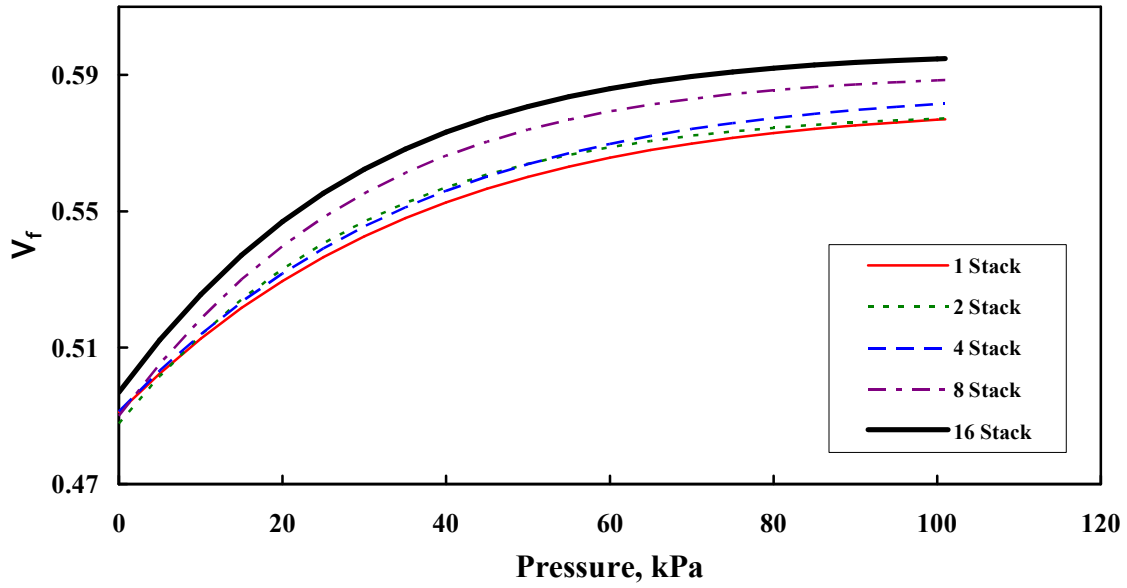

Figure 2.14: Combined model relations for MAWK in dry compaction conditions.

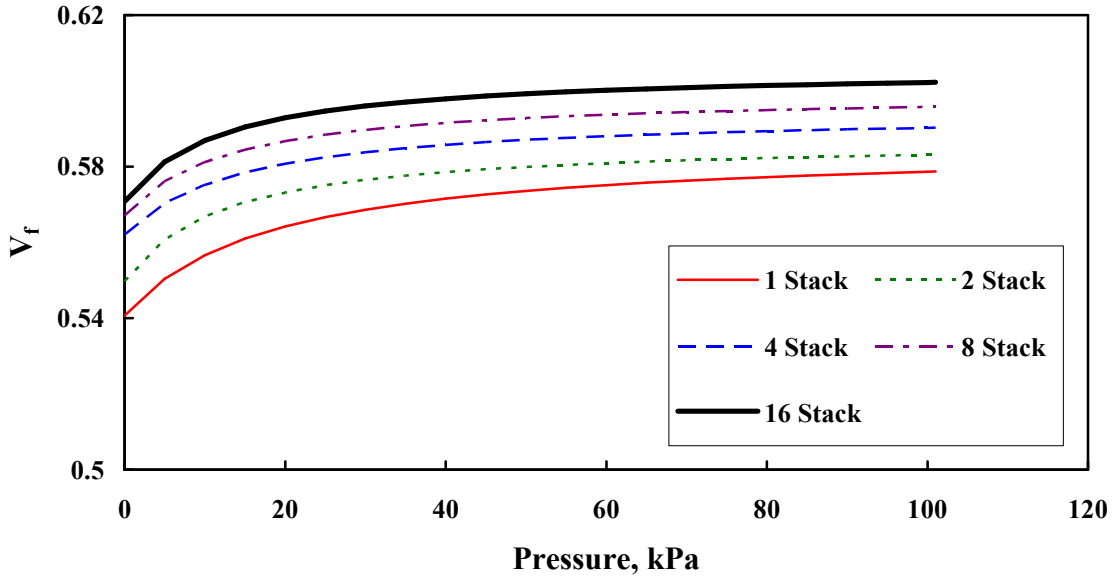

Figure 2.15: Combined model relations for MAWK in wet unloading conditions.

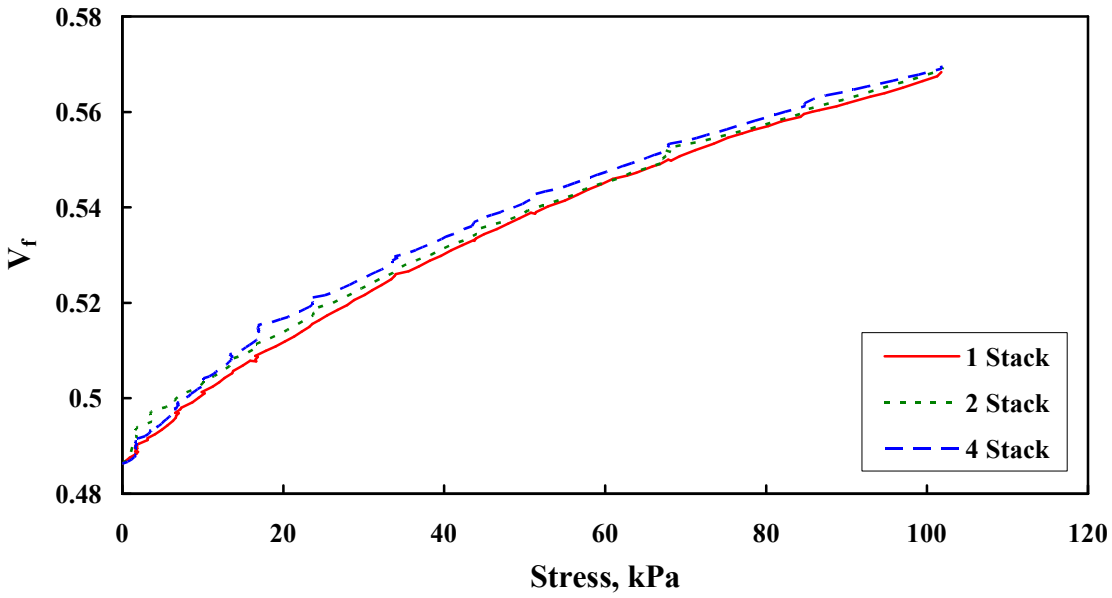

Figure 2.16: Combined test frame results for MAWK in dry compacting conditions.

The interstack phenomenon was not evident in comparing the relations generated from the biaxial fabric charaterization, as shown in Figures 2.17 and 2.18. With this type of material the addition of layers of fabric does not appear to influence the maximum attainable V_f. This material does not contain any knitting because the fiber bundles are woven together. Hence, the presence of knitting in the MAWK fabric is likely the reason for the increase in V_f with the addition of stacks.

In addition to the influence of the interstack region on the fiber volume fraction of the MAWK fabric, it is also important to note how the fabrics, both MAWK and biaxial, react to the release of the pressure in the wet unloading characterization tests. It is evident in all of the wet unloading curves shown for both the MAWK and biaxial materials in Figures 2.15 and 2.18 that the majority of the decrease in fiber volume, or increase in thickness, occurs after the fabric has reached the 55 kPa unloading point. In fact, an average of 90% of the displacement occurs after the material has reached this point. In other words, half of the compacting pressure is removed prior to the material having any appreciable loss in fiber

volume fraction. Likewise in the dry compaction test results in Figures 2.14 and 2.17 the majority of the displacement occurs prior to the 65 kPa loading point. Very little compaction of the fabrics occur between 70 and 101 kPa.

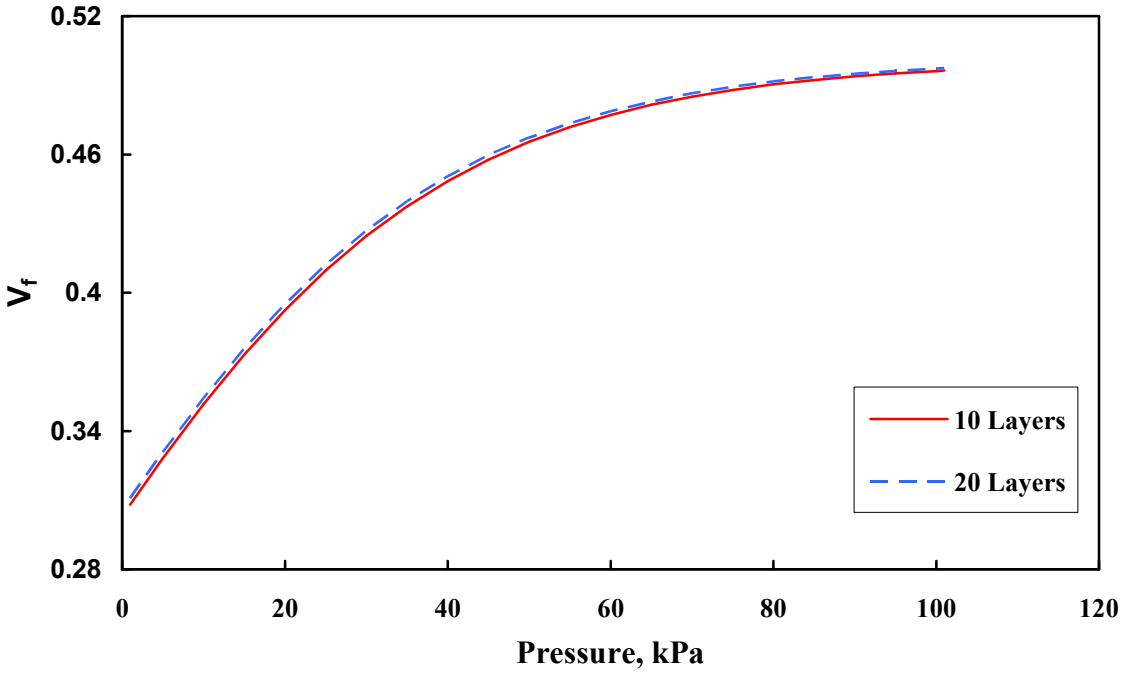

Figure 2.17: Combined model relations for biaxial in dry compaction conditions.

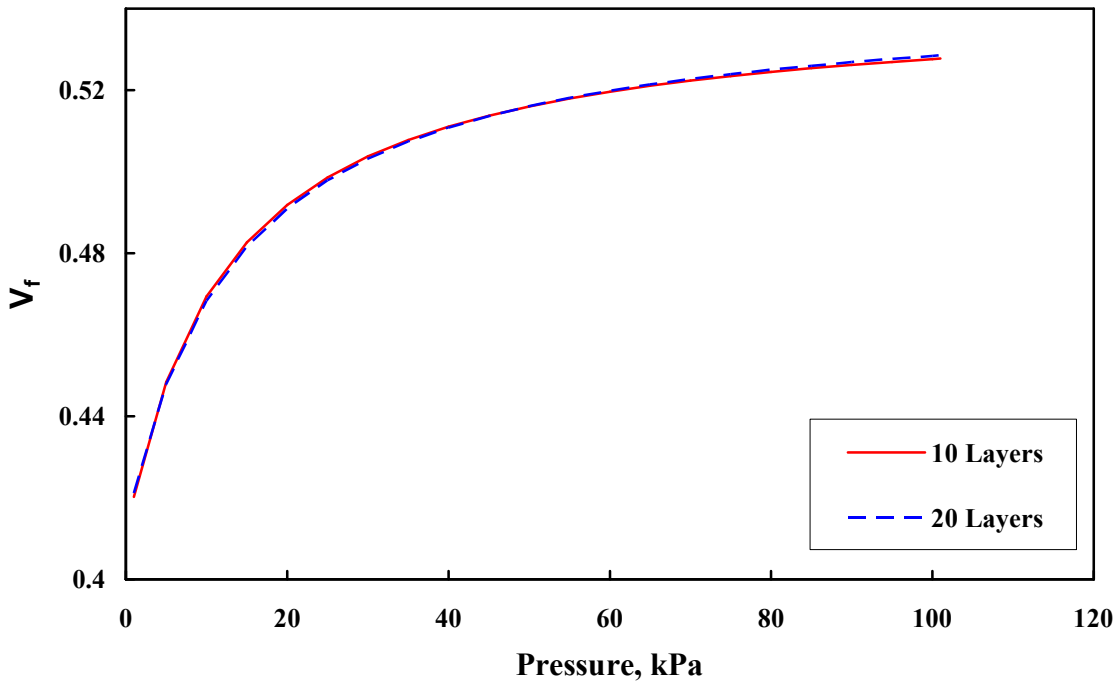

Figure 2.18: Combined model relations for biaxial in wet unloading conditions.

In addition to determining the compaction response of the carbon fiber preform materials, the response of the bagging materials was also determined. These materials include the bagging film, three layers of distribution medium, and the one layer of release (peel) cloth, as described in Section 2.2. In this experiment the media and release cloth were placed inside the vacuum bag. The bag was fully evacuated to 760 mm Hg, resulting in a compaction pressure of 101.5 kPa, and held for approximately 500 seconds. The results in Figure 2.19 show that after the material is debulked at the maximum compaction value, there is no evident further decrease in thickness. The material is stiff enough to resist any further relaxation at these pressures. The resulting thickness value from this test was used as a standard for subtracting the bagging material thickness from the data obtained in the infiltration experiments presented in Chapter 5.

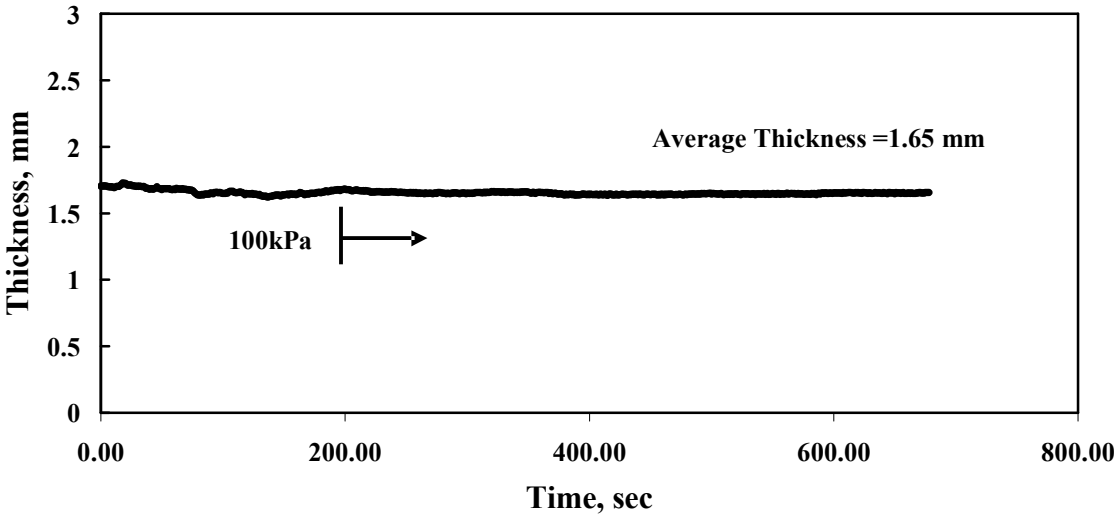

Figure 2.19: Dry compaction results for bagging materials, including one layer of nylon bagging film, three layers of Plastinet® distribution media, and one layer of Release Ease®.

Chapter 3

Preform Characterization: Permeability

Adaptation of an infusion process like VARTM to manufacture of aerospace structure requires accurate prediction of large-scale part fill times. Accurate flow simulations require detailed knowledge of the impregnation behavior of the fiber preform materials. In addition to the compaction behavior, the other critical material input property required for accurate flow prediction is the preform permeability. Permeability is a measure of the preform material's resistance to flow and relates the velocity of the infiltrating fluid to the pressure gradient within the preform. To determine the effects of preform thickness and the inter-stack influence on the permeability of the MAWK material, tests were perfomed to measure the permeabilities of specimens containing one, two, four, eight and sixteen stacks of the SAERTEX® multi-axial, warp-knit (MAWK) carbon fabric. The in-plane and transverse permeabilities of specimens containing ten and twenty layers of 5-harness satin, biaxial woven carbon fabric were also characterized. The experiments were conducted over the range of compaction levels found in typical VARTM conditions. The results of the experiments were fit to empirical equations and can be used as material input parameters in the flow simulation finite element process models.

3.1 Background

Flow of resin through fibrous media is commonly modeled using Darcy's law [28-30]. Permeability is defined as the resistance to flow through porous media and is often related to the porosity using an empirical model. The three-dimensional form of Darcy's Law for an anisotropic material is written in Cartesian coordinates as:

$$\begin{bmatrix} \bar{q}_x \\ \bar{q}_y \\ \bar{q}_z \end{bmatrix} = \frac{1}{\eta} \begin{bmatrix} S_{xx} & S_{xy} & S_{xz} \\ S_{xy} & S_{yy} & S_{yz} \\ S_{xz} & S_{yz} & S_{zz} \end{bmatrix} \begin{bmatrix} \partial P / \partial x \\ \partial P / \partial y \\ \partial P / \partial z \end{bmatrix} \tag{3.1}$$

where S_{ijk} are the components of the permeability tensor, $q_{bar,ijk}$ are the components of the superficial velocity vector, η is the viscosity of the fluid and P is the pressure. For preform architectures that are orthotropic, the components S_{xy}, S_{xz} and S_{yz} are zero and Equation 3.1 simplifies to:

$$\begin{aligned} \bar{q}_x &= \frac{1}{\eta} S_{xx} \frac{\partial P}{\partial x} \\ \bar{q}_y &= \frac{1}{\eta} S_{yy} \frac{\partial P}{\partial y} \\ \bar{q}_z &= \frac{1}{\eta} S_{zz} \frac{\partial P}{\partial z} \end{aligned} \tag{3.2}$$

In this work, the *x-direction* runs parallel to the advancing flow front in a VARTM panel infiltration. The *y-direction* is 90° and in-plane to x. The *z-direction* is the transverse, or through-thickness, flow direction.

Several models have been developed in the past to estimate the permeability of fiber preforms. The Kozeny-Carmen capillary model was developed and sucessfully predicted permeability in granular beds consisting of ellipsoids [31]. However, this method is deficient in prediction of permeability for non-isotropic flow in continuous fiber preforms. Gebart, among others [32, 33], developed models to approach this problem based on a geometry of

ordered arrays of cylinders. These models were found to more accurately predict the axial and transverse permeabilities of fibrous preforms. Gokce and Advani further developed these models to include the influence of intra-tow flow on preform permeability determination [34]. The technique takes a micromechanical approach incorporating the Method of Cells in which a unit cell, the preform, contains sub-cells with the characteristics of one tow, or bundle, of fibers. These chararcteristics include the geometry of the fiber tow, the necessary porosity, or air gaps, surrounding the tow and the pressure distribution along the tows. This requires that the properties of the fiber tow be determined experimentally. The sub-cells are organized in the unit cell according to the particular fabric geometry and the unit cells are then structured according to the desired composite part geometry. Use of this method in conjuction with Darcy's law and the continuity equation allows for a more general approach to the prediction of the permeability tensor of a variety of fiber architectures in a variety of final part geometries.

While predictive models for the determination of preform permeability are both cost effective and extremely important to develop a physical understanding of flow through porous materials, experimental methods are still more commonly used. Experimental techniques for measuring the permeabilities of fiberous materials, especially for RTM applications, is well developed in the literature [35-37 and 16]. Trevino, et al. [35] measured the in-plane and transverse (through-thickness) permeabilities by placing the fiber mats into rigid steel molds. Fluid was pumped into the closed molds at a constant flow rate and the pressure differential was measured between the fluid entry and exit on either side of the compacted preform. The pressure was recorded after the fabric was fully saturated and the measured fluid pressure had reached steady state conditions. The permeability was then calculated based on Darcy's law and the steady-state pressure difference. The mold was designed with a fixed cavity volume. In order to vary preform porosity, additional layers of fabric were simply added to the mold. The in-plane and transverse permeabilities of both randomly oriented and continuous bi-directional fabrics were characterized as a function of porosity. Trevino determined that for the fabrics studied, the transverse permeability was

always lower than the in-plane values and that part infusion times would be greatly affected by the fiber anisotropy.

Hammami [37] determined that flow in VARTM differs from the traditional RTM process. The flexible vacuum bag and varying pressure inside the mold cavity result in a variation of the preform thickness and, hence, the fiber volume fraction of the preform during infusion. The variation of compaction pressure during infiltration necessitates measurement of the preform permeability at varying fiber volumes. Hammami also stressed the importance of determining the permeability of the distribution media, or "flow enhancement layer."

Work by Sommerscales [39] and others [40] found that because the wetting characteristics, namely surface tension and contact angle, of various permeant fluids differ, their use can influence the measured permeabilities of the preform. Steenkamer, et al. [40], determined the effect on permeability by varying the permeant. The fluids investigated included diluted corn syrup (viscosity, η = 0.19 Pa·sec), SAE 10W-30 motor oil (η = 0.16 Pa·sec), and a vinyl ester resin (η = 0.14 Pa·sec). The corn syrup exhibited the highest contact angle on the woven glass mat at 45^{o}, followed by the resin at 38^{o}. The contact angle of the oil could not be measured because it spread too quickly. The work of spreading was measured for each fluid and reported as syrup = -189.0 μN/cm, oil = 16.0 μN/cm and resin = -74 μN/cm. The negative value of work of spreading means that pressure had to be applied to achieve fiber wetting. The results of permeability characterization with these three materials showed that the fabric tested with the motor oil had the highest in-plane permeability of 1.74x10-9 m^2 followed by the resin at 1.23x10-9 m^2 and the syrup at 0.70 x10-9 m^2. This indicates that the effect is more highly dependent on the surface tension of the permeant rather than the viscosity. The author concluded that the permeability measurements should, ideally, be conducted using the resin that will ultimately be used to infuse the composite part. Luo, et al. [41], and Hammond and Loos [42], found that the effect of different permeants was within the scatter of the measured permeabilities.

In the present investigation the permeabilities of the carbon fabric preforms were measured using an SAE 40 motor oil as the permeant due to its similar viscosity to the epoxy resins

investigated in the work. As stated, the overall purpose of the work is to validate the 3DINFIL model. All validation infiltration experiments described in subsequent chapters, as well as the compaction characterization, were performed using this fluid. It was chosen because it is relatively safe for the user and will not damage the costly equipment used to perform the experiments. Therefore, the permeabilites reported in the following sections may be considered to be "apparent" values relative to the fluid used and treated as such.

3.2 Experimental

Experiments were conducted to measure the in-plane (S_{xx} and S_{yy}) and the transverse (S_{zz}) permeability at fiber volumes ranging from 45% up to 60% for the MAWK fabric specimens and 35% to 55% for the biaxial fabric specimens. The tests were performed at or below the VARTM injection pressure of 101.5 kPa. Schematic diagrams of the in-plane permeability test fixture are shown in Figure 3.1. Both the in-plane and through-thickness fixtures were essentially rigid steel molds instrumented with diaphragm pressure sensors and LVDTs. The fixtures were mounted in a compression test frame. The in-plane fixture was designed to characterize preform specimens 15 cm in length by 15.3 cm in width at thicknesses ranging from 0.0 cm to 2.5 cm.

A 1.2 cm x 15.3 cm strip of steel screen was added to the in-plane fixture after initial tests at the lower fiber volumes showed that the preform specimens tended to slide across the ground surface of the fixture. The screen was placed at both ends of the preform to ensure identical boundary conditions at both the resin filling and exiting sides. The in-plane fixture utilized two LVDTs to ensure uniform thickness across the 15.0 cm length of the specimen. Four pressure sensors were contained in this fixture. The sensor located at the inlet side was utilized in this study for permeability characterization under steady-state conditions. The remaining three pressure sensors can be used for advancing-front characterization.

In testing the MAWK fabric, the specimen was placed so that the 0° rovings (as described in Table 3.1) were length-wise, or parallel to the direction of resin flow for determination of S_{xx}. For S_{yy}, the specimen was placed so that the 0° rovings were perpendicular to the direction of flow. Due to the architecture of the biaxial fabric, the S_{xx} and S_{yy} permeabilities

were assumed to be equal. Therefore, tests were conducted to determine only the S_{xx} and S_{zz} permeability of this fabric.

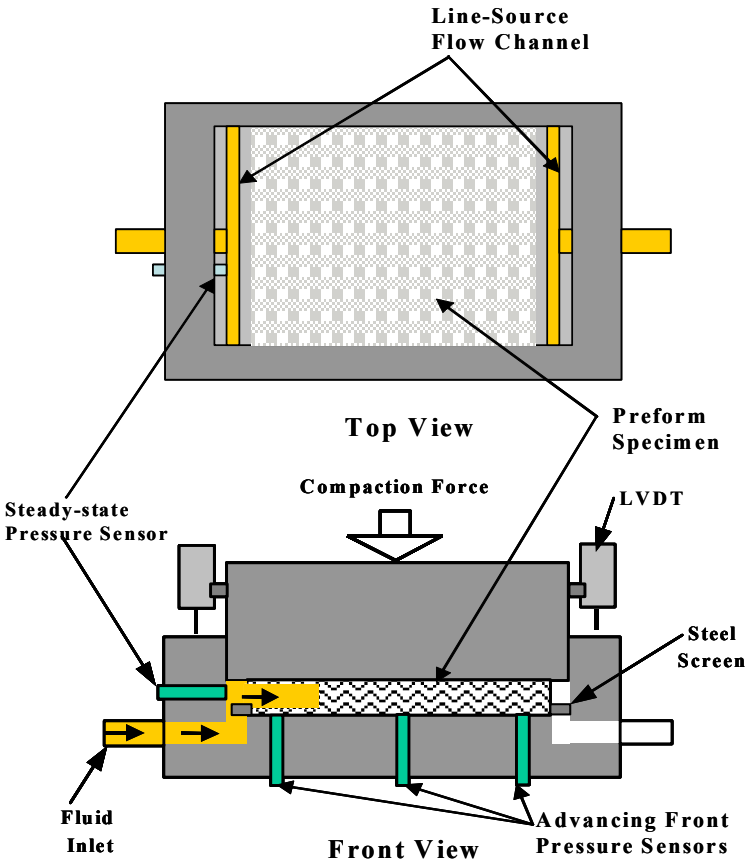

Figure 3.1: In-plane permeability measurement fixture.

The transverse, or through-thickness, S_{zz}, fixture (Figure 3.2) was designed to test fabric specimens 5.08 cm x 5.08 cm up to 3.20 cm thick. The concept is identical to that of the in-plane fixture except that the fluid flowed into and out of the specimen via a rigid distribution plunger and base plates, which rested against the 25.81 cm^2 surface on both sides of the specimen. The plate contained a hole-pattern with 0.50 cm holes drilled every 0.64 cm.

Prior to the permeability tests, the temperature of the SAE 40 oil was recorded and the viscosity was measured using a Brookfield® model DV-III viscometer. The viscometer was calibrated using standards supplied by Brookfield®. The results of the SAE 40 oil viscosity measurements as well as a curve fit equation are shown in Figure 3.3.

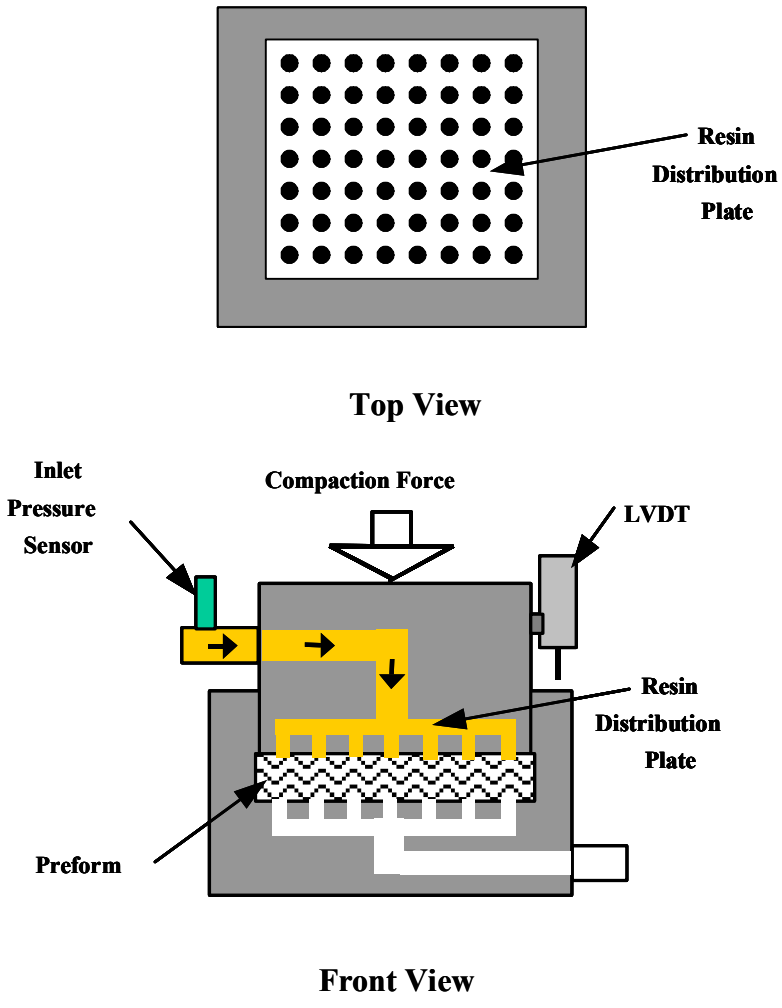

Figure 3.2: Transverse permeability fixture.

Each fabric specimen was tested over a range of fiber volumes. For the MAWK fabric, the specimens were initially compacted to approximately 45% fiber volume, as measured by the

LVDTs on the fixture. After the initial permeability measurements at this initial compaction level, the wetted specimen was further compacted to the next fiber volume level in increments of 2% on up to a maximum of 60%. The biaxial fabric specimens were tested at fiber volumes ranging from 35% to 55%.

Each test cycle at a particular fiber volume consisted of four flow rates of increasing levels. The oil was supplied to the fixtures via a ZENITH® constant-flow metered pump. The flow was set at the pump control unit and measured using a Mettler-Toledo® model (SB1600) balance.

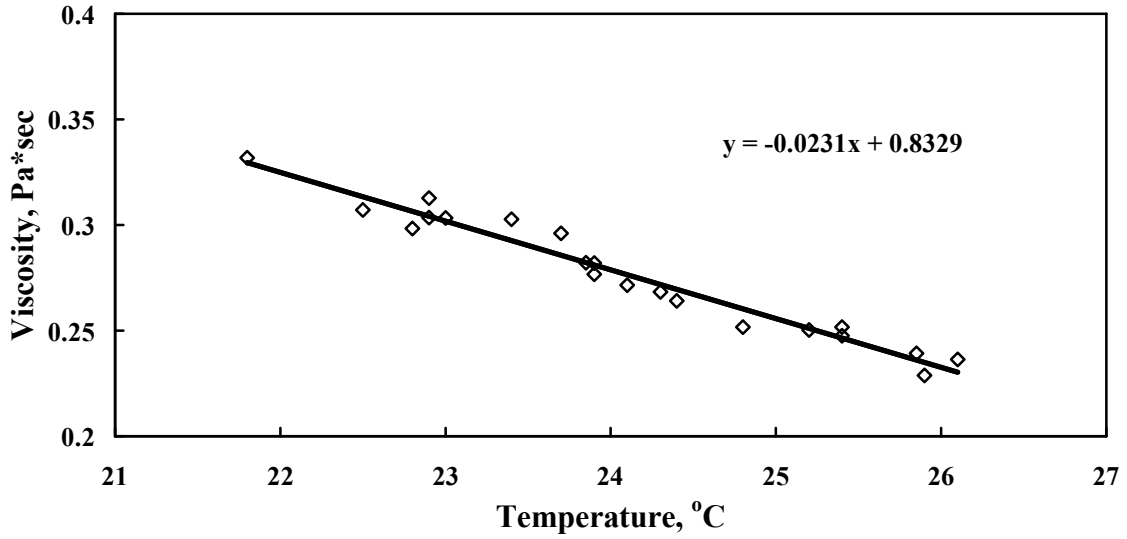

Figure 3.3: Brookfield viscosity versus temperature results for SAE 40 motor oil.

The resulting flow rates over a range of pump setpoints are displayed in Figure 3.4. To maintain flow front pressures below 101.5 kPa, most of the in-plane experiments were carried out at flow rates less than 3.5 cc/min, while the through-thickness permeabilities were found using flow rates between 2.0 and 6.5 cc/min. Flow rates greater than 8.5 cc/min were necessary to develop any measurable pressure when determining both the in-plane and transverse permeabilities of the distribution media material.The constant flow rate at each pump setting corresponded to a build up of fluid pressure at the entry gate/channel of the

preform specimen as read by the pressure sensors. Figure 3.5 shows the typical pressure difference (inlet and outlet), ΔP, mass flow rate, M, and thickness, t, data recorded for one test cycle using NATIONAL INSTRUMENTS® data acquisition hardware and LABVIEW® software. The flow rate was held constant until visual inspection of the real-time pressure curve was found to reach steady-state.

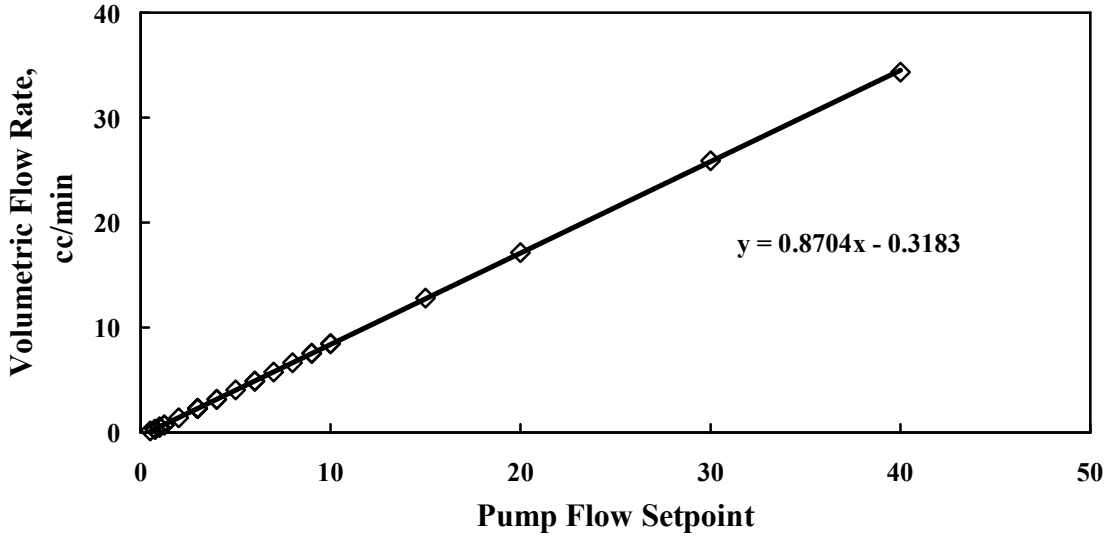

Figure 3.4: Volumetric flow rate as a function of pump setpoint for SAE 40 motor oil.

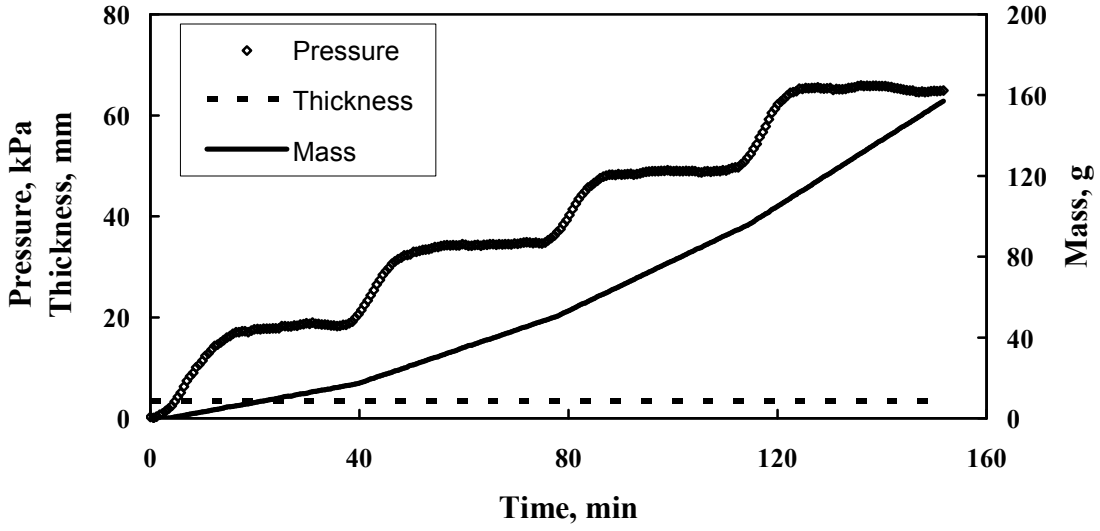

Figure 3.5: Preform thickness, mass evolution and pressure change raw data versus time for a typical permeability characterization test cycle.

Typically, for in-plane characterization the time to reach steady-state ranged from 20 to 60 minutes depending on the thickness of the specimen and fiber volume fraction level. After reaching steady-state, the flow rate was increased to the next level until all four levels were completed. The pressure corresponding to the highest flow rate for each cycle never exceeded 101.5 kPa.

3.3 Results

As stated previously, specimens containing multiple stacks of the MAWK material were tested in an effort to determine the effects of preform thickness on permeability resulting from the inter-stack influence on the fiber volume found in the compaction experiments. These specimen sets are designated “one”, “two”, “four”, “eight” and “sixteen stacks” for the MAWK material as well as “ten” and “twenty layers” for the biaxial preform material. Multiple specimens were cut and individually tested over a range of fiber volumes for each of these sets. The fiber volume fraction, V_f, is calculated using the following expression:

$$V_f = \frac{FAW}{t * \rho_F} \tag{3.3}$$

where FAW is the fiber areal weight of the preform specimen and ρ_F is the density of the carbon fiber and t is the measured preform thickness.The superficial or filter velocity, q, is calculated as:

$$q = \frac{M}{\rho_R A} \tag{3.4}$$

Where ρ_R is the density of the fluid, M is the measured mass and A is the cross-sectional area of the preform normal to the fluid flow direction. The permeability constant, S, is then calculated at each compaction, or thickness, level from Darcy's Law:

$$S = \frac{q\eta L}{\Delta P} \tag{3.5}$$

Where η is the viscosity of the fluid, ΔP is the measured pressure difference and L is the length of the preform specimen. The permeability was determeined over a range of fiber volume fractions for each specimen set using data from multiple tests. A power law equation was used to fit the permeability data as a function of the fiber volume fraction:

$$S = a(V_f)^b \tag{3.6}$$

Where S is the permeability in m^2, V_f is the fiber volume fraction and a and b are the empirical constants. The resulting permeability versus fiber volume fraction curves are shown for each specimen set along with the model fit and error in figures A15 through A33 in the appendix. Figure 3.6 depicts the model fit relations for the MAWK specimen sets for one, two and four stacks in the in-plane, *x-direction*. In comparing these relations it would appear that the same trend seen in the preform compaction characterization has developed. From these curves it would appear that there is an interstack influence on the permeability.

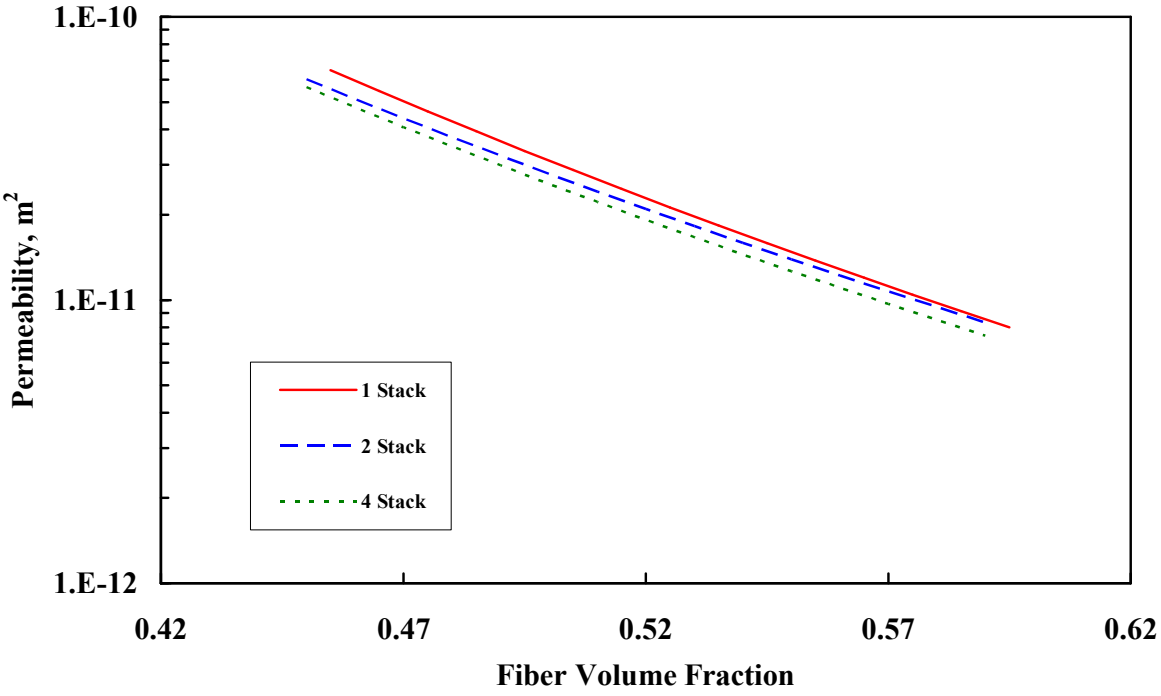

Figure 3.6: Permeability model fit results for S_{xx} of MAWK one, two and four stacks.

In the compaction characterization the ability of the MAWK fabric to nest and reach higher fiber volumes at a given compaction level was found to increase as more stacks are added to the specimen. It is assumed that this is due to an improved nesting capability at the interstack, or between-stack, region. It was hypothesized that the higher degree of nesting in this region would translate to a lower porosity at the interstack region and, therefore lower permeability values, as the amount of stacks in a specimen were increased. For the relations in Figure 3.6 the permeabilitiy decreases as the number of stacks increase.

The resulting model fit relationss from multiple tests of these eight and sixteen specimen sets are added to the results and compared in Figure 3.7. The same trend was not seen when this data is included in the comparison despite repeating tests and careful scrutiny of the test procedure. Therefore, an average power law relation that was fit to all of the in-plane, S_{xx}

data is shown in Figure 3.7. The constants, a and b, from the empical curve-fits of each specimen stack set as well as the average fit are included in Table 3.1.

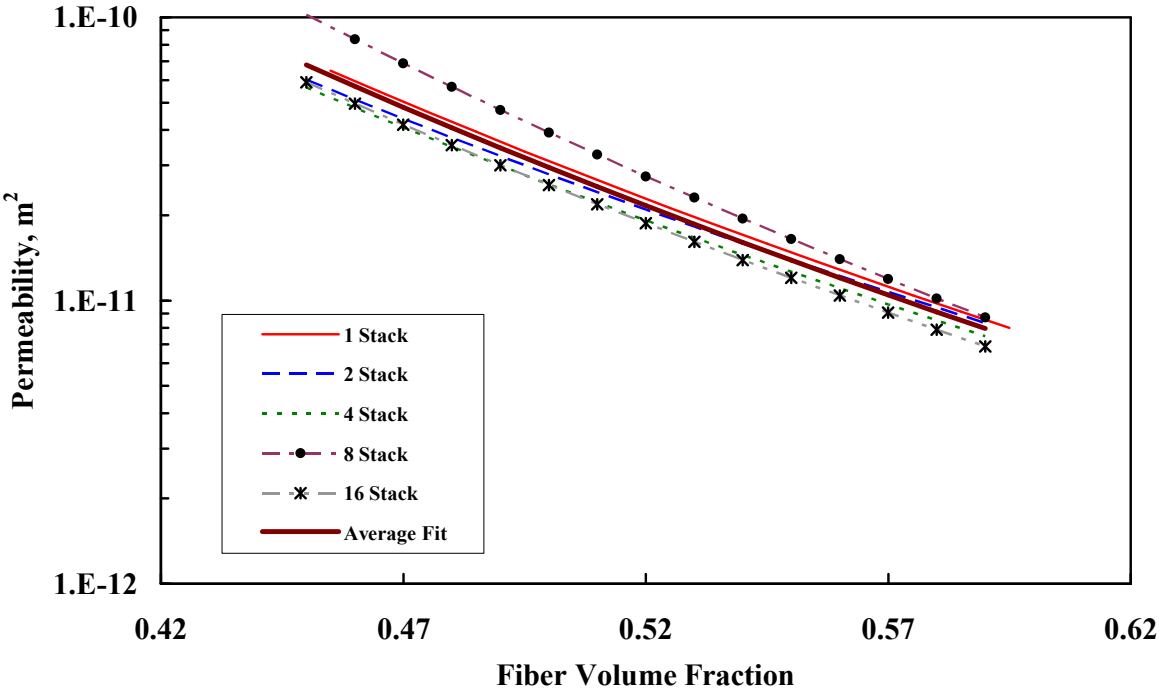

Figure 3.7: Permeability model curve-fit results for S_{xx} of MAWK one, two, four, eight and sixteen stacks and an average fit curve of all results.

Figure 3.8 and Figure 3.9 compare the permeability model fit curves for each of the MAWK stack sets in the *y* and *z*-direction, respectively. The comparison of the in-plane, S_{yy}, model fit curves in Figure 3.8 does not result in any noticible trend relating to the possible interstack influence found in Figure 3.6. The resulting relations shown in Figure 3.9 for the transverse permeabilities of the MAWK fabric do show the same trend for the one, two and four stack specimen sets that were evident in the in-plane, S_{xx}. The transverse permeability for one, two and four stacks was found to increase with increasing stacks, or interstack regions. However, the resulting relations from the model fit for eight and sixteen stacks again do not support this trend. It should also be noted that, although the scatter found in the

error analysis of all of the results was as small if not smaller than previous work [3.8-3.11 and 3.15], the interstack trend found from curve fitting the model equation tends to fall within the range of scatter when comparing between stack sets. The empirical model curve fit constants for the in-plane and transverse permeabilities for all stack sets as well as the average fits are included in Table 3.1.

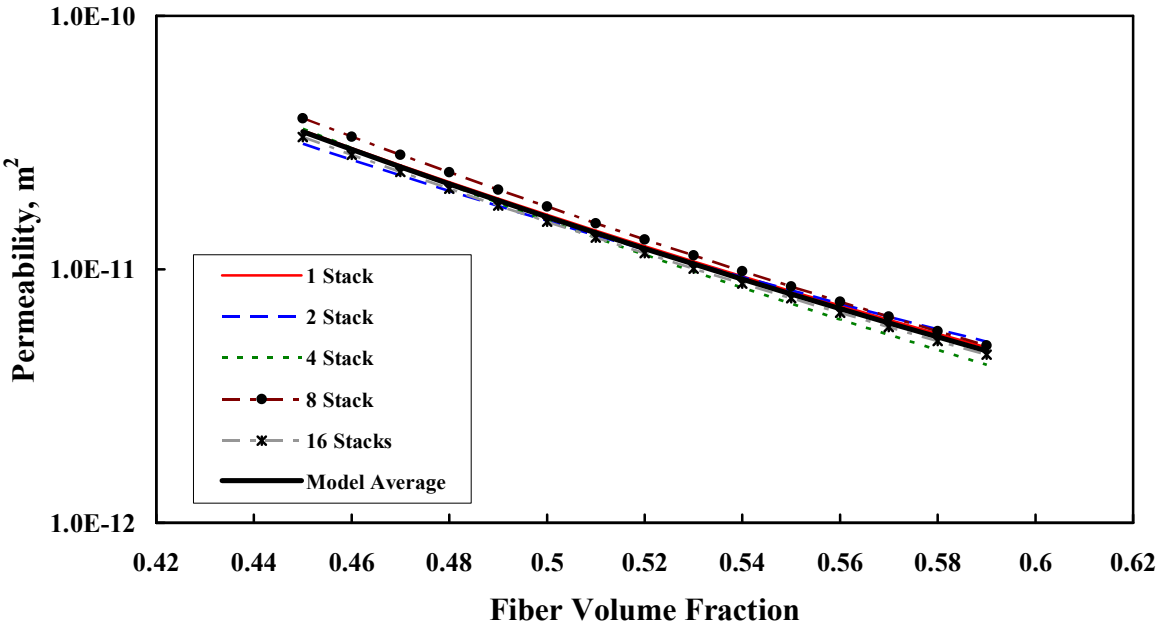

Figure 3.8: In-plane, S_{yy}, permeability model fit results for MAWK one, two, four, eight and sixteen stacks and an average fit relation of all results.

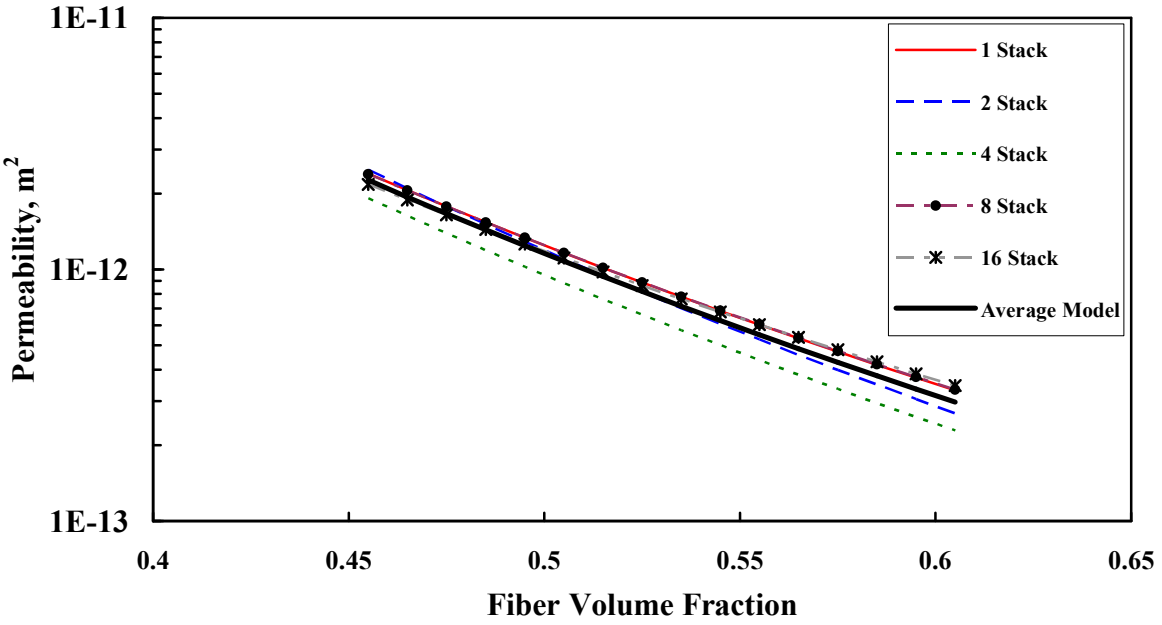

Figure 3.9: Transverse, S_{zz}, permeability model fit results for MAWK one, two, four, eight and sixteen stacks and an average fit relation of all results.

In Figure 3.10, the resulting average relations are compared for the MAWK in-plane permeabilities, S_{xx} and S_{yy}, and the transverse, S_{zz}. As expected the S_{yy} values are slightly lower than the S_{xx} due to the greater number of 0^o fiber tows in the x-direction of the fabric architecture. The S_{zz} values were found to be over an order of magnitude lower than the in-plane values. A lower transverse permeability is generally the case with all continuous fiber preforms due to the lower porosity in that direction of flow [3.8].

In order to more readily understand the influence of the interstack region with regards to the compaction and permeability response of the fabric, and therefore the flow predictions made in FEA analysis, it may be more appropriate to view the permeability as a function of the compaction level of the preform specimens. Attempts were made to run permeability characterization experiments where the compaction loads were used as the independent variable rather than thickness, i.e., fiber volume. These attempts failed due to the nature of

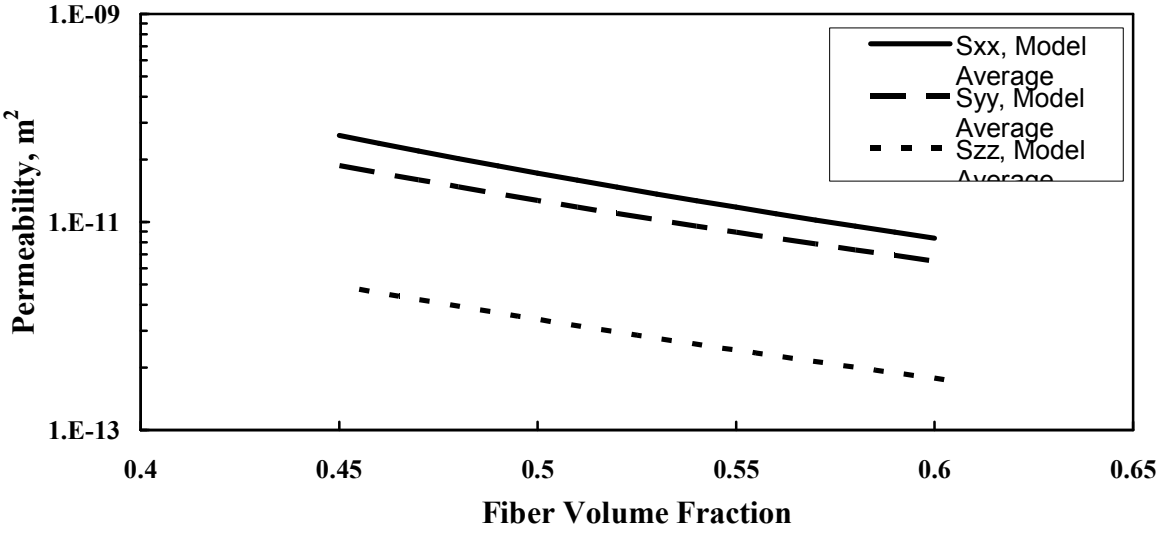

Figure 3.10: MAWK in-plane permeabilities, S_{xx} and S_{yy}, and transverse permeability, S_{zz}, average model fit results.

the permeability fixture design. The plunger, or ”male”, portion of the fixture is designed to seal to the mold cavity, or “female,” portion of the fixture via a rubber gasket. Therefore, the loads necessary to compact and reduce the thickness of the preform were influenced by the variable loads necessary to seal the plunger as it traveled into the cavity. However, using the resulting equations from the compaction characterization described in the previous chapter, the compaction pressures the specimen experiences to reach a particlar level of fiber volume are back calculated and used for comparison in Figures 3.11, 3.12 and 3.13. The values of permeability are generated from the average values of permeability fitted from the relations in Figures 3.8, 3.9 and 3.10. Therefore, when the results of the compaction behavior characterization and the permeability characterization are combined so that the permeability of each stack set is plotted versus the compaction pressure, the influence of increasing the interstack region and its effect on the flow characteristics of the preform is more apparent.

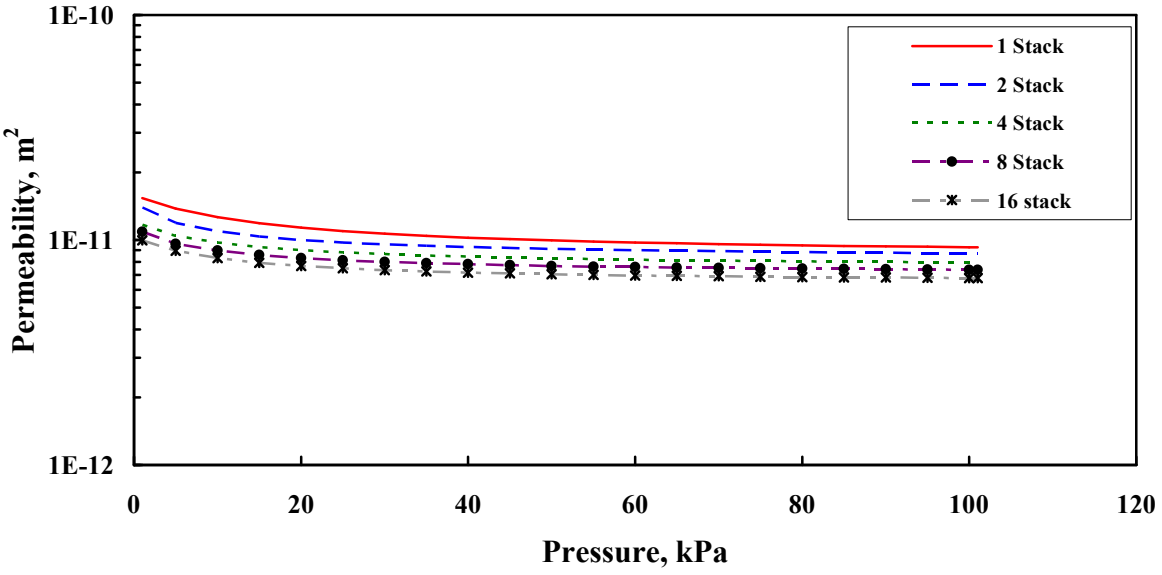

Figure 3.11: MAWK in-plane permeability, S_{xx}, versus pressure values generated from compaction models.

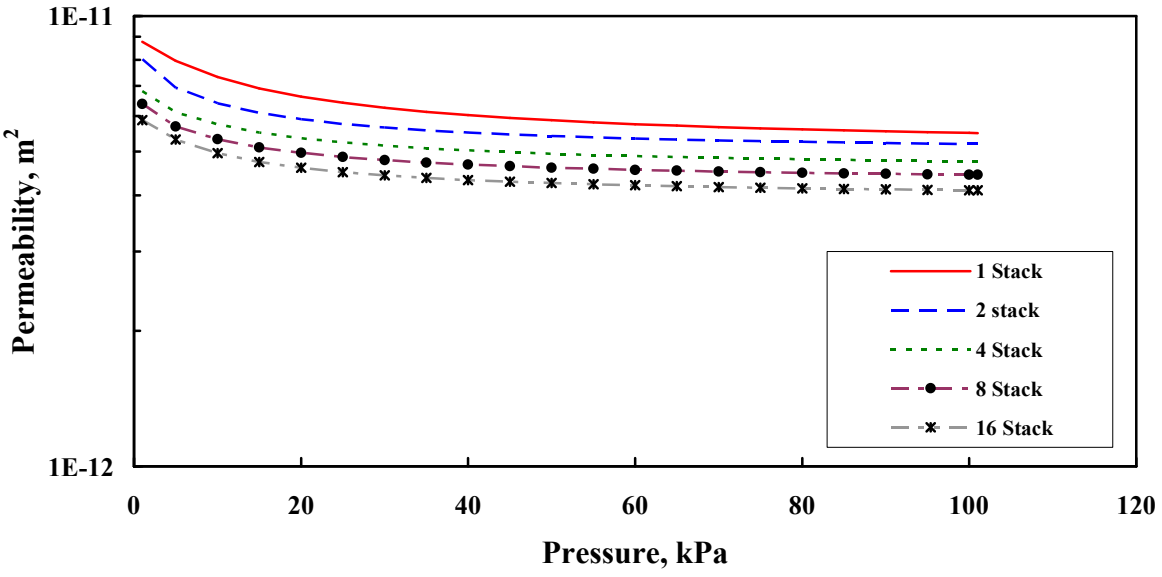

Figure 3.12: MAWK in-plane permeability, S_{yy}, versus pressure values generated from compaction models.

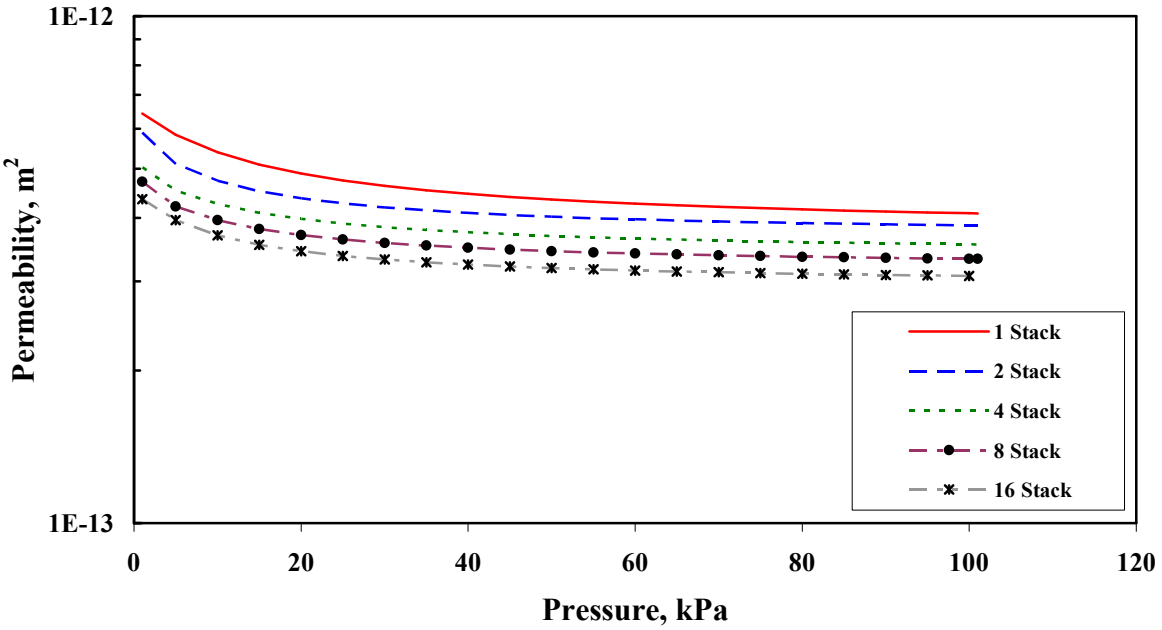

Figure 3.13: MAWK transverse permeability, S_{zz}, versus pressure values generated from compaction models.

The in-plane and transverse permeabilities of the biaxial fabric were also measured. The results, including the power-law curve fit and corresponding error difference are shown in Figures A3.16-A3.20 of the Appendix. Figure 3.14 compares the in-plane permeability, S_{xx} or S_{yy}, of the 10- and 20-layer specimen sets as well as the scatter. There does not appear to be any noticible change in permeability with the increase in number of layers. However, the scatter found in the data for the 20-layer specimen set is about twice that of that found when curve fitting the permeability results for the 10-layer specimens. It is proposed that the reason for the error is due in part to the poor handleability of the fabric. Since the biaxial fabric is a simple woven and not knitted fabric, handling the material, even very carefully, results in disruption of the tow alignment. Loss of tows from the cut edges is common both while cutting and when loading the specimen into the fixture cavity.

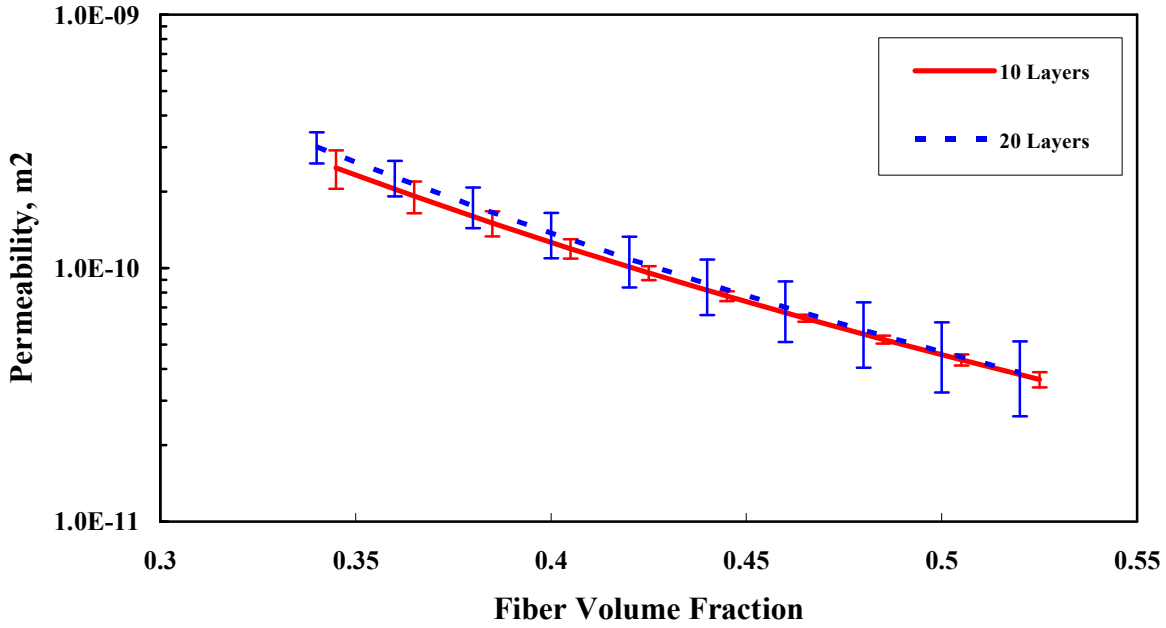

Figure 3.14: In-plane permeability, S_{xx} or S_{yy}, model fit and error for ten and twenty layers of biaxial fabric.

This would necessarily have some influence on the repeatability of permeability values found in experimental characterization. Increasing the number of layers is shown to increase the magnitude of the error found in the characterization tests. The transverse permeability model fit curves are shown in Figure 3.15. While the difference in the magnitude of the error is not as marked in these results, the 20-layer specimen curve fit analysis had an increased amount of scatter when compared with the characterization of the ten layer specimens. The reason for pointing out this repeatability problem is to stress the importance of careful handling of this material when used in laying-up parts for infusion. The history of the material including shipment, cutting, and placement on the tool can influence its infusion characteristics as well as its final performance as a structural component. As in the work described in Chapter 2, no trends were noted regarding the effect of increasing numbers of layers on fiber volume fraction levels or on the values found for permeability.

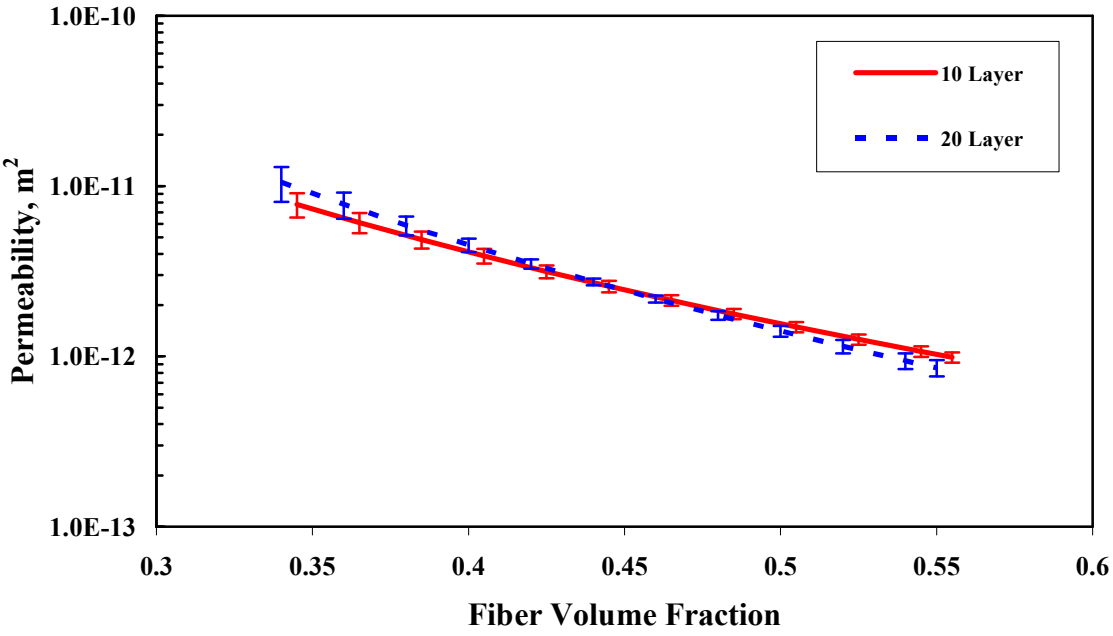

Figure 3.15: Transverse permeability, S_{zz}, model fit and error for 10- and 20-layers of biaxial fabric.

Figure 3.16 shows the average values calculated from data found for both the ten and twenty layer biaxial specimens for both in-plane and transverse permeability. The transverse permeability of this fabric was found to be more than an order of magnitude smaller than the values found for the in-plane permeability over the range of fiber volumes tested. The results of the curve fitting analysis for the ten and twenty layer specimens as well as the empirical model constants for the average curve fits are included in Table 3.1.

The in-plane and transverse permeability of the release film and the three layers of distribution media were also characterized. Results from the compaction experiments carried out on these materials showed that there was no change in thickness in the pressure range of 0.0 to 101.5 kPa. Therefore, the porosity of the material is assumed to be constant. Experiments were carried out using the same permeability fixtures as described in Section 3.2. The materials were compacted under approximately 101.5 kPa as read by the compression test frame load sensor and the SAE 40 motor oil was pumped into the fixture

at four different flow rates. Multiple tests were conducted on specimens containing three layers of the distribution media described in Chapter 2. Experiments were also conducted on specimens containing three layers of the media plus a layer of the release cloth, which rests between the media and the fabric preform in and actual part infusion. These values are included in Table 3.2. Due to the high porosity of these materials, combined with the limit of maximum flow rates obtainable with the pump used in the experiments, the maximum pressures differences, ΔP, reached in these charactrizations were typically less than 10.0 kPa whereas, the maximum ΔP of most of the fabric tests approached 101.5 kPa. The results of the characterization showed that the addition of the one layer of release cloth to the three layers of media significantly lowered the transverse permeability value of the specimen and should therefore be used when simulating flow with these materials. Since the porosity of these materials does not change with compaction pressure, the permeability was not fit to an empirical equation and only the values are entered as material input in the 3DINFIL model.

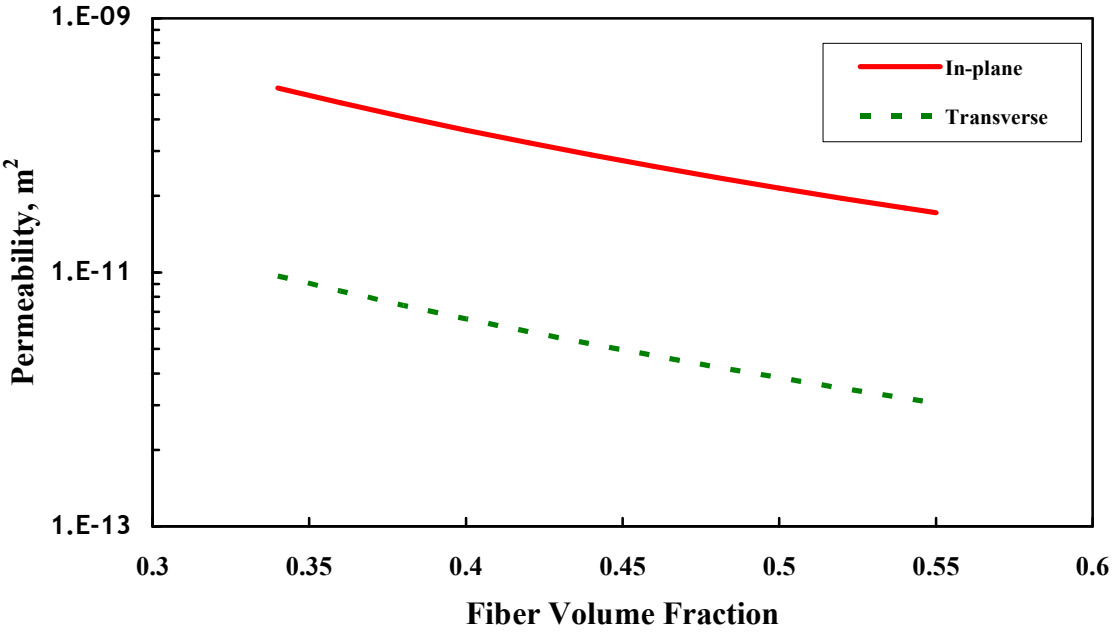

Figure 3.16: Average in-plane and transverse permeabilities of the bixial fabric.

Table 3.1: Permeability as a function of fiber volume fraction and empirical model equation Eq. (3.6) constants for MAWK and biaxial fabrics.

Material Specimen	Empirical Constants					
	In-plane				Transverse	
	S_{xx}		S_{yy}		S_{zz}	
	a	*b*	*a*	*b*	*a*	*b*
MAWK - One Stack	1.40 E-13	-7.798	1.06 E-13	-7.271	9.99 E-15	-6.962
MAWK - Two Stacks	1.78 E-13	-7.294	1.56 E-13	-6.638	5.26 E-15	-7.821
MAWK - Four Stacks	1.47 E-13	-7.446	6.48 E-14	-7.908	5.38 E-15	-7.463
MAWK - Eight Stacks	7.19 E-14	-9.090	8.96 E-14	-7.624	1.03 E-14	-6.919
MAWK - Sixteen Stacks	1.05 E-13	-7.923	9.75 E-14	-7.304	1.34 E-13	-6.460
MAWK - Average	1.23 E-13	-7.910	9.87 E-14	-7.349	9.87 E-14	-7.349
Biaxial - Ten Layers	1.90 E-12	-4.578	1.90 E-12	-4.578	7.62 E-14	-4.351
Biaxial - Twenty Layers	1.64 E-12	-4.828	1.64 E-12	-4.828	3.79 E-14	-5.212
Biaxial - Average	1.77 E-12	-4.703	1.77 E-12	-4.703	5.38 E-14	-4.781

Table 3.2: In-plane permeability, S_{xx}, and transverse permeability, S_{zz}, values of distribution media and release cloth.

Material Specimen	Average In-Plane Permeability, S_{xx}, S_{yy} (m^2)	Average Transverse Permeability, S_{zz} (m^2)
Three Layers Distribution Media (Nylon Mesh)	1.15 E-8	3.55 E-6
Three Layers Distribution Media and One Layer Release Ease® Cloth	9.39 E-9	3.04 E-11

Chapter 4

Matrix Characterization

To ensure successful application of composite structures for aerospace vehicles, it is necessary to develop material systems that meet a variety of requirements. The industry has recently developed a number of low-viscosity epoxy resins to meet the processing requirements associated with vacuum assisted resin transfer molding (VARTM) of aerospace structural components. As part of the effort to further develop the VARTM process, several of these resins are being characterized and selected for use [42]. In addition to the required strength and durability of the polymer matrix, properties that govern the processing characteristics must be considered. A combination of experiments and process models are used to characterize these resin systems and determine the influence of a larger number of polymer properties on final part quality. Further material development and characterization efforts can then be focused on the most important parameters for a given application.

The curing kinetics and viscosity of two of these resins, an amine-cured epoxy system, VR56-4 (Applied Poleramic, Inc.), and an anhydride-cured epoxy system, SI-ZG-5A (A.T.A.R.D. Laboratories), have been characterized for application in the VARTM process. Simulations were carried out using the process model, COMPRO©, to examine heat transfer, curing kinetics and viscosity for different panel thicknesses and cure cycles. Results of these

simulations indicate that the two resins have significantly different curing behaviors and flow characteristics.

4.1 Background

The crosslinked polymer epoxy is derived from reactions of the epoxy group, or epoxide, shown in Equation 2.1 below.

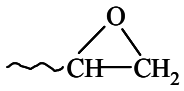

(4.1)

Most commercial epoxy resins are synthesized from the reaction of two or more moles of epichlorhydrin and one mole of bisphenol A [43]. This results in the uncrosslinked resin diglycidyl ether of bisphenol A (DGEBA) shown in Equation 4.2 with the epoxide group at each end. With n=1, this is the most basic form of liquid epoxy resin.

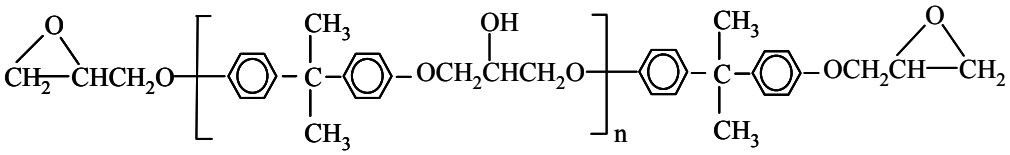

(4.2)

The functionality and reactivity of the epoxy resin molecule is, in part, dictated by the epichlorhydrin monomer, which can have two or more epoxide groups at varying locations, depending on its prior reaction with a variety of hydroxy, carboxy and amino compounds.

The resulting epoxy resin can then be reacted with a curing agent to form a solid crosslinked epoxy network. Several basic curing chemistries may be chosen according to factors such as the steric nature and functionality of the epoxy resin as well as the desired mechanical and thermal properties of the cured epoxy [44]. Of interest here are the amine and anhydride type curing agents.

Aromatic primary amines such as m-Phenylenediamine (m-PDA) require the presence of a hydrogen donor compound such as a hydroxyl group(benzene, acetone, water) in order to react with the epoxy ring. Equation 4.3 shows the addition-reaction of a primary amine (RNH_2) with the epoxy ring, where, for m-PDA, $R = H_2NC_6H_4$.

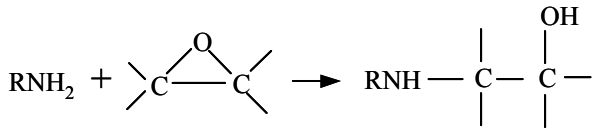

(4.3)

When this occurs, the initial reaction product is a hydroxyl and a secondary amine (RNH). The secondary amine and the hydroxyl can then open the epoxy ring of another DGEBA molecule, creating a crosslink between the two as shown in Equation 4.4, where R=C_6H_4. This reaction continues throughout the bulk of the epoxy resin/curing agent mixture with the primary amines usually reacting twice as quickly with the DGEBA molecules as the secondary amines react [43].

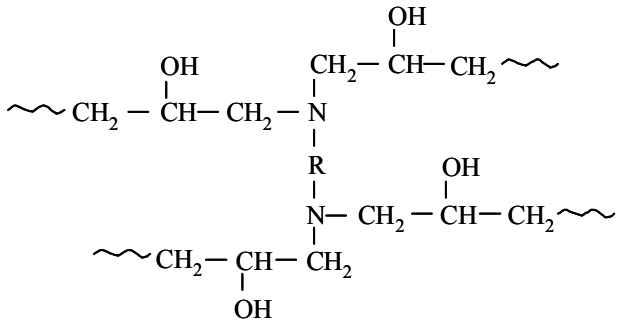

(4.4)

This reaction results in a tertiary amine. The resulting tertiary amine, in this case, usually lacks the reactivity to continue catalytic activity. Some secondary aromatic amines such as diethanolamine and also tertiary amines such as dimethylethanolamine and diethylethanolamine can be introduced to the epoxy resin to act as the sole curing agent [43]. The tertiary amine is an organic base containing an atom with an unpaired electron in its outer orbital. In this case, the tertiary amine approaches one of the carbon atoms of the epoxide group and, in the presence of a hydroxyl group, bonds to the oxygen atom of the epoxy. From this an anion is generated, which is capable of opening a second epoxy ring, and thus continues the crosslink reaction.

The other epoxy system investigated uses anhydride curing agents. Cyclic anhydrides, such as the aromatic phthalic anhydride (PA), will not react directly with the epoxide group. The anhydride ring must first be opened by active hydrogen present as water, hydroxyls, or a

Lewis base. The addition of a hydroxyl group to the PA compound, shown in Equation 4.5 with R= ~CH_2-CH-CH_2~, results in the organic acid carboxyl group which can then react with the DGEBA molecule.

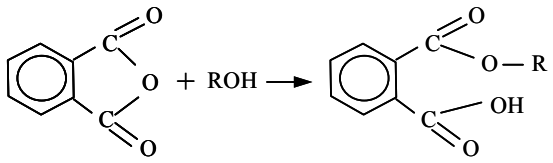

(4.5)

The crosslinking epoxy reaction is quite complex, involving addition esterification with the formed carboxyl group and/or by condensation reactions of pendant hydroxyl groups [43]. The un-catalyzed epoxy-carboxyl reaction shown in Equation 4.6 will occur slowly without the presence of proton donors [45].

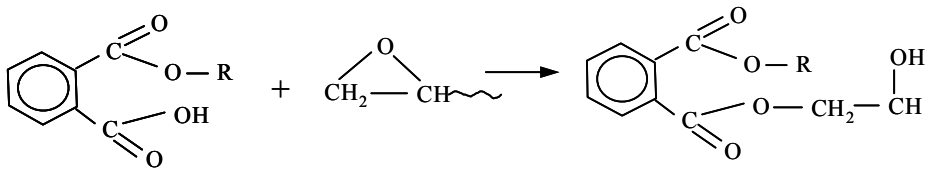

(4.6)

The final crosslinked, phthalic anhydride-cured epoxy is shown in simplified form in Equation 4.7, where R=C_6H_4.

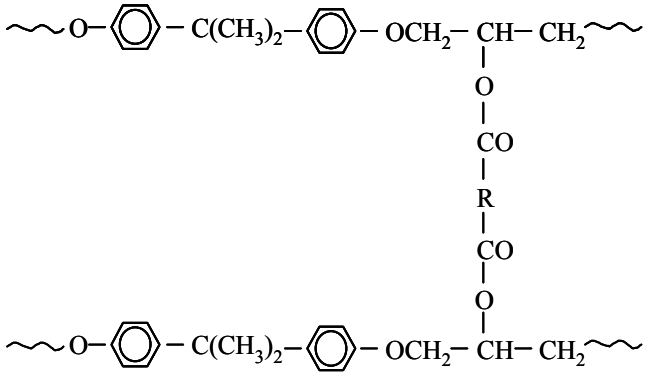

(4.7)

Some generalizations have been made in the literature regarding the comparison of amine-cured versus anhydride-cured epoxies [43] and [45]. The amines are more toxic causing skin and respiratory irritation, however, this can be alleviated if the amines are used in the

form of adducts. The stoichiometric ratio of the epoxy/amine reaction requires careful measurement of the epoxy resin and curing agent. The aromatic amines offer superior resistance to chemical attack. Anhydrides reportedly give lower exotherms during cure and generally provide better thermal stability and electrical insulation. The majority of anhydride-cured epoxies are more brittle than the amine-cured. Toughening with flexibilizers generally results in lowered heat resistance.

Both the amine-cured epoxy VR-56 and the anhydride-cured epoxy SI-ZG-5A are proprietary blends of several different epoxy resins and several different amine and anhydride curing agents, respectively. The epoxy resins present in these blends may have different functionalities and reactivities and the curing agents may be present in liquid eutectics and adducts. Cure kinetics characterization can be difficult due to the complex and proprietary nature of these blended resins. In addition, the generalizations found in the literature may or may not be relevant to these particular epoxy resin systems.

4.2 Matrix Characterization

Accurate prediction of many of the key material properties required in composites process models such as resin viscosity, modulus development and cure shrinkage depend on an accurate knowledge of the cure state of the resin during processing [46-48]. Furthermore, an understanding of resin viscosity behavior is also required to predict the flow of resin during VARTM infiltration [49]. Cure kinetics and viscosity models are obtained for the resin using a combination of isothermal and dynamic differential scanning calorimeter (DSC) and parallel-plate rheometer scans, respectively.

4.2.1 Initial Panel Cure Characterization A series of experiments were performed to ascertain the influence of both the resin system and the effects of part thickness and fiber volume, i.e., increasing number of the SAERTEX® MAWK stacks, on the part temperature during composite cure. MAWK preform specimens 30.5 cm x 30.5 cm containing two, four and eight stacks were laid-up on a 1.27 cm thick aluminum tool. A 30 gage type K thermocouple was placed in the center of the part with respect to both the area and the

thickness. The preforms were bagged, evacuated, and debulked under full vacuum, 101.5 kPa, for approximately twelve hours prior to infusion. To reduce the effects of oven temperature variability, two panels were infused at the same time on the same tool and the parts were spaced 10.0 cm from each other. This resulted in the part thermocouples being 40.0 cm apart from each other. The specimens were infused with each of the resin systems, SI-ZG-5A and VR-56-4, until the preform was observed to be fully wetted. The resin line was closed while the vacuum line was left open for an additional 15 minutes. After clamping the resin line, a second bag was placed over the parts, clamped resin and vacuum lines, and the infusion bag to prevent leaks and ensure that the parts remained under a compaction force during cure. The oven cure cycle included two 175 min isothermal holds at 65^{o}C and 121^{o}C and the oven temperature was ramped to these holds at 1.1^{o}C/min.

The resulting temperature evolutions from these experiments are shown in Figure 4.1 for two, four and eight stacks specimens of MAWK fabric with the SI-ZG-5A resin system and in Figure 4.2 for the VR-56-4 system. As there is little variation in laboratory temperature, the oven temperature was not found to vary from test to test. The oven curve shown is plotted from the data taken from the four stack test. In each of the curves an exothermic reaction was found to take place during the first temperature hold at 65^{o}C. This is noted by the part thermocouple displaying a higher temperature reading than the oven temperature.

It was thought that the increasing fiber volume trend shown in the compaction studies would result in a decrease in exotherm temperature as the amount of stacks were increased. However, no temperature trend with respect to fiber volume is observed in the curves generated using this experimental technique. In fact the eight-stack specimen curves for each resin system were each found to reach the highest temperatures during the exothermic reaction at the 65^{o}C hold. Because these panels contain a greater mass of resin, the initial cure rate is higher and, therefore, due to heat transfer effects, would necessarily reach higher temperatures.

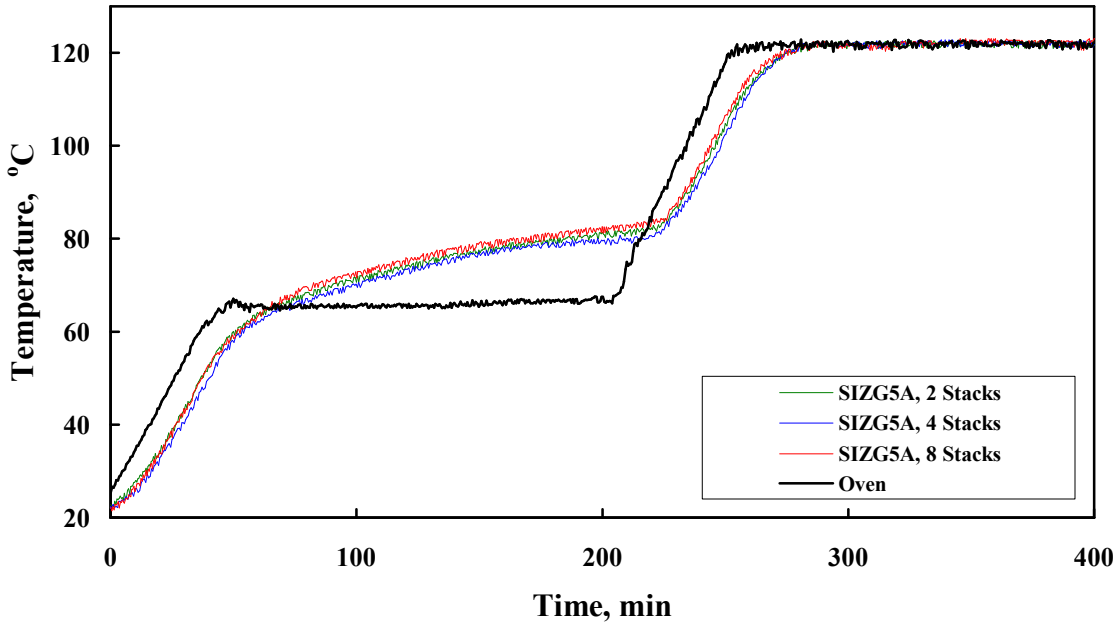

Figure 4.1: Part temperature evolution during cure of MAWK panels with SI-ZG-5A epoxy.

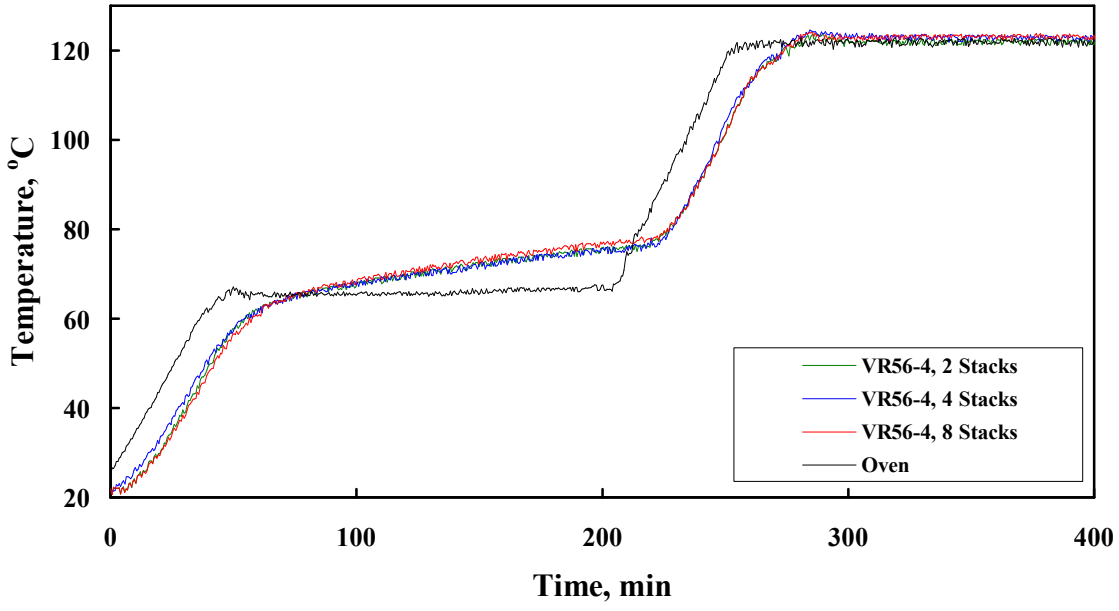

Figure 4.2: Part temperature evolution during cure of MAWK panels with VR-56-4 epoxy.

This experiment is not an effective technique to indicate the fiber volume influence on part temperature evolution during cure. There is, however, an obvious difference in the temperature evolution when comparing the specimens infused with the amine cured VR56-4 epoxy resin versus those fabricated using the anhydride cured SI-ZG-5A epoxy. The average part temperature from the curves in Figures 4.1 and 4.2 are plotted in Figure 4.3.

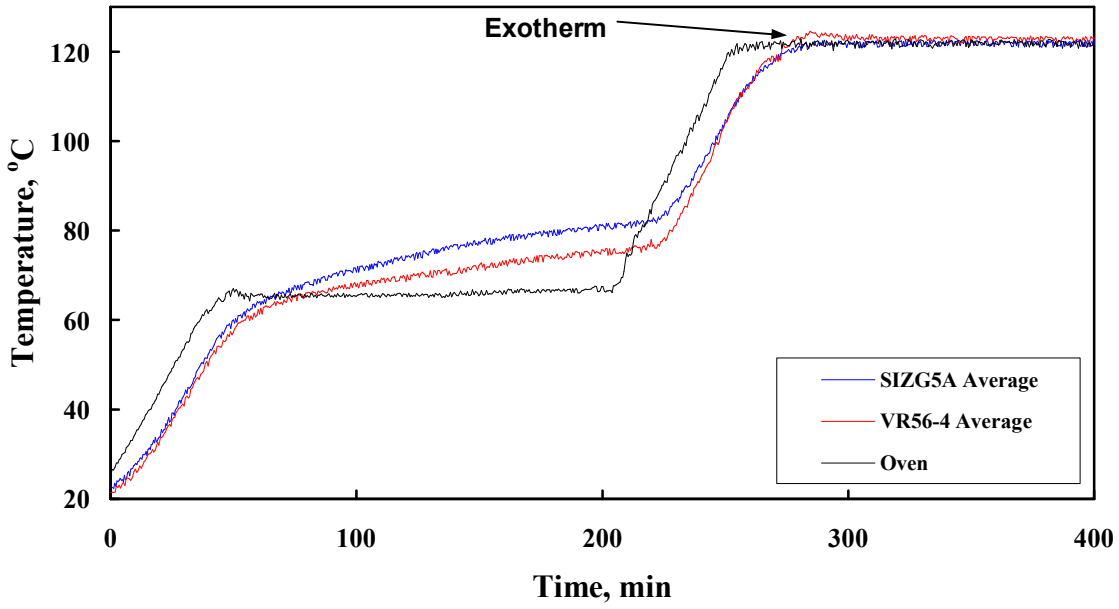

Figure 4.3: Average part temperature evolution during cure of MAWK panels with SI-ZG-5A and VR-56-4 epoxy resins.

From these curves it is observed that the SI-ZG-5A panels were found to reach higher exothermic reaction temperatures during the first isothermal hold. In addition, it appears that the VR-56-4 resin cure reaction continues for a longer period of time as noted by the small exotherm at the start of the second temperature hold. The curves indicate the importance of developing a more thorough understanding of the curing kinetics for each of the epoxy resin systems.

4.2.2 Cure kinetics model All tests were performed on a Shimadzu DSC-50 differential scanning calorimeter. The total heat of reaction (HR) was measured from dynamic scans at 1.1°C/minute from room temperature up to 250°C. The isothermal tests were performed at temperatures ranging from 60°C to 140°C. In these tests, the specimens were dropped into a DSC cell that had been heated to the desired temperature. The specimens were maintained and scanned at these temperatures for up to 12 hours, and then rapidly cooled. The isothermal tests were followed by a dynamic scan at 1.1°C/minute to measure the residual heat of reaction.

Raw data from the DSC experiments consisted of measurements of heat flow and total resin heat of reaction as calculated by the apparatus software. From the heat flow curves obtained from the dynamic runs shown in Figure 4.4, H_R for the anhydride-cured SI-ZG-5A and the amine-cured VR-56-4 were determined to be almost identical: 350 kJ/kg and 353 kJ/kg, respectively. However, the peak shape and location for each resin system was different. The peak for SI-ZG-5A occurred at a lower temperature (112°C) compared to VR-56-4 (120°C). Furthermore, the width of the exothermic peak was narrower for SI-ZG-5A indicating that the reaction rate was higher compared to VR-56-4. From the baseline heat flow ($\dot{q}_{baseline}$) and the total heat flow, the resin cure rate was then determined for each epoxy using:

$$\frac{d\alpha}{dt} = \frac{(\dot{q}_{baseline} - \dot{q}_{in}) / m_{sample}}{H_R /(1-\alpha_0)} \tag{4.8}$$

where, $\dot{q}_{in}$ is the measured heat flow, m_{sample} is the sample mass and α_0 is the starting resin degree of cure, assumed to be 0.01 in all cases. Resin degree of cure as a function of time was determined by integrating the calculated cure rate. From Figure 4.5, two distinct peaks in the VR56-4 isothermal curve can be observed. These two peaks were present to some degree in all of the isothermal scans for this resin.

For SI-ZG-5A, the equation chosen for the cure kinetics model is a modified auto-catalytic equation, modified to account for a shift from kinetics to diffusion control [46].

$$\frac{d\alpha}{dt} = \frac{K\alpha^{m}(1-\alpha)^{n}}{1+e^{C\{\alpha-(\alpha_{C0}+\alpha_{CT}T)\}}} \qquad (4.9)$$
$$K = Ae^{(-\Delta E/RT)}$$

The cure kinetics for the VR-56-4 was more complex. The two peaks in the isothermal heat flow curve shown in Figure 4.5 reveals two separate reactions occurring during cure. It was determined that the first reaction for $\alpha < 0.10$ probably corresponds to the primary amine reaction discussed in Section 4.1. Therefore, an n^{th}-order rate equation (Equation 5.3) was used to calculate $d\alpha/dt$ for $\alpha < 0.10$. For $\alpha \geq 0.10$, the modified, auto-catalytic equation (Equation 4.2) is used to calculate $d\alpha/dt$.

$$\frac{d\alpha}{dt} = A_2 e^{(-\Delta E_2/RT)}(1-\alpha)^{n_2} \quad \alpha < 0.1$$
$$\frac{d\alpha}{dt} = \frac{K\alpha^{m}(1-\alpha)^{n}}{1+e^{C\{\alpha-(\alpha_{C0}+\alpha_{CT}T)\}}} \quad \alpha \geq 0.1 \qquad (4.10)$$
$$K = Ae^{(-\Delta E/RT)}$$

The significance of the various terms in Equations 4.9 and 4.10 is presented in Table 4.1. The activation energies, ΔE and ΔE_2, were calculated from the slope of the natural logarithm of the isothermal cure rate, $\ln(d\alpha/dt)$, vs. $1/T$ at a number of different resin degrees of cure. All other model constants were determined using a weighted least-squares analysis, using data from both isothermal and dynamic DSC measurements.

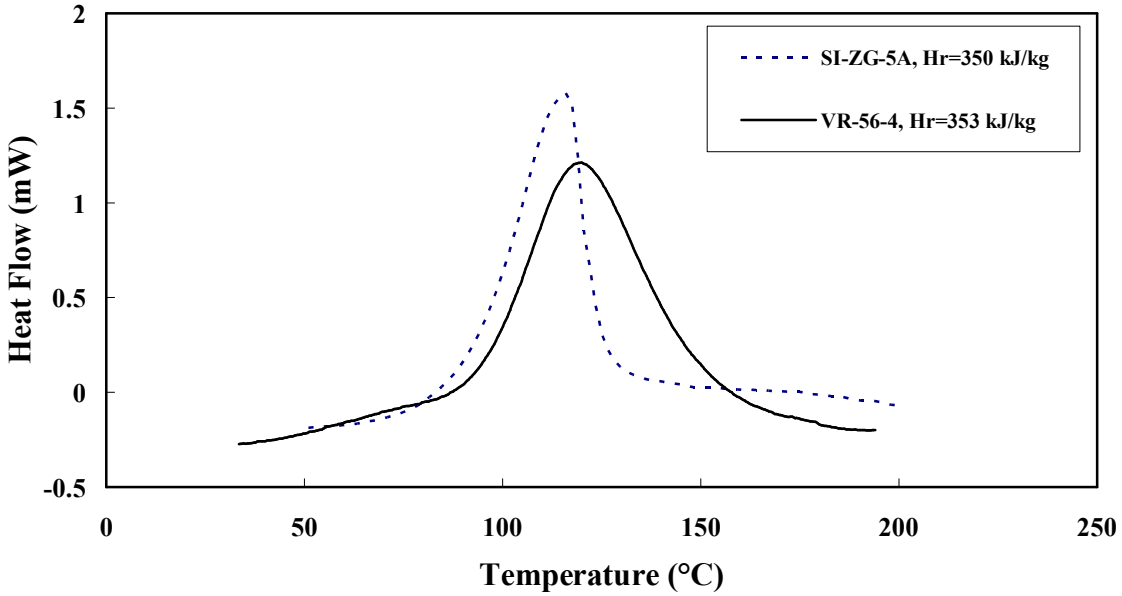

Figure 4.4: Dynamic scans for SI-ZG-5A and VR-56-4 at 1.1 °C/min showing the total heat of reaction.

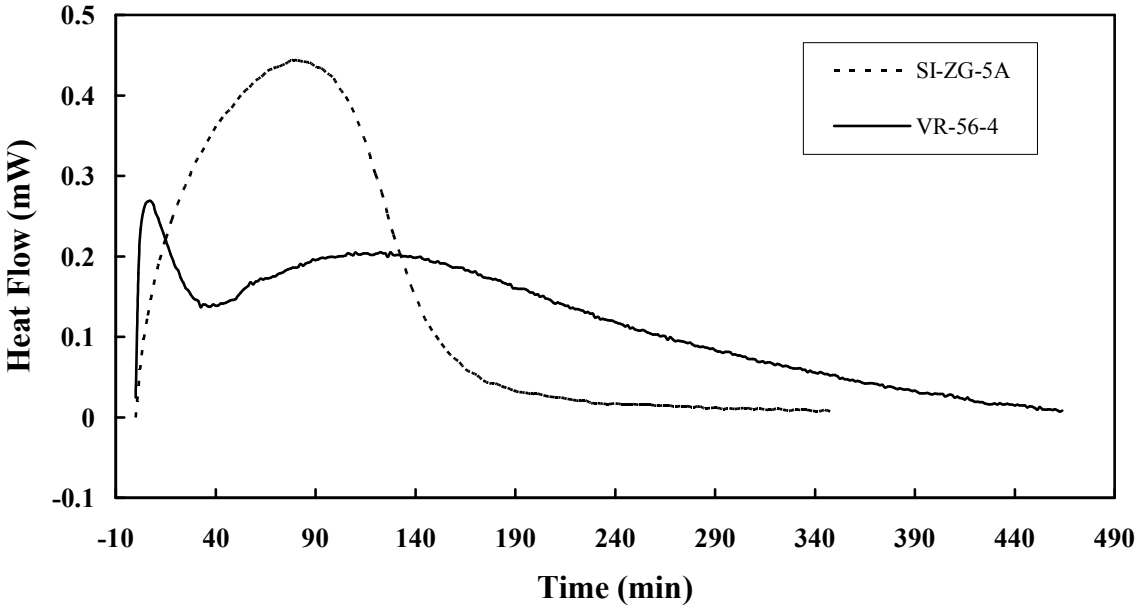

Figure 4.5: Isothermal scans of SI-ZG-5A and VR-56-4 at 80°C for 6 hrs and 8 hrs, respectively.

Table 4.1: Parameters used in SI-ZG-5A and VR-56-4 kinetics model (Equations 4.9 and 4.10).

Parameter	Value	
	SI-ZG-5A	**VR56-4**
Activation energy	ΔE = 61.0 kJ/gmole	ΔE = 48.8 kJ/gmole
Pre-exponential cure rate coefficient	$A = 4.11 \times 10^5$ /s	$A = 2.46 \times 10^3$ /s
First exponential constant	m = 0.551	m = 0.475
Second exponential constant	n = 1.00	n = 1.09
Diffusion constant	C = 40	C = 10
Critical degree of cure at T = 0°K.	α_{C0} = 0.216	α_{C0} = 0.748
Constant accounting for increase in critical resin degree of cure with temperature	$\alpha_{CT} = 1.3 \times 10^{-3}$/K	$\alpha_{CT} = 5.7 \times 10^{-4}$/K
Activation energy for initial reaction	-	ΔE_2 = 47.2 kJ/gmole
Pre-exponential cure rate coefficient (initial reaction)	-	$A_2 = 1.13 \times 10^3$ /s
Exponential constant (initial reaction)	-	n_2 = 1.09

Figure 4.6 compares the model predictions for the rate of cure versus degree of cure for the 100°C isothermal hold. The modified catalytic equation is shown to work very well in both cases. For VR-56-4, the initial reaction occurring at $\alpha < 0.10$ is also well captured. Figures 4.7 and 4.8 show that the models provide an excellent fit to the isothermal cure tests at all temperatures examined. In Figure 4.7, for VR-56-4 the only discrepancy is found at $\alpha > 0.8$ for the 120°C and 140°C case. In Figure 4.8, the only discrepancy between the model and the experiments is found for times greater than twelve hours in the 60°C case. The reason for these deiscrepencies, which seem to occur at the extreme cases, is possibly due to the difficulties encountered when fitting a baseline to the raw data shown in Figure 4.5. For the

higher temperature isothems, a portion of the heat flow data may be lost during initial heating. For the lower temperature isothemal scans, the long duration and shape of the curve make it difficult to exactly fit the baseline, i.e., the fit is somewhat arbitrary.

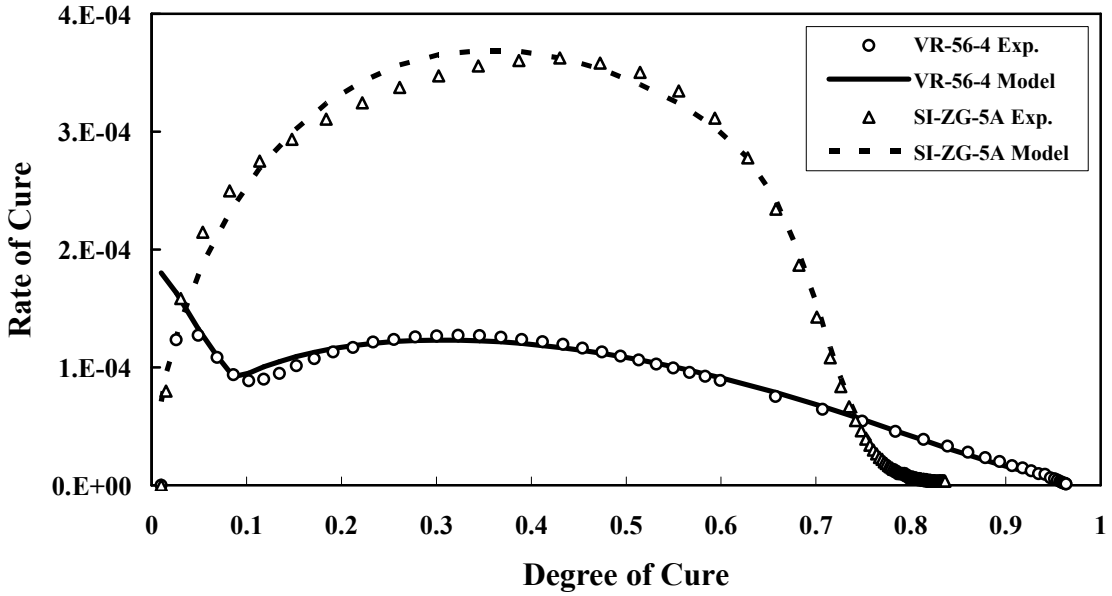

Figure 4.6: Calculated model fits to experimental data for SI-ZG-5A and VR-56-4 at 100°C isothermal cure.

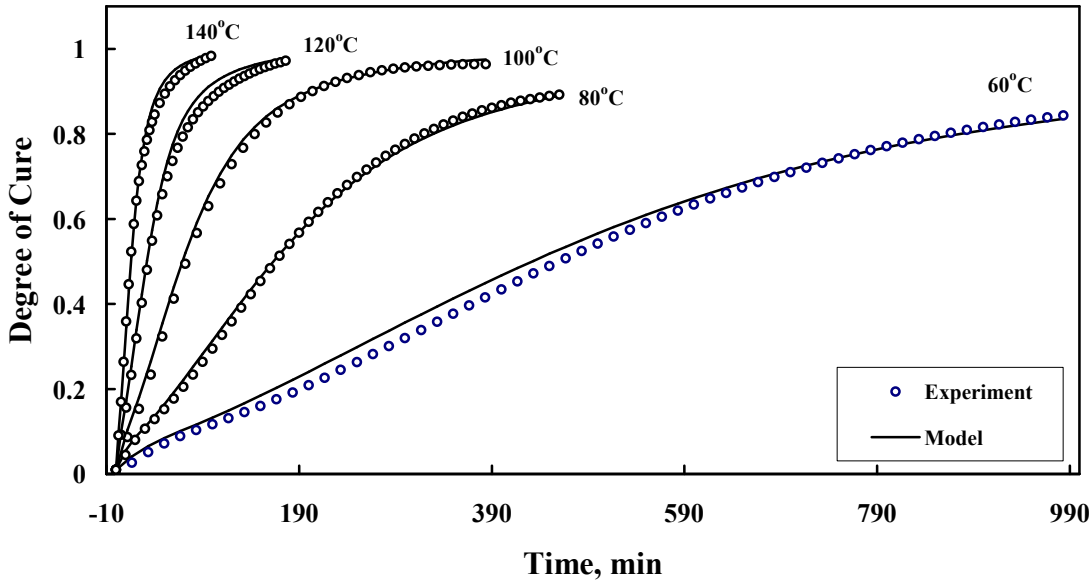

Figure 4.7: Comparison of measured and predicted VR-56-4 resin degree of cure in isothermal curing condition.

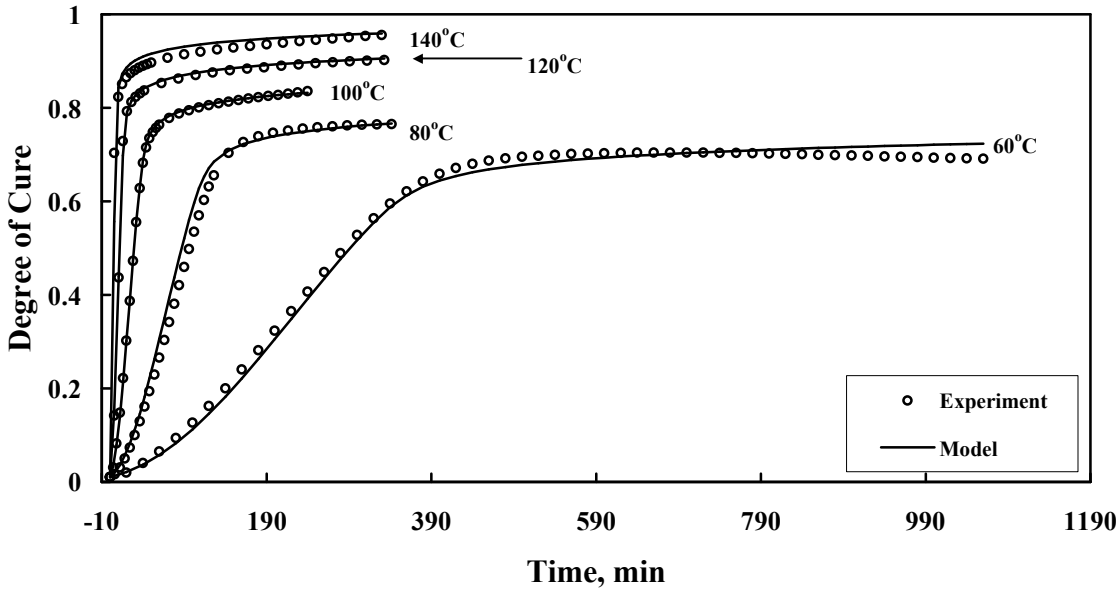

Figure 4.8: Comparison of measured and predicted SI-ZG-5A resin degree of cure in isothermal curing condition.

4.2.3 Viscosity Model An ARES Rheometric System-Five parallel-plate rheometer was used to measure the neat resin viscosity. The viscosity model constants for both resins were determined by a series of isothermal cure tests ranging from 60°C to 140°C. Dynamic cures at 1.1°C/minute and a typical cure cycle test were conducted to validate the models. The samples were sheared between two 30 mm parallel discs. A dynamic or sinusoidal wave torque signal was applied to the sample. The frequency of the signal was 100 rad/s at a maximum shear strain of 10%. The test was stopped when the resin reached its gel point or after twelve hours, whichever came first. Figure 4.9 shows a typical dynamic temperature scan performed with the VR-56-4 resin system. The room temperature viscosity for SI-ZG-5A and the VR-56-4 were measured to be 0.32 Pa·s and 0.42 Pa·s, respectively.

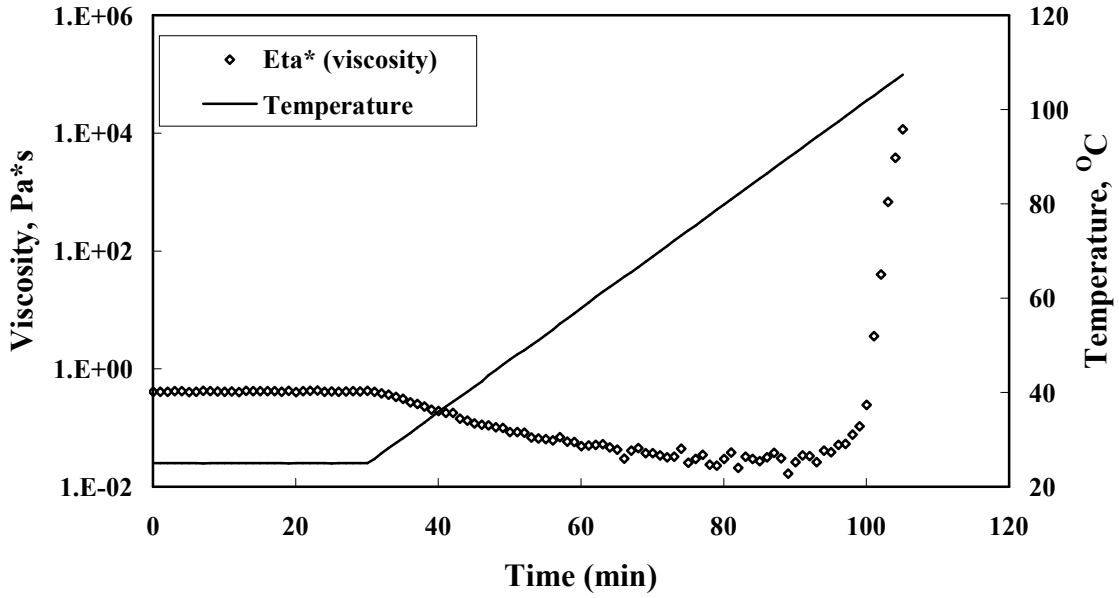

Figure 4.9: Dynamic temperature rheology scan of VR-56-4 at 1.1°C/min, 100 rad/sec.

The viscosity model [49] used in this study is as follows:

$$\mu = A_\mu \exp\left(E_\mu / RT\right)\left[\alpha_g / \left(\alpha_g - \alpha\right)\right]^{(A+B\alpha)} \tag{4.11}$$

where A_μ, E_μ, A and B are experimentally determined parameters, R is the universal gas constant and α_g is the degree of cure at gelation. The slope of a linear regression through the data of lnμ versus $1/T$ at low resin degree of cure ($\alpha \approx 0$) yields the values for E_μ. The results from the dynamic runs at 1.1° C/min were used in this calculation for both resins. Figure 4.10 shows the regression analysis of the portion (0 to 60 minutes) of the raw data curve from Figure 4.9 for VR-56-4. The value of 6432.4 Pa·s·K for the slope of this fit resulted in a calculated value of activation energy, E_μ = 56000 J/g·mol.

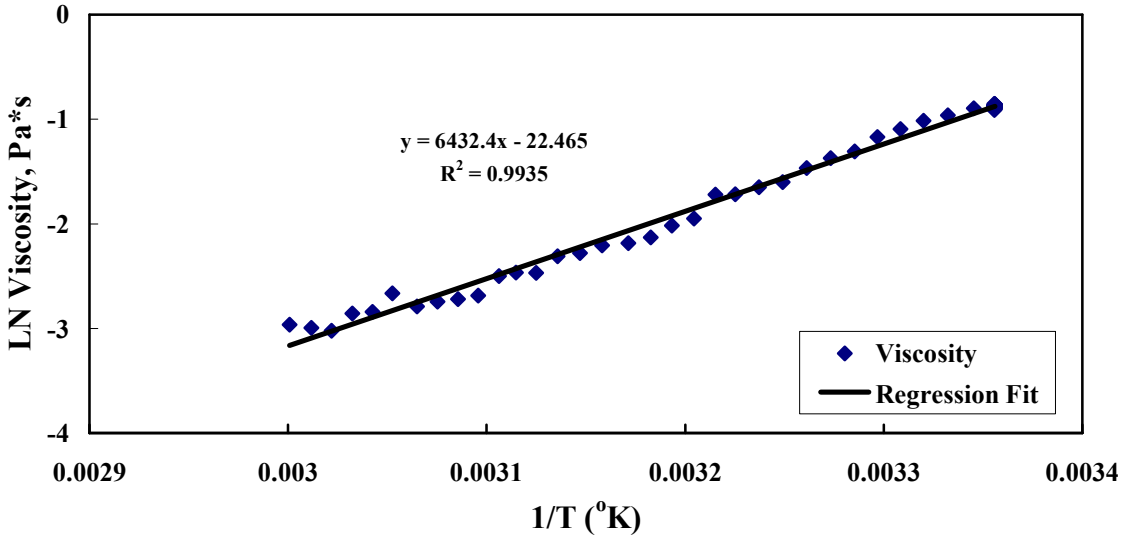

Figure 4.10: Viscosity activation energy determination by regression analysis of portion of dynamic temperature scan for VR-56-4.

The gel point degree of cure (α_g) was evaluated from the crossover point between the storage and the loss modulus (G' and G''). The gel point was 0.60 for SI-ZG-5A and 0.86

for VR-56-4. To evaluate the other constants, A_μ, A and B were curve-fit to the experimental data from the isothermal and dynamic tests. The best-fit constants are given in Table 4.2.

Table 4.2: Parameters used in SI-ZG-5A and VR-56-4 viscosity model (Equation 4.11).

Parameter	**Value**	
	SI-ZG-5A	**VR-56-4**
Activation energy	E_μ = 54803 J/gmole	E_μ = 56000 J/gmole
Pre-exponential coefficient	$A_\mu = 8.3 \times 10^{-11}$ Pa·s	$A_\mu = 6.5 \times 10^{-11}$ Pa·s
First exponential constant	A = 4	A = 4.23
Second exponential constant	B = 6.25	B = 0
Degree of cure at gel point	α_g = 0.60	α_g = 0.86

Figure 4.11 shows the comparison of the model prediction to the experimental data in a typical cure temperature cycle test for SI-ZG-5A and VR-56-4. In both cases, the models capture the ambient viscosity, the reduction in viscosity due to temperature increase, and the rapid increase in viscosity as the resins reach the gel point. Furthermore, for the temperature cycle shown, the VR-56-4 epoxy is found to have a more gradual increase in viscosity during the 66°C hold. This resin must be heated to a higher temperature in order to reach gelation.

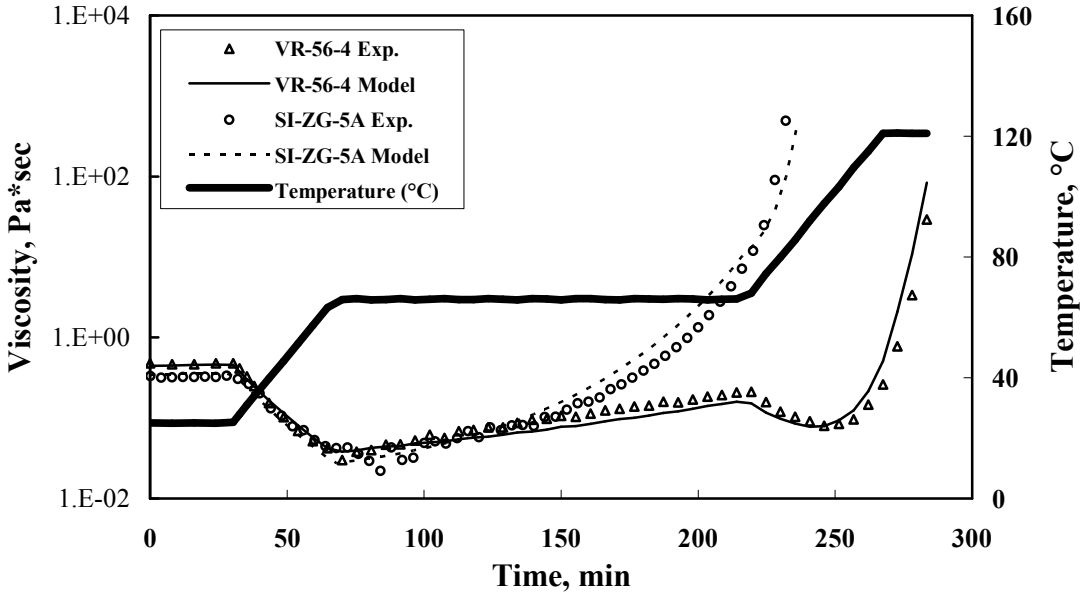

Figure 4.11: Comparison between measured and predicted viscosity for a typical cure cycle test for SI-ZG-5A and VR-56-4.

4.3 Cure Simulations

The difference in curing behavior between VR-56-4 and SI-ZG-5A for typical VARTM panels was investigated using the process model COMPRO© [50]. Cure simulations of 5 mm and 25 mm thick panels were performed. Two different cure cycles with specifications summarized in Table 4.3 were considered. Cycle 1 is the resin manufacturer recommended cycle for SI-ZG-5A, while cycle 2 is a composites manufacturer suggested cure cycle. The cure kinetics and viscosity model developed in this work for SI-ZG-5A and VR-56-4 were used in the simulations. A fiber volume fraction of 0.50 was chosen for the composite preform material. The panel was assumed to be fully saturated with resin at this fiber volume. Thermal properties for the resin and the fiber were taken for a typical epoxy and carbon fiber. The panel, the 3 mm thick steel tool and the distribution media were modeled with a one-dimensional column of elements in the thickness direction. The distribution

media was modeled as a nylon/resin composite with a fiber volume fraction of 0.23 and a thickness of 2 and 3 mm for the 5 mm and 25 mm panel, respectively. A convective heat transfer boundary condition of 20 $W/m^2°C$ was assumed on the top and bottom of the tool-part assembly. The heat transfer and resin cure kinetics were solved and resin flow during cure was neglected.

Table 4.3 summarizes the results of the simulations and Figures 4.12-4.15 present the maximum part temperature and minimum resin viscosity profiles predicted by the model.

Table 4.3: Results from the cure simulations.

Case	Exotherm Temperature (°C)	Minimum Vicosity (Pa·s)	Gel Time (min)	Flow Number (s/(Pa·s))
SAERTEX/SI-ZG-5A				
5 mm panel, Cycle 1*	4	0.031	191	128577
5 mm panel, Cycle 2**	4	0.034	212	130610
25 mm panel, Cycle 1	42	0.036	161	128831
25 mm panel, Cycle 2	42	0.037	182	130561
SAERTEX/VR-56-4				
5 mm panel, Cycle 1	7	0.033	290	280302
5 mm panel, Cycle 2	2	0.034	412	273814
25 mm panel, Cycle 1	25	0.034	280	281309
25 mm panel, Cycle 2	11	0.035	412	277117

* Cycle 1: Ramp to 66°C @ 1.11°C/min, Hold 2.75 hours, Ramp to 121°C @ 0.83°C/min, Hold 2.5 hours, Ramp to 177°C @ 0.56°C/min, Hold 6 hours, Ramp to RT @ -0.56°C/min.

** Cycle 2: Ramp to 66°C @ 0.56°C/min, Hold 4 hours, Ramp to 177°C @ 0.56°C/min, Hold 6 hours, Ramp to RT @ -0.56°C/min.

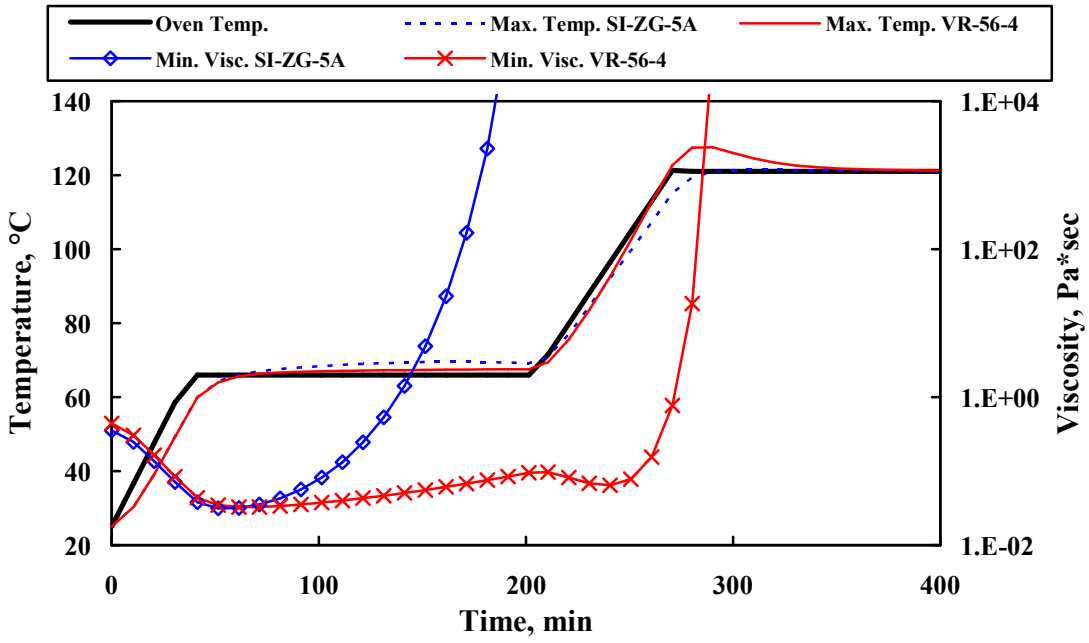

Figure 4.12: Predicted maximum part temperature and minimum resin viscosity for a 5mm thick panel cured following cycle 1 for SI-ZG-5A and VR-56-4.

It is clear that the two resin systems have significantly different curing behaviors. The gel time for each scan was detemined from the test data (not shown) when the storage modulus relation crosses the loss modulus relation. At this point the material is assumed to behave more like a glassy solid than a rubbery liquid. From this data, the material SI-ZG-5A has a faster gel time (an average of 162 min more guickly) than VR-56-4, but has a higher exothermic temperature for the 25 mm panel (up to +31°C). Both systems have similar minimum viscosity. VR-56-4 cure is more sensitive to the cure cycle selected in this study, as using cycle 2 reduces the exothermic temperature by 14°C and increases the gel time by 132 minutes. This difference between cycle 1 and 2 is not observed for SI-ZG-5A. VR-56-4 cure is more gradual and occurs at higher temperature and the results of the simulation clearly illustrate that behavior.

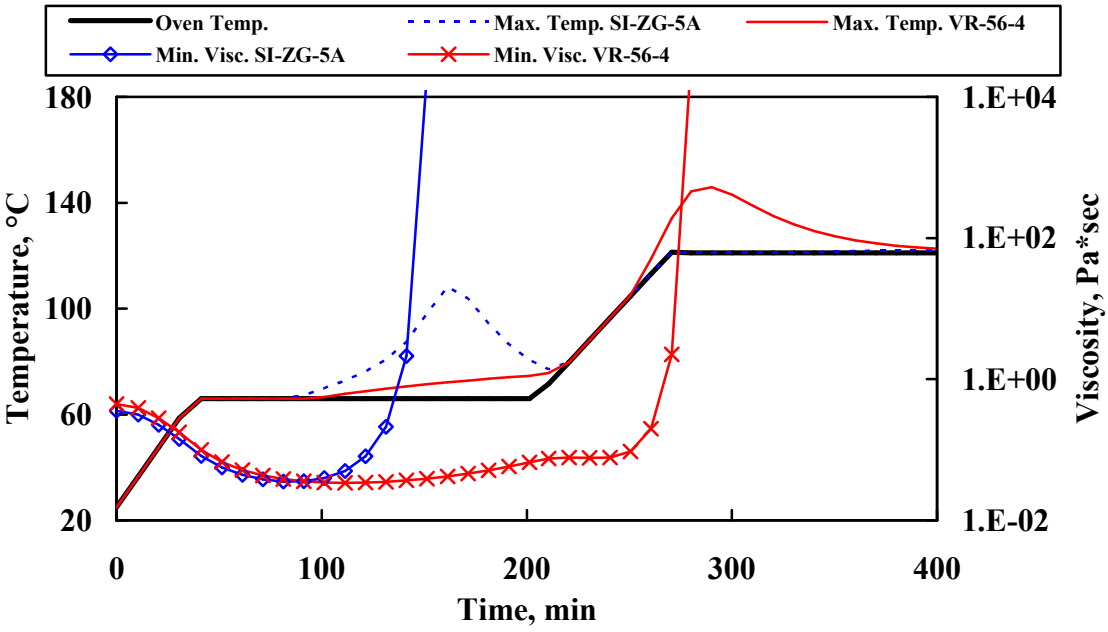

Figure 4.13: Predicted maximum part temperature and minimum resin viscosity for a 25mm thick panel cured following cycle 1 for SI-ZG-5A and VR56-4.

The flow number (FN) presented in Table 4.4 gives an indication on the amount of flow possible before gelation and was calculated using the following relation:

$$FN = \int_0^{t_{gel}} 1/\mu(t)dt \tag{4.5}$$

From Table 4.4, the flow number for VR56-4 is about twice the value for SI-ZG-5A, which indicates that there is more time for to resin flow before gelation occurs in VR-56-4. This analysis stresses the importance of understanding the curing behavior of the resin systems considered for a particular application and the relationship between part geometry and curing conditions.

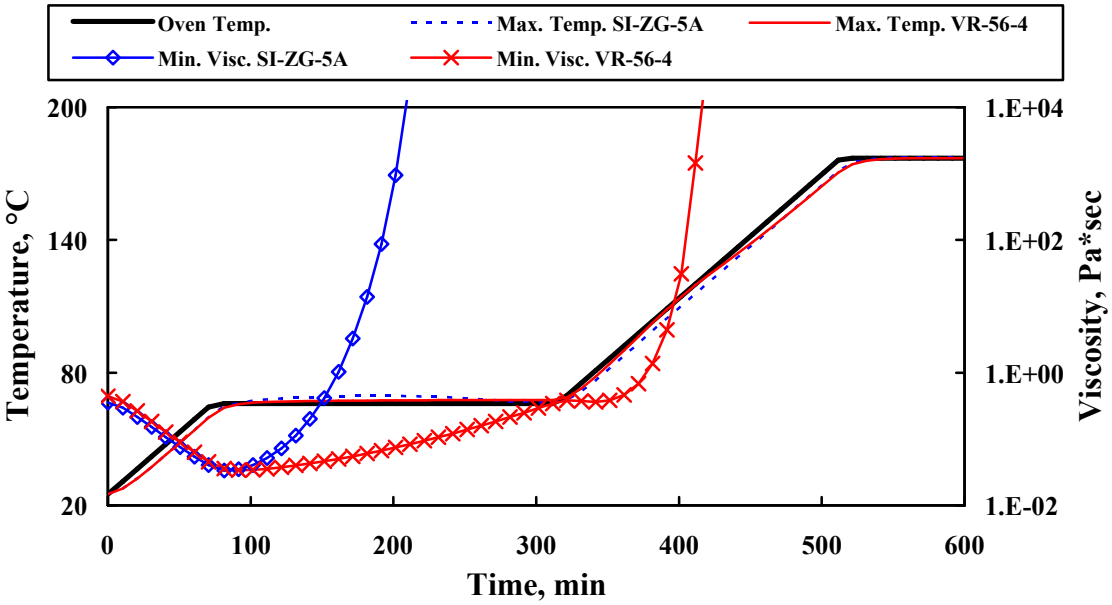

Figure 4.14: Predicted maximum part temperature and minimum resin viscosity for a 5mm thick panel cured following cycle 2 for SI-ZG-5A and VR56-4.

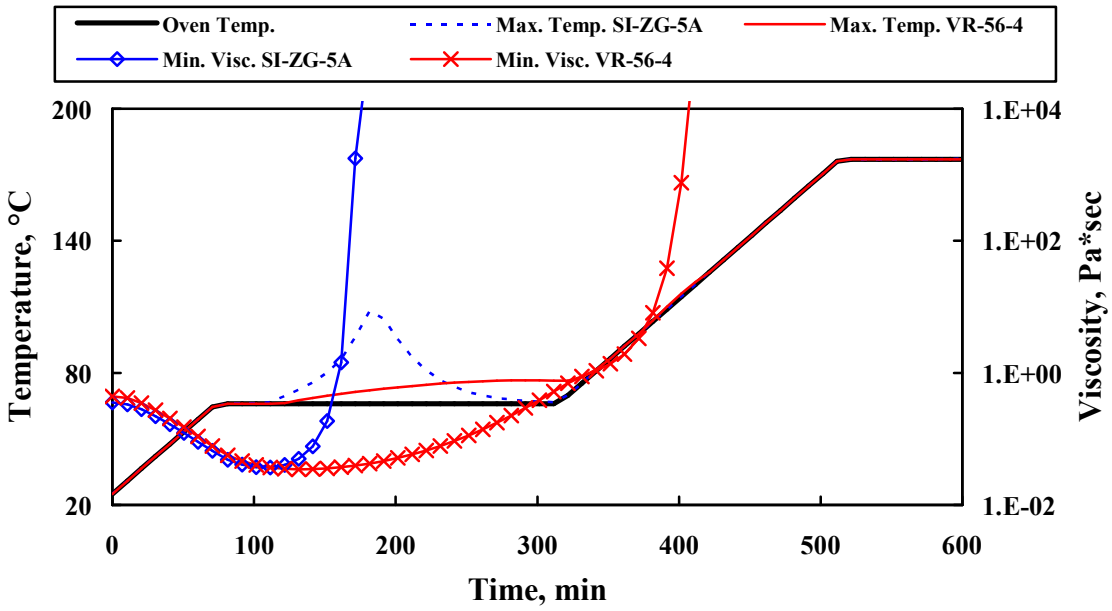

Figure 4.15: Predicted maximum part temperature and minimum resin viscosity for a 25mm thick panel cured following cycle 2 for SI-ZG-5A and VR56-4.

Chapter 5

VARTM Infiltration Experiments

In order to fully understand flow behavior during VARTM infiltration it is necessary to accurately characterize the flow and compaction response during actual infusion of composite parts. A detailed analysis of the VARTM infiltration process is presented in this chapter. An instrumented VARTM system was developed to measure resin pressure and panel transverse displacement at different locations in the preform during the infiltration process. The flow front position on the bag side and tool side of the preform was also measured in separate tests using a glass tool and digital video photography. Final composite quality was evaluated by analyzing the void contents and fiber volume fractions of multiple specimens of varying thickness. The preform deformation behavior during infiltration was measured and compared with the preform compaction curves measured in quasi-static compaction, which were described in detail in Chapter 2. The flow experiments were performed using the same carbon fabric preforms described in previous chapters. In an effort to determine thickness effects and the inter-stack, or region between stacks, influence on the flow behavior of the SAERTEX® multi-axial, warp-knit (MAWK) carbon fabric preforms, tests were perfomed to measure the infusion response of preform specimens containing one, two, four, and eight stacks of the material. Infiltration experiments were also conducted using ten layers of 5-harness satin, biaxial woven carbon fabric as the preform. Finally, the

relation between panel consolidation and resin pressure and the potential impact on the maximum achievable fiber volume fraction is discussed.

5.1 Background

Vacuum-assisted resin transfer molding (VARTM) is a variant of the resin transfer molding (RTM) composite manufacturing process [51]. In VARTM, the rigid top mold of the matched metal tooling found in RTM is replaced with a flexible vacuum bag. In addition, all flow and compaction occurs under atmospheric pressure alone. Having potential to eliminate the need for conventional autoclave processing of composites translates to tremendous cost savings for the manufacture of large, complex shapes such as aircraft wing structures [52]. The keys to successful fabrication of void-free composite laminates are adequate evacuation of the preform under leak-free conditions, adequate wet-out of the preform prior to gelation of the resin system, and, finally, proper cure of the part in which the resin reaches gelation under leak-free conditions.

Manufacture of composite parts by the VARTM method begins with lay-up, or draping, of a dry fiber preform onto the rigid metal tool. The rigid tool base dictates the final shape of the part. The preform, which serves as reinforcement in the final composite part, is typically a woven or knitted, glass or carbon fabric. Resin inlet and vacuum ports are stategically placed to ensure full infusion and wet-out of the preform in the given out-time of the resin matrix. Some manufacturers wisely use process simulation models to determine the number and location of these ports to limit the cost of trial and error of prototype parts [53]. The preform is then bagged using a flexible plastic film.

Adequate evacuation of the bagged fiber preform is one of the keys to successful VARTM fabrication of void free laminates. During this step the resin inlet line is closed and the dry preform is evacuated via the vacuum port by a vacuum pump to reach the maximum compaction level of 760 mm Hg which is equal to a compaction pressure of 101.5 kPa. The fiber volume fraction of the fabric preform increases as the fiber bundles, or tows, are flattened, reducing the pores and gaps both within the tows and between tows and also due to elastic deformation of the fibers, nesting and interlayer packing [54]. Obviously this level

can only be achieved with a vaccum bag that is completely sealed and free of any air leaks. However, the time required during this step to fully debulk the preform is not fully understood based on a review of the literature. Gama, et al. [55] found that the fiber volume of the dry preform could be maximized by cycling the vacuum pressure between 127 mm Hg (compaction pressure = 16.9 kPa) and 760 mm Hg (compaction pressure = 101.5 kPa) with two minute holds at each of the two vacuum levels. Gama et al. found that the fabric investigated exhibited a hysteresis response to compaction probably due to increased nesting with each successive compaction cycle. It was found that the preform reached a minimum thickness after approximately fifty cycles. In other work [56, 57], maximum dry fiber volumes were achieved by debulking the preform under full vacuum for long periods of time. For the purpose of the present work the practice of debulking the dry preform at a constant vacuum level of 760 mm Hg for a long period of time (up to 10 hours) was followed prior to infusion.

The SCRIMP [58, 59] version of VARTM includes a highly permeable layer of material typically called a "distribution media." The distribitution media allows parts with high aspect ratios to be manufactured in a relatively short period of time, i.e., composite skins on aircraft where the length and width of the part is many times greater than the thickness. The highly porous media provides a pathway to quickly distribute the resin across the surface area of the fiber preform. To fill the preform, resin flows through the thickness which is the smallest dimension. Resin flows, or leaks, down into the part from the media layer due to the pressure difference, gravity and capillary action [60].

After the debulking step, the dry preform is prepared for infusion. Typically the resin is degassed under full vacuum to remove air bubbles and then allowed to flow into the part via the resin inlet tubing. As pointed out in the preceeding chapters and also widely accepted in the literature, the resin system must be at a temperature where the viscosity is at or below 0.5 Pa·sec. This number may seem somewhat arbitrary because the size of the part, as well as the out-time of the resin (time at ideal flow viscosity after mixing), dictates the ideal level of viscosity for infusion. A small part could be infused at viscosity levels above 0.5 Pa·sec, however minimizing the resin viscosity will maximize the resin flow rate and reduce part fill

times. The low-viscosity, degassed resin is contained in a pot which is open to the atmosphere at 101.50 kPa. Flow into the media and preform contained under full vacuum begins with the opening of the resin injection port. Therefore, transfer of the resin during VARTM processing occurs due to the pressure gradient which exists due to the atmospheric pressure on the resin and the 0 atmosphere created in the bag due to the vacuum pump. Refering to figure 5.1, the pressure of the resin, P_R, as it enters the bagged part is assumed to be 101.5 kPa. The change in fiber stress, σ_F, during VARTM infusion is governed by the effective stress concept developed by Terzaghi [57]. Where σ_F is equal to the localized compaction pressure carried by the fibers, P_C:

$$P_{ATM} = P_C + P_R \tag{5.1}$$

The flow front develops in the preform where on the wetted side of the preform, the local preform pressure, P_C inside the bag is equal to the atmospheric pressure, P_{ATM}, minus P_R and therefore is $P_C < 101$kPa.

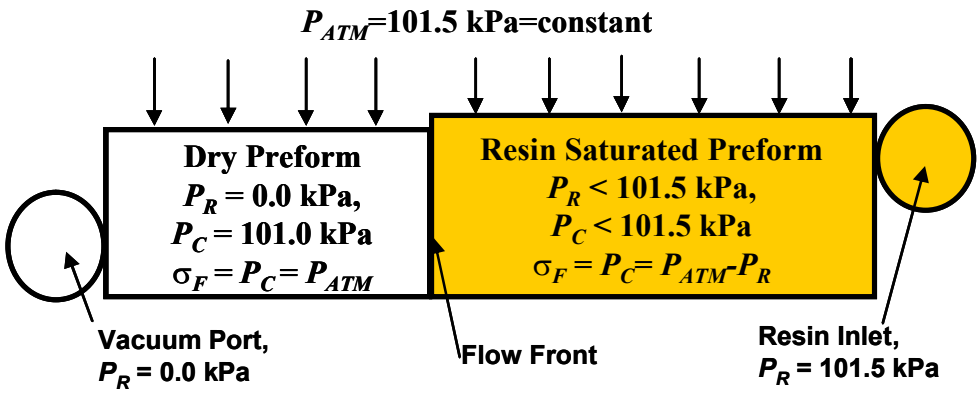

Figure 5.1: Theortical compaction behavior during VARTM infusion.

On the dry side, ahead of the flow front, the preform pressure inside the bag is also governed by (5.1). However, since there is no resin present on the dry side, the compaction pressure and fiber stress are equal to P_{ATM} because the dry side is presumably still at full vacuum. Therefore, the pressure distribution between the preform and the resin dynamically changes

as the flow front develops due to the force balance between the resin pressure of the wetted preform and compaction pressure of the atmosphere on the bag.

It has been found in previous work [21] that as the preform is initially wetted at the localized region of the flow front, the preform thickness initially decreases. This is the "lubrication effect," where the wetting of the fabric reduces friction, allowing the fibers to slide more easily and further nest to a higher packing level. However, this lubrication-induced nesting phenomenon is quickly followed by spring-back of the fibers due to the resin pressure and subsequent release of compaction pressure, as explained by Equation 5.1. The increasing thickness results in decreasing fiber volume and, therefore, increasing porosity of the preform. Since the permeability of the preform increases with increasing porosity, then, according to Darcy's Law, resistance to resin flow into the part decreases. This summarizes one of the main difficulties in formulating process models to accurately predict flow evolution in VARTM processing, i.e., the thickness of the preform changes as a result of the resin pressure and flexible bag.

In previous infusion experiments of preforms with thickness greater than 1.27 cm, the flow front was observed to have a parabolic shape, as shown in Figure 5.2 [21]. This indicates that the flow front develops as a result of both transverse flow from the distribution layer as well as in-plane flow along the preform length in the direction of flow. This would also indicate that, for finite periods of time, the pressure varies through the thickness due to filled and unfilled regions at the flow front.

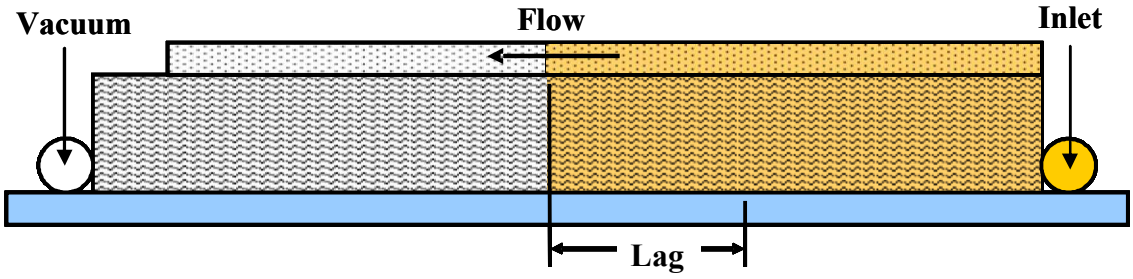

Figure 5.2: Side-view diagram of flow in VARTM of thick preform specimen.

As the flow front nears the end of the panel and the preform becomes fully saturated with resin, a pressure gradient develops along the length of the part from the resin port to the vacuum port. Because the top of the mold is made of a flexible material, this pressure gradient leads to a thickness gradient. The resin pressure in the part is higher at the resin inlet side, making the compaction pressure lower and, therefore, leads to a higher thickness and lower fiber volume fraction at the resin inlet side. After the preform reaches full saturation the thickness at the resin inlet is noticibly greater than the thickness of the preform near the end of the panel nearest to the vacuum port. This phenomenon can be expressed more simply using Darcy's Law and assuming a linear pressure gradient. The resin pressure, P_R, can be expressed as

$$P_R = P_{ATM}(1 - \frac{x}{L}) \tag{5.2}$$

At the time when the panel is completely wetted with resin, L is the length of the preform and x is the distance from the point of interest to the resin inlet. At any point along the length of the panel the compaction pressure can therefore be found by

$$P_C = P_{ATM} - P_R = P_{ATM}\left(\frac{x}{L}\right) \tag{5.3}$$

So at the resin inlet, $x = 0$ and the compaction presssure is equal to zero, meaning that the atmosperic pressure is carried by the resin. This would necessarily be the point of maximum thickness along the length of the panel. At the end of the panel nearest the vacuum port, $x=L$ and $P_C = P_{ATM}$. This is the point of minimum thickness or highest fiber volume fraction. In a series of experiments to improve the final part dimensional tolerances Gama, et al. [55] investigated the compaction response of the part after the preform became saturated. In these experiments the vaccum port was left open after the part was filled and the resin port closed. At the point of where saturation was reached and the resin port was closed, the thickness gradient from resin inlet to vacuum port was at a maximum. After 30 minutes with the vacuum port open so that resin could flow out of the part, the thickness gradient was non-existent. The vacuum was left open during cure of the part for approximately 600 minutes, which resulted in a marked change in thickness. However, the part was noted to be resin

starved after using this method. This work was conducted using layered glass fabric and the author does not remark on how the results would translate to fabrics of different architecture and porosity. It was noted that the procedure deserved further investigation in order to improve the dimensional stability and consistency of parts made by VARTM.

It has become common practice in the development of the VARTM process for aerospace quality parts to use a secondary bag, or "double bag", procedure for cure of the infused composite. After the part is fully wet-out with resin, both the resin inlet tubing as well as the vacuum line at some point is clamped and cut. Then the entire bagged part and clamped tubing is covered with breather cloth and a second flexible bag which is also sealed to the rigid tool. The second bag is evacuated using a second vacuum port and ensures that the original, inner bag will not leak during cure. Since the time for the resin to reach gelation can take several hours, any air leaks in the original bag bag that develop during oven cure would result in an uncompacted and high void content panel. Some have assumed that a second bag will somehow increase the amount of compaction pressure on the saturated preform and therefore lead to higher fiber volumes in the final cured part. This simply is not the case. The compaction pressure that the part realizes is always equal to the atmospheric pressure minus the resin pressure as stated in Equation 5.1. The atmospheric pressure is constant at P_{ATM} = 101.5 kPa. Using a second bag or ten extra vacuum bags does not change the value of P_{ATM}. The pressure of the resin sealed within the original bag does not change during cure. Therefore, once the inner bag is clamped, the compaction pressure will not change with the addition of a second bag. If, however, a leak in the inner bag develops during oven cure and resin is able to bleed from the part into the second bag, then an increase in fiber volume would develop. This is equivalent to the experiment Gama et al. [55] conducted leaving the vacuum port open during cure. However, simply relying on leaks to develop in the inner bag would result in significant variability in final quality from one part to the next. Work is ongoing at NASA Langley Research Center and by other research groups to investigate this and other techniques to improve the fiber volume of parts fabricated by VARTM.

In the following sections the pressure and compaction (thickness) response to resin infiltration of fiber preforms during actual VARTM infusion is presented. Experiments were conducted to deterimine the effect of part thickness as well as the effects of differing flow process scenarios in an effort to more fully understand flow during the process and verify the physical theories proposed in the preceeding paragraphs.

5.2 Experimental

5.2.1 Instrumented Tool Test Bed A 1.27 cm thick aluminum tool was instrumented to measure the pressure and displacement of the preform during the VARTM infiltration. The tool measured 120.0 cm x 60.0 cm to accommodate a 60.0 cm x 30.0 cm part as well as the necessary instrumentation. As shown in Figure 5.3, the pressure sensors (Omega Engineering, Inc., Series PX102) labeled P1 through P3 were embedded in the tool surface beneath the fiber preform. Fittings, supplied by Omega, allowed the sensors to form airtight seals with the tool. These sensors measure the level of vacuum inside the bag. When the bag is fully evacuated to 760 mm Hg, the preform compaction pressure is one atmosphere, or 101.5 kPa. During infusion, the hydrostatic resin pressure in the preform increases and the pressure sensors read a decrease in vacuum. The decrease in vacuum (or increase in resin pressure) inside the preform corresponds to a decrease in preform compaction pressure. For instance, when enough fluid has entered the bagged preform so that the fluid hydrostatic pressure is measured to be 40.5 kPa, or a vacuum level of 457 mm Hg, the corresponding pressure on the preform supplied by the atmosphere is equal to 61.0 kPa according to Equation 5.1. The term “release” is commonly used to describe the reduction in compaction pressure due to the infusion of the part with the pressurized resin. This will be more readily apparent in the results section of the chapter.

Linear Variable Displacement Transducers (LVDT, Omega Engineering, Inc., Series 400) labeled LVDT 1 through LVDT 3 were supported above the vacuum-bagged preform by a rigid aluminum beam. In addition, an L-Gage® laser thickness sensor was incorporated to supplement measurement of displacement by the LVDT sensors. One laser gage was placed

next to LVDT-2 to measure thickness at the middle of the panel. Sensors were recorded by a PC-based data acquisition system using LabVIEW® software. Both the LVDT and L-Gage data were acquired as changes in voltage. The voltage is converted to displacement using predeterimined calibration constants. The thickness is found from the starting thickness minus the thickness of the flexible bag, media and release cloth. The thickness is then converted to fiber volume fraction using Equation 2.2. All of the results are reported as fiber volume fraction. The flow front at the vacuum bag surface of the part was recorded using a digital video camera and later analysed with a P.C. based software.

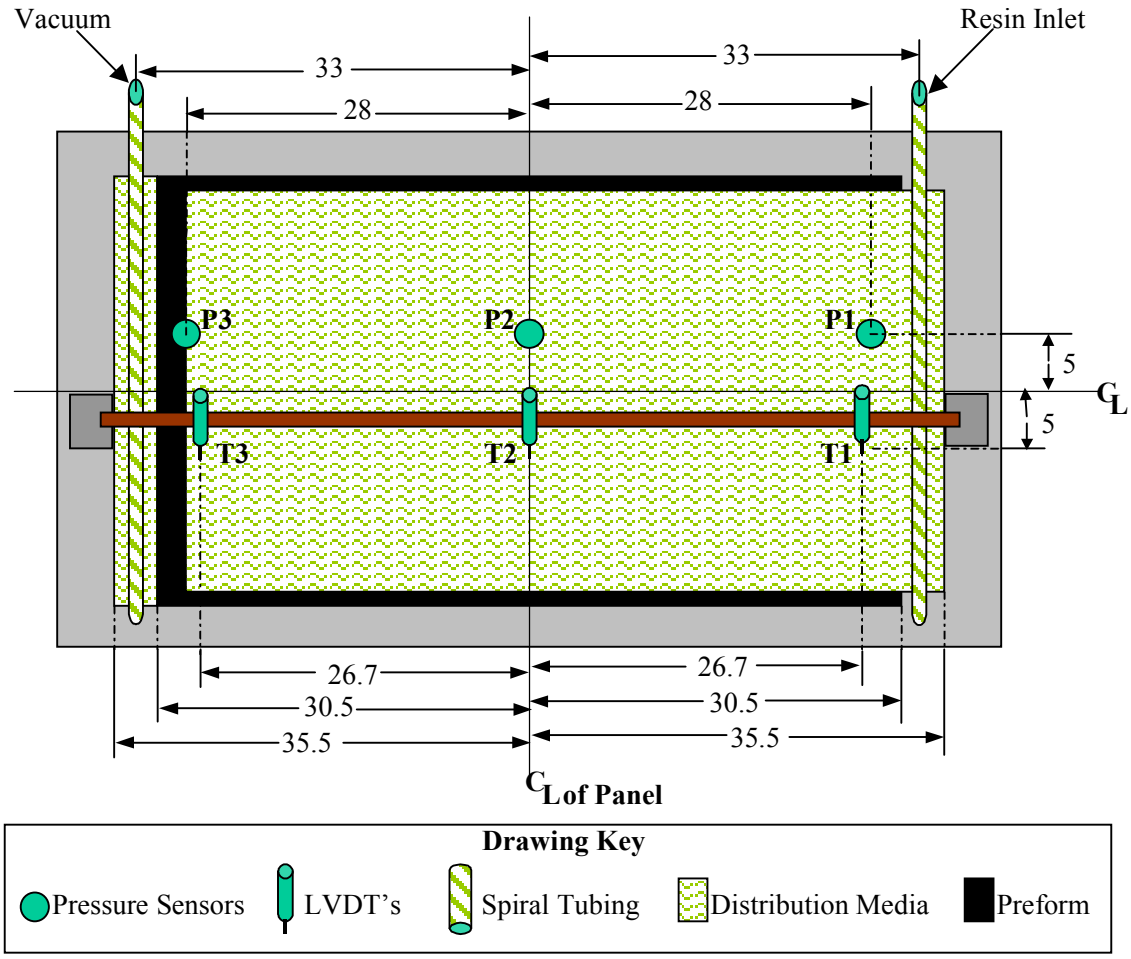

Figure 5.3: Typical VARTM lay-up scheme for the instrumented tool (dimensions in cm).

5.2.2 Glass Tool Test Bed A 1.27 cm thick glass tool plate was utilized to visually observe and record flow front evolution at the bottom (tool side) of the preform specimen. A picture of a glass tool infiltration is shown in Figure 5.4. Prior to each infusion test, a grid pattern wase drawn on the surface of the glass plate touching the carbon fabric. The lines were drawn at 5.08 cm intervals to facilitate position versus time analysis. A mirror was placed beneath the glass plate and angled so that one video camera could capture the flow fronts on both the top and the bottom simultaneously. This made analysis of the captured video much easier.

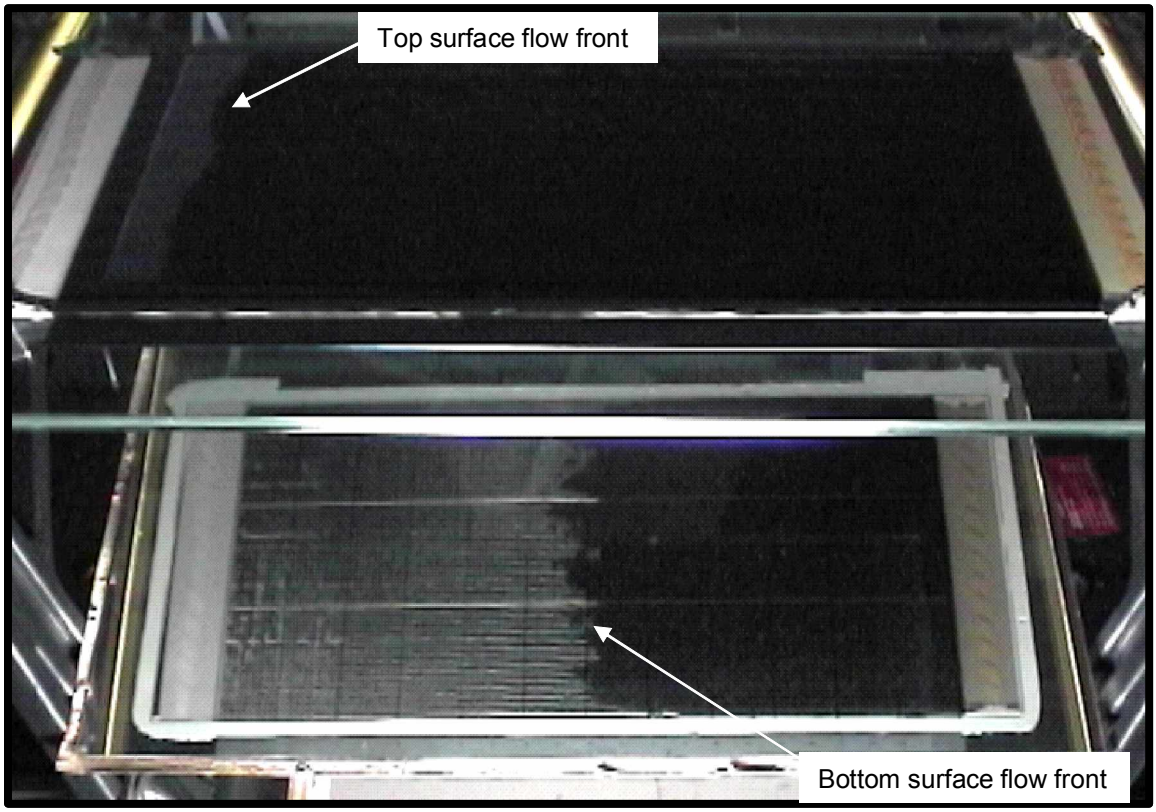

Figure 5.4: Glass tool infiltration experiment.

5.2.3 Experiment Procedure Preform specimens containing one, two, four, and eight stacks of the MAWK fabric and 10-layers of the 5-harness biaxial woven fabric were cut to dimensions of 60.96 cm x 30.48 cm. The specimens were laid onto the tooling so that flow

was parallel to the longer dimension. In the case of the MAWK fabric, the material was cut and placed on the tool so that the 0° rovings were length-wise, or parallel to the direction of resin flow (see Chapter 2). Refer again to Figure 5.3, which includes the typical VARTM lay-up scheme. A layer of the Release Ease® fabric was placed above the preform to serve as a release layer. The distribution medium, containing three layers of nylon mesh screen described in previous chapters, was laid on top of the preform and release layer. The medium was cut to dimensions of 60 cm by 27.4 cm allowing a 1.3 cm gap between the edge of the medium and the edge of the preform along the length. The distribution medium was terminated at a distance 2.5 cm from the end of the preform. These gaps prevented race-tracking of the resin as it flowed through the medium and the fiber preform. A 5.0 cm portion of the media was extended beyond the panel at the inlet side for inlet tube placement. M.M. Newman supplied Heli-Tube® spiral-wrap tubing (1.57 cm diameter) was stretched across the width of the panel on top of this section of medium to provide an even supply of resin to the part. Weatherhead® 0.635 cm inside-diameter polyethylene tubing was used to supply resin to the part. Both the polyethylene and spiral tubing were used on the vacuum side of the part. The outlet tubing was connected to a resin trap and vacuum pump. The bagging procedure was completed when the preform, medium and tubing were sealed to both the aluminum tool and the glass tool using a conformable vacuum bag and sealant tape.

The sealed bag and tubing were first evacuated to 12.7 mm Hg in order to zero the LVDT's and check for leaks using the pressure sensors. The vacuum pressure was then increased slowly to full vacuum and held there until the measured displacement reached equilibrium. The preform was then held under full vacuum for up to ten hours to debulk and achieve a minimum dry porosity of the material. The fluid used in the infusion experiments was the same SAE 40 motor oil used in both the compaction and permeability characterizations. The viscosity of the oil was determined using a Brookfield Model DV-III rheometer and the oil was then degassed prior to each experiment in a vacuum chamber for one hour.

After debulking, the free end of the inlet tube was placed in the pot containing the degassed resin. A tube clamp was opened to allow the fluid to flow into the spiral tubing, through the distribution medium and into the fiber preform, as shown in Figure 5.3. When the preform was fully impregnated, as confirmed through visual inspection, the fluid inlet tube was closed. The wetted preform was then held under vacuum for approximately fifteen minutes prior to clamping the vacuum tubing and ending the test.

5.2.4 Cured-Panel Fiber Volume Fraction Analysis In another set of experiments, one, two, four and eight-stack specimens of MAWK fabric as well as ten layer and twenty layer preform specimens of the biaxial fabric were infused with two different epoxy resin systems, SI-ZG-5A and VR56-4. These panels were layed-up and infused following the same procedure described above. The composite panels were then cured following an oven cycle which consisted of a ramp from room temperature to 65°C at 1.1°C/minute and held for 2.75 hours, followed by a ramp at 1.1°C/minute to 121°C and held for 2.75 hours. The part was then cooled at 1.1°C/minute to room temperature. Specimens, 1.27 cm by 0.75 cm, were cut from these cured panels at the center. The fiber volume fraction of these cured panels was then determined by acid digestion following the procedure described in ASTM D3171-99.

5.3 Results of Infiltration Experiments

In general, the results obtained using both the instrumented tool and the glass tool indicated that the test fluid flows rapidly into the media and then more slowly through the thickness of the carbon fiber preform. Side-view observation of the MAWK eight-stack infiltration as depicted in Figure 5.2 indicates that the majority of resin filling of the fiber preform is a result of transverse flow. The resin flow front was uniform across the width of the preform for all of the tests performed, as shown in Figure 5.4 and no race tracking at the edges was detected. Infiltration times to completely fill the preform increased with increasing thickness of the part.

5.3.1 Instrumented Tool Experiment Results The results of the instrumented tool infusion experiments performed using the MAWK material are shown in Figures 5.5-5.6 and 5.8-5.11. The displacement and pressure data for the ten-layer biaxial specimen are presented in Figure 5.12. As explained in Section 5.2.3, the preform material is typically bagged and evacuated under full vacuum (760 mm Hg), which results in a maximum debulking pressure supplied by the atmosphere to the preform of 101.5 kPa. The amount of time at which the preform is held during this debulking stage may affect both the properties of the preform as well as the processing parameters. Figures 5.5 through 5.7 include data obtained to determine the effects of the duration of the debulking stage on initial fiber volume fraction, preform compaction behavior during infusion and flow-front evolution times.

In Figure 5.5, both the response of the pressure sensors as well as the change in fiber volume fraction, V_f, for the infusion of a one stack MAWK preform specimen are displayed. This specimen is labeled MAWK1-1 and was compacted to 101.5 kPa under full vacuum and held at this level for one hour prior to infusion. After an hour of compaction the specimen was found to have an average fiber volume fraction of 0.563. The V_f of this specimen was not uniform after this compaction period. The V_f of the preform nearest to the vacuum port was higher than that found for the middle and material nearest the fluid inlet side, or furthest from the vacuum port. The plotted data begins at time, t = 0 min, when the fluid first enters the bagged preform. This is noted by an immediate response in the plot of LVDT 1: the thickness increases, corresponding to a decrease in fiber volume fraction. Pressure sensor P1 responds quickly thereafter to the increase in hydrstatic pressure of the fluid, indicating that the fluid has wetted the bottom of the preform (tool side). As the fluid continues to flow down the length of the media and proceed down into the preform, at t = 0.7 min LVDT 2 at the middle of the panel length indicates a change in thickness. In this case the V_f initially increases. This response is assumed to be the “lubrication effect” discussed in Chapter 2. The initial wetting of the fabric preform results in a decrease in the friction between fibers and fiber bundles. The reduction in friction allows the fibers to further nest and therefore reach a higher V_f. The value of V_f in this region of the panel increases from 0.55 at start to a

peak value of 0.56 at approximately t = 1.5 min. However, as the volume of fluid flowing into the preform continues, the increase in hydrostatic fluid pressure in this region increases. From equation 5.1, this results in a loss in fiber compaction pressure and, hence, relaxation of the fiber bed occurs as indicated by the decrease in V_f at t = 1.7 min. The response of LVDT 3 in Figure 5.5 differs from that of LVDT 2 in that there is no noticible increase in V_f due to lubrication by the infiltrating fluid. The region of preform measured by LVDT 3 was nearest to the vacuum port and had reached a higher initial V_f prior to infusion. It is assumed that because the material had reached a higher level of compaction during the one hour hold, that the material would not reach a higher V_f during wetting.

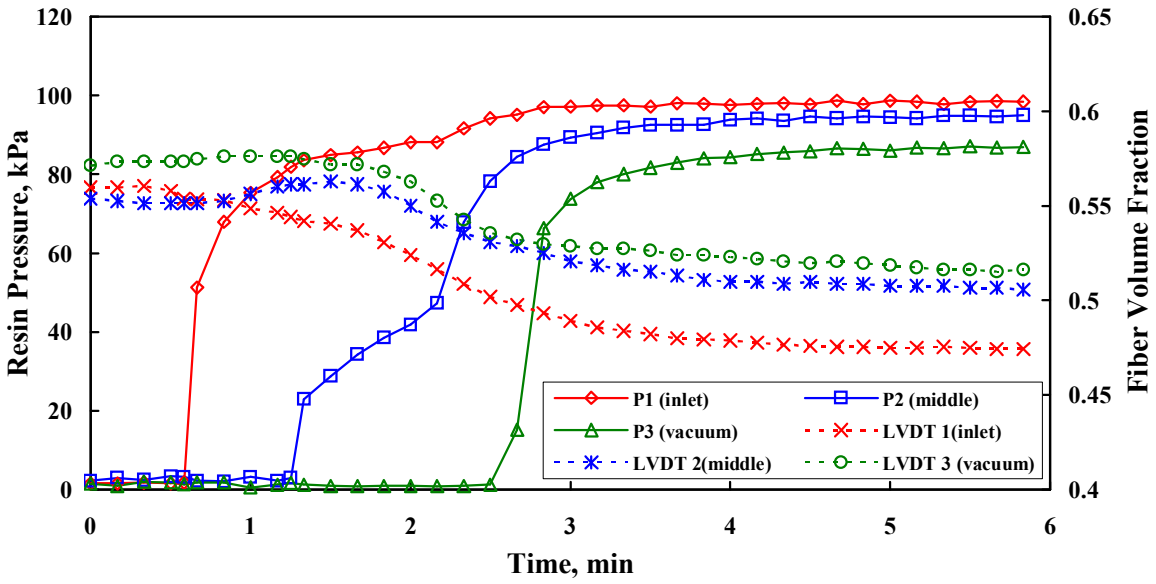

Figure 5.5: Instrumented tool infusion of one-stack of MAWK fabric after 1.0 hr compaction hold at full vacuum (MAWK1-1).

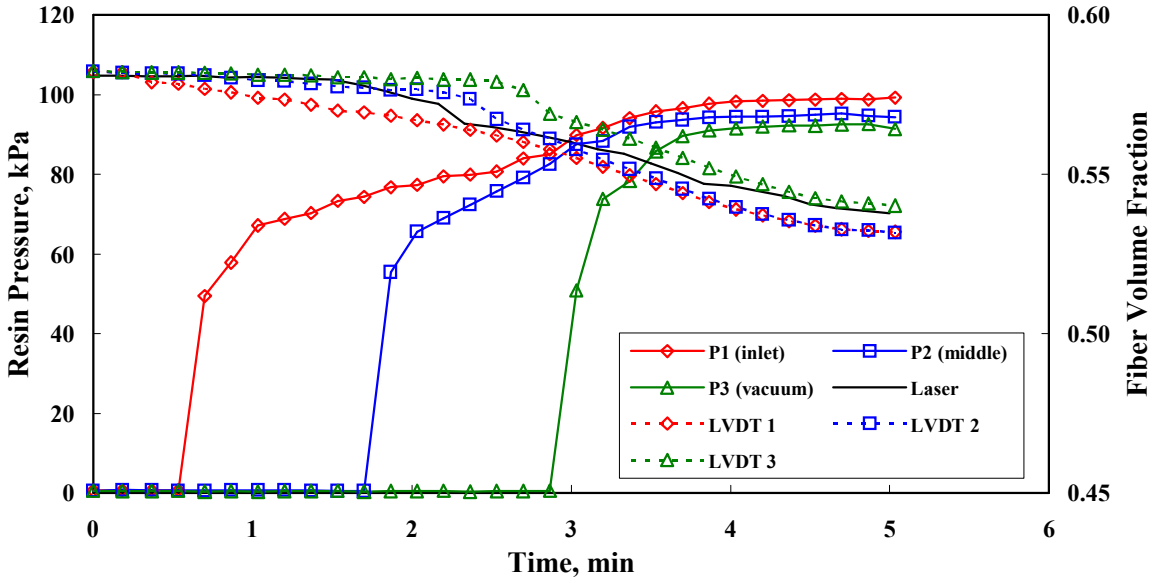

Figure 5.6: Instrumented tool infusion of one-stack of MAWK fabric after 10.0 hr compaction hold at full vacuum (MAWK 1-10).

In another experiment, a one stack MAWK specimen was infused after compacting and holding the specimen under full vacuum for ten hours. The results for this specimen, labeled MAWK1-10, are shown in Figure 5.6. This specimen reached a higher initial average V_f of 0.58 compared with the average found for the panel compacted for only an hour. The initial thickness of MAWK1-10 was also found to be much more uniform after the longer compaction hold. In addition, the initial V_f after the 10.0 hour debulking hold was closer if not slightly greater than the value presented in Chapter 2 for the quasi-static dry compaction experiments performed on the one-stack MAWK specimens. The L-Gage laser sensor was incorporated in this test and placed in close proximity to LVDT 2 to supplement the data response found with the LVDT. As shown in Figure 5.6, the L-Gage and LVDT 1, 2, and 3 all show a decrease in V_f, indicating relaxation in response to the increase in hydrostatic pressure carried by the wetting fluid. There were no lubricating effects found in the infusion of MAWK1-10. This supports the previous assertion that the material has reached a level of

V_f due to the longer period of debulking compaction which is high enough to reduce or eliminate the effects of lubrication. There is also a significant difference in the level of V_f noted for the time when the preform specimen has reached full saturation. LVDT 2 (middle) for the MAWK 1-1 specimen had a V_f of 0.506 while the MAWK1-10 specimen had a V_F of 0.530 at the time of saturation. In comparing the initial V_f found in the experiments for the one stack MAWK specimens, the time-dependence of the compaction response is clearly evident. In addition, the relaxation response of the MAWK preform during infusion, especially the saturation V_f, is influenced by the duration of the debulking time period. Although the data were not acquired during the ten hour debulking cycle for the MAWK1-10 specimen, in a separate experiment an eight stack MAWK specimen was debulked for 6.5 hours. The results of this experiment are shown below in Figure 5.7. It is clear from the slope of the curve in Figure 5.7 that the eight stacks continue to compact to higher V_f even up to 6.5 hours under 760 mm Hg, or 101.5 kPa, compaction pressure. This indicates that the MAWK material requires significant time to fully nest and reach a maximum V_f under the low compaction pressures experienced in the VARTM process.

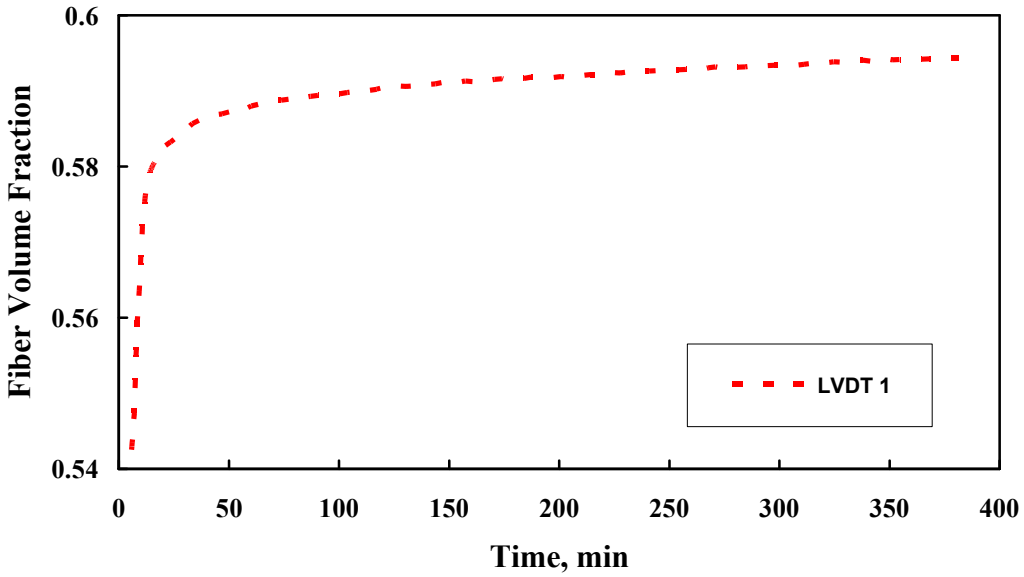

Figure 5.7: Compaction response to long debulking cycle of an eight stack MAWK preform specimen.

The viscosity of the fluid used to infiltrate MAWK1-1 was 0.270 Pa·s, while the fluid viscosity of the MAWK1-10 was 0.263 Pa·s. Despite having a slightly lower viscosity, in comparing the response times of both the LVDT's and the pressure sensors, it was found that increasing the debulking stage resulted in longer infiltration times for the MAWK1-10 specimen. For example, pressure sensor P3 for the MAWK1-1 specimen responded to the wetting resin at t = 2.5 min whereas P3 of the MAWK 1-10 specimen experiment responded at t = 2.86 min. These results support Darcy's Law for flow through porous media. The MAWK1-10 preform specimen has a lower porosity at the time of infusion in comparison to the MAWK1-1 specimen. From Darcy's Law, Equation 3.5 and 3.6, the permeability of the preform is proportional to the porosity. Therefore, as the porosity decreases due to the longer debulking stage, the permeability will necessarily decrease, making it more difficult for resin to flow through the preform. The increased time noted for the P3 reaction in the MAWK1-10 specimen indicates that the permeability of this preform is lower due to the lower level of porosity. In both experiments, all of the pressure sensor reaction times lag behind the LVDT and L-gage reactions, indicating that there is a lag in the flow front between the top (bag side) and bottom (tool side) of the preform. This is due to the difference in permeability between the distribution media which rests on the top surface of the preform and the through thickness permeability of the preform.

In another series of instrumented-tool infusion experiments, one, two, four and eight stack MAWK preform specimens were infused to determine the effect of thickness variation on VARTM process behavior. In addition, a 10-layer biaxial specimen was also infused for the purpose of comparing differing fabric architectures. All of these tests were performed on specimens that had experienced a 10-hour debulking stage prior to infusion. In addition, after the preform was visually observed to be fully wetted, and all of the pressure sensors had reacted, the fluid inlet was clamped and the specimen was held under full vacuum for at least 0.25 hours. The results of these tests are shown in the following Figures 5.8-5.12.

After initial compaction to 101.5 kPa under full vacuum, each specimen was found to further compact after being held for up to ten hours during the debulking stage and prior to

infusion. For the MAWK specimens, the average increase in fiber volume during the debulking stage was 0.06 %, whereas for the ten layer biaxial specimen, an increase of almost 0.15 % was noted. Both displacement and pressure values at important events during infusion are shown in Table 5.1.

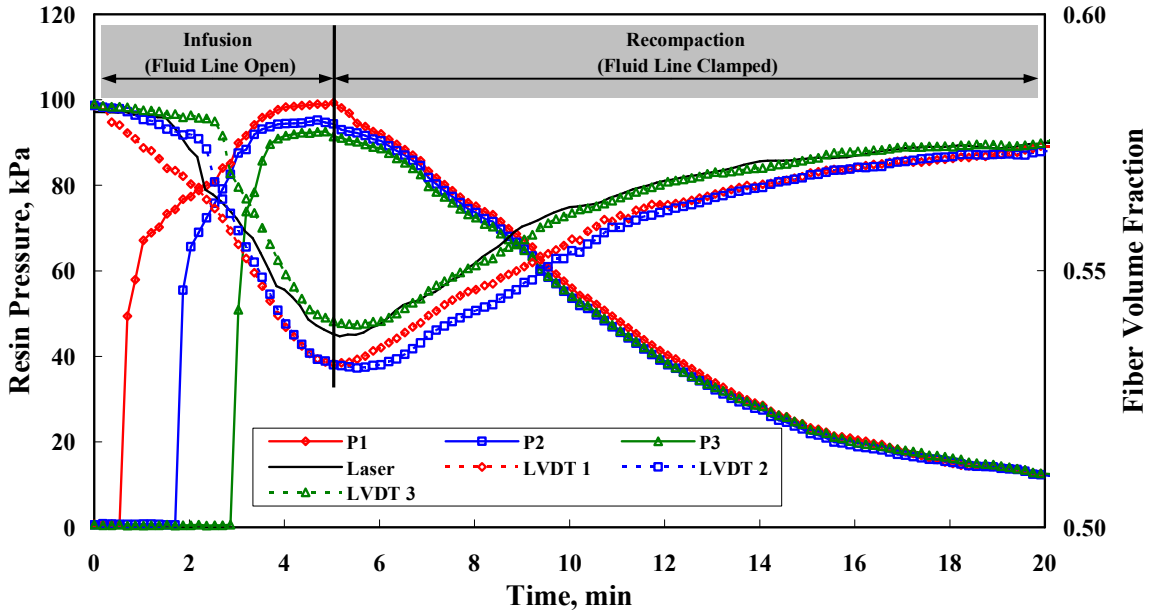

Figure 5.8: Instrumented tool infusion of one stack of MAWK fabric.

As the fluid flowed into the preform, the following general observations of the pressure and displacement data resulting from all of the MAWK test specimens were evident:

1) The displacement sensors (LVDT 1, 2 and 3) reacted prior to the pressure sensors (P1, P2, and P3) during infusion. This is noted by the decrease in fiber volume plotted for each of the displacement sensors as the flow front moves down the length (60.0 cm) of the specimen. The delay is due to the time required for the fluid to flow in the transverse direction and reach the pressure sensors. The rapid reaction of the displacement sensors to the relaxation of the preform as the fluid is observed to flow

past the measurement points beneath the LVDTs combined with the slightly delayed reaction of the pressure sensors, indicates that flow occurs rapidly in the media and then more slowly through the preform.

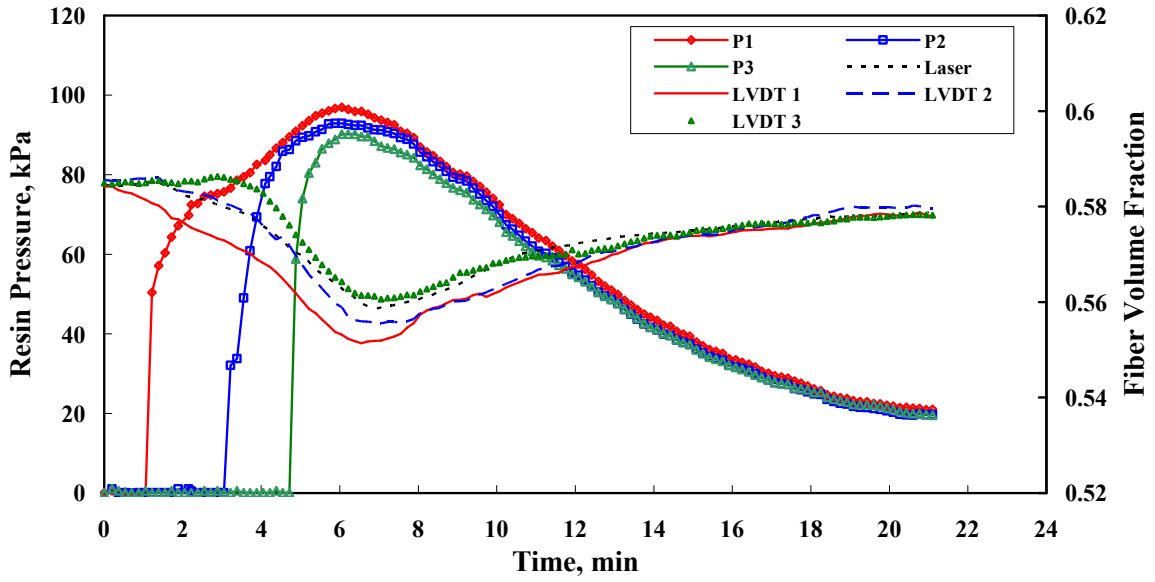

Figure 5.9: Instrumented tool infusion of two stacks of MAWK fabric.

2) When the fluid reaches the bottom of the preform at the tool surface, the vacuum level at the pressure sensor rapidly decreases due to the increase in hydrostatic fluid pressure. This corresponds to preform relaxation in that region. The fluid hydrostatic pressure continues to increase in that region until preform saturation occurs at or near a fluid pressure of 101.5 kPa and corresponding compaction pressure near 0 kPa.

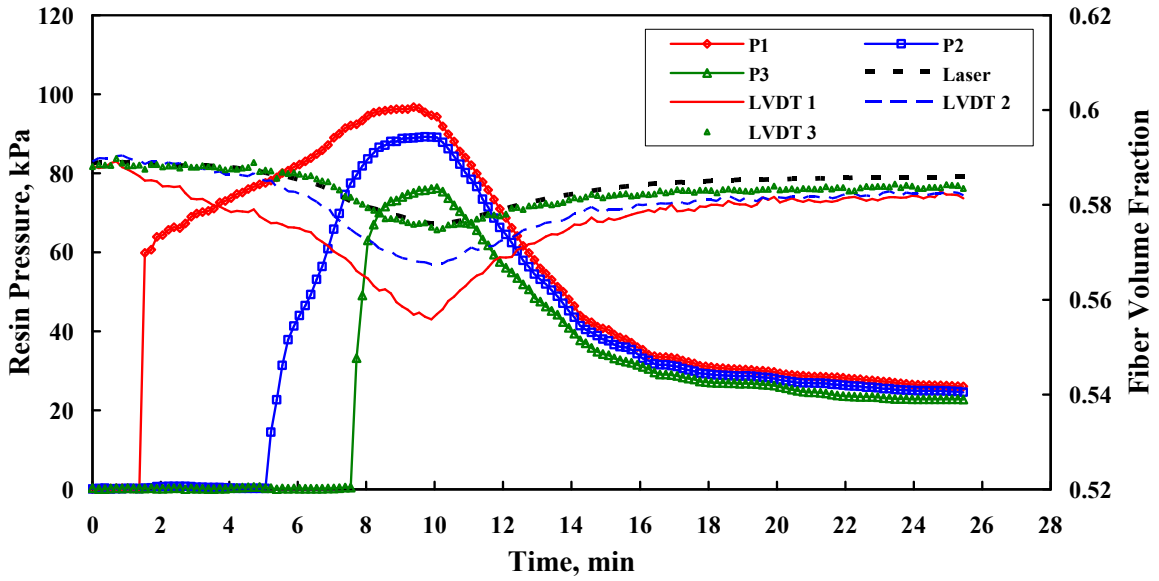

Figure 5.10: Instrumented tool infusion of four stacks of MAWK fabric.

3) Prior to recompaction, after the preform was observed to be filled or fully wetted, a pressure gradient existed in the flow direction, i.e., P1>P2>P3. Because the fluid pressure was found to be greater at the fluid inlet side than at the vacuum side, this should correspond to a greater volume of fluid in the P1 region than in the P2 region and, therefore, the measured fiber volume should decrease from the vacuum side to the fluid inlet side. This was found to be the case, as indicated by the displacement sensors, in Figures 5.9, 5.10 and 5.11. During infusion, at the point where all three pressure sensors are at or near the maximum, the V_f at LVDT1 < LVDT2 < LVDT3. This corresponds to P1>P2>P3 during this same time frame.

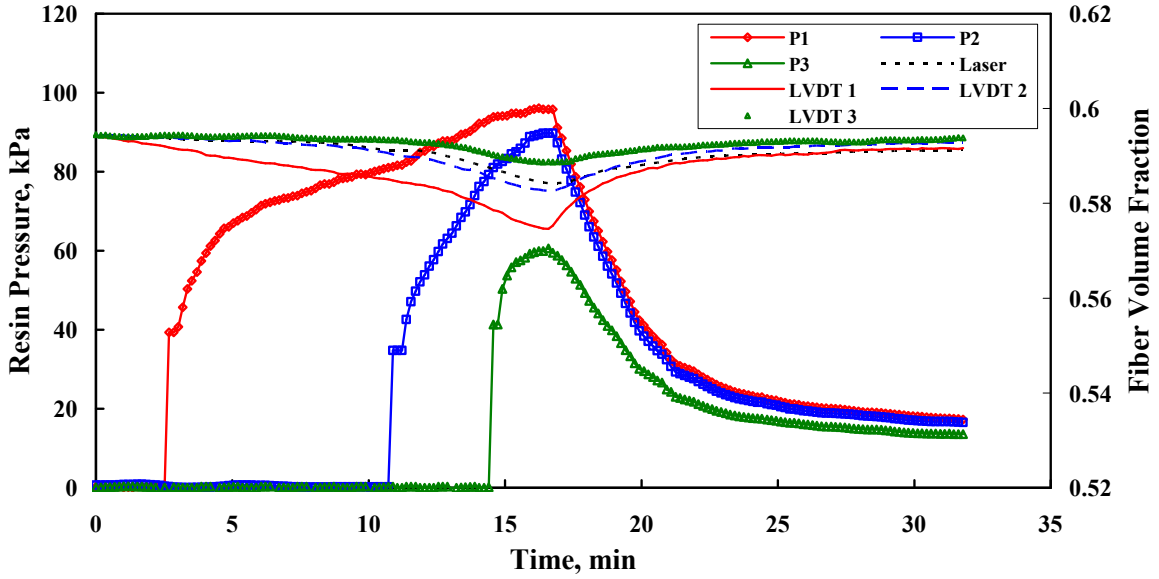

Figure 5.11: Instrumented tool infusion of eight stacks of MAWK fabric.

4) For all of the MAWK preform specimens, the average fiber volume fraction was greater prior to infusion than at the end of the infiltration test. However, in comparing the results from the MAWK specimens (Figures 5.8-5.11), the change in fiber volume appears to be more drastic for the one- and two-stack specimens than was found in the four- and eight-stack tests. In fact, the decrease in fiber volume during infusion is inversely proportional to the amount of stacks in the specimen.

This inversely proportional relationship may be due to the force exerted by the mass of the wetted upper stacks on the lower stacks in the thicker parts, which may restrict release of the preform as the resin pressure increases. Assuming a constant V_f of 0.57, a fiber density of 1.77 g/cc and a fluid (resin) density of 1.25 g/cc and using the rule of mixtures, the force exerted by one wetted 60 cm x 30 cm stack is approximately 3.92 N. For the eight stacks, this translates to an added compaction pressure of only 0.153 kPa, which is a fraction of the pressure exerted by the atmosphere even at high levels of hydrostactic resin pressure during

infusion. A more likely reason for this behavior is more apparent from the data summary presented in Table 5.1. The compaction pressure values included in the table were calculated from the resin pressure data recorded during the experiment and using Equation 5.1.

Table 5.1: Sensor data recorded during instrumented-tool infusion at two general events.

Event	Specimen	Time, min	Compaction Pressure, kPa			Fiber Volume,V_f		
			P1	P2	P3	LVDT1	LVDT2	LVDT3
LVDT 2 Reacts	One Stack	0.97	41.2	101.5	101.5	0.576	0.580	0.582
	Two Stack	1.55	41.3	101.5	101.5	0.579	0.585	0.585
	Four Stack	2.75	43.3	101.5	101.5	0.581	0.587	0.585
	Eight Stack	7.05	48.9	101.5	101.5	0.588	0.593	0.594
	Biaxial	3.63	22.6	101.5	101.5	0.512	0.540	0.542
LVDT 3 Reacts	One Stack	2.53	20.3	25.3	101.5	0.562	0.567	0.579
	Two Stack	3.51	20.1	32.6	101.5	0.571	0.579	0.585
	Four Stack	6.38	19.9	53.0	101.5	0.574	0.581	0.586
	Eight Stack	11.21	20.5	67.4	101.5	0.584	0.590	0.593
	Biaxial	4.70	16.5	47.7	101.5	0.500	0.531	0.541

There is an observable trend associated with the effect of increased thickness, or number of stacks, and the relationship between LVDT reaction and corresponding compaction pressure values. For the LVDT 1 reaction event, the value of P1 increases as the amount of stacks in the specimen increases. Likewise, for the LVDT 2 reaction the same trend is observed. This is most likely due to the increase in the flow front lag between the top and bottom of the preform (Figure 5.3). The lag is due to the high permeability of the fluid distribution layers on the top surface of the preform. The lag increases with increasing specimen thickness because of the increased volume of resin needed to flow through the thickness and fill the greater volume of pores in the preform. Any regions, of dry preform is considered to still be under full vacuum and therefore fully compacted. Therefore, as the lag becomes greater due

to the greater thickness, a larger region of dry compacted preform exists when the top flow front reaches the end of the media. The flow front lag will be more apparent in the glass tool results section below. When the top flow front reaches the end of the media, the flow front velocity decreases dramaticlly due to the lower permeability of the preform, as noted in Chapter 3. Because a pressure difference still exists between the fluid pot, or reservoir, and the vacuum port, fluid continues to flow into the preform as noted by the continued rise in resin pressure at P1. In the thinner specimens where the lag is smaller, the bottom flow front quickly matches the top just seconds after the end of the media is reached. From that point forward, flow evolves almost entirely in-plane as the flow front moves slowly towards the end of the preform. In each of these experiments the media always ended 2.54 cm prior to the end of the preform specimen. The reason for the gap is to allow the bottom flow front to match the top prior to full saturation of the preform. Since more fluid continues to flow into the preform from the fluid reservoir, the already wetted regions of preform become more saturated with fluid. The hydrostaic pressure carried by the fluid results in further release of compaction pressure on the fiber bed and the V_f decreases. Because of the greater lag in the thicker panels, when the top flow front reaches the end of the media, there is a greater amount of fully compacted dry preform still to be wetted. The top flow front continues to flow in-plane towards the end of the specimen while the remaining dry preform is filling. The flow fronts eventually catch-up to each other prior to the panel becoming completely wet-out. However, the key difference is that the thicker specimens have a greater portion of preform that has remained fully compacted for a longer period of time prior to reaching full wet-out. Although a test has not been conducted, it is assumed that if the resin inlet were not clamped immediately after the four and eight stack specimens reached full wet-out, the further flow of resin and increase in resin pressure would cause further relaxation of the specimen and loss of V_f. With this in mind, it may also be possible to reduce the amount of relaxation in the thinner panels by reducing the gap between the end of the media and the end of the preform. This would imply that the final fiber volume fraction could be tailored by adjusting the gap length of the media. A phenomenon of this type should be further investigated using finite element process simulation models.

For the 10-layer biaxial specimen, which was also debulked for ten hours prior to infusion there was also no evidence of a lubricating effect on the V_f. The displacement and pressure sensors were found to react in much the same way as in the MAWK specimen tests during the infusion part of the experiment. However, the recompaction of this material was quite different. As shown in Figure 5.12, this preform material requires much more time to reach a steady pressure and displacement. In fact in the test performed neither the pressure nor the displacement ever reached a steady state. After clamping the fluid inlet tubing and pulling vacuum for 15 minutes following the procedure used for the MAWK specimens, the pressure sensors in the biaxial infusion reported only a 15 kPa recovery of compaction pressure. The MAWK specimens averaged a 75 kPa recovery of compaction pressure in this same time period.

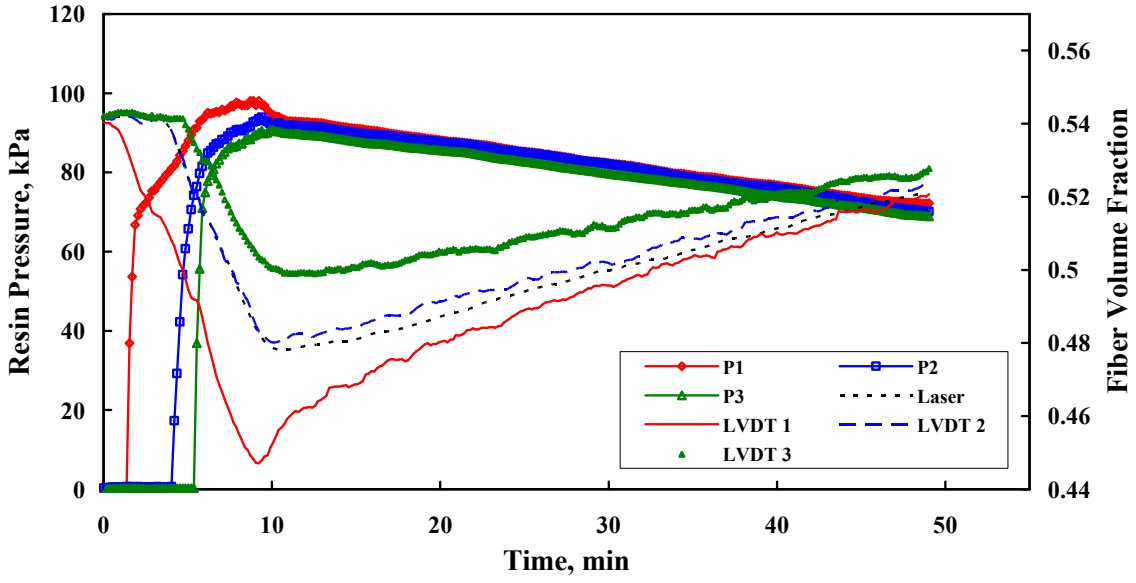

Figure 5.12: Instrumented tool infusion of 10 layers of biaxial fabric.

Figure 5.13 shows the displacement vs the sensor position along the length of the panel for two different times during the infusion of the two and four stack MAWK specimens. These

times include the point where the panel has become fully wetted as well as the point in time where the panels have undergone a fifteen minute recompaction. Figure 5.14 shows the same type of results for the biaxial panel infusion experiment. This plot includes a third time where the preform reaches the end of the forty minute recompaction (time = 50 min). The fiber volumes in these two figures are plotted on different scales due to the higher fiber volume of the MAWK material, however, for the purpose of comparison, the range of the scale is the same in both figures.

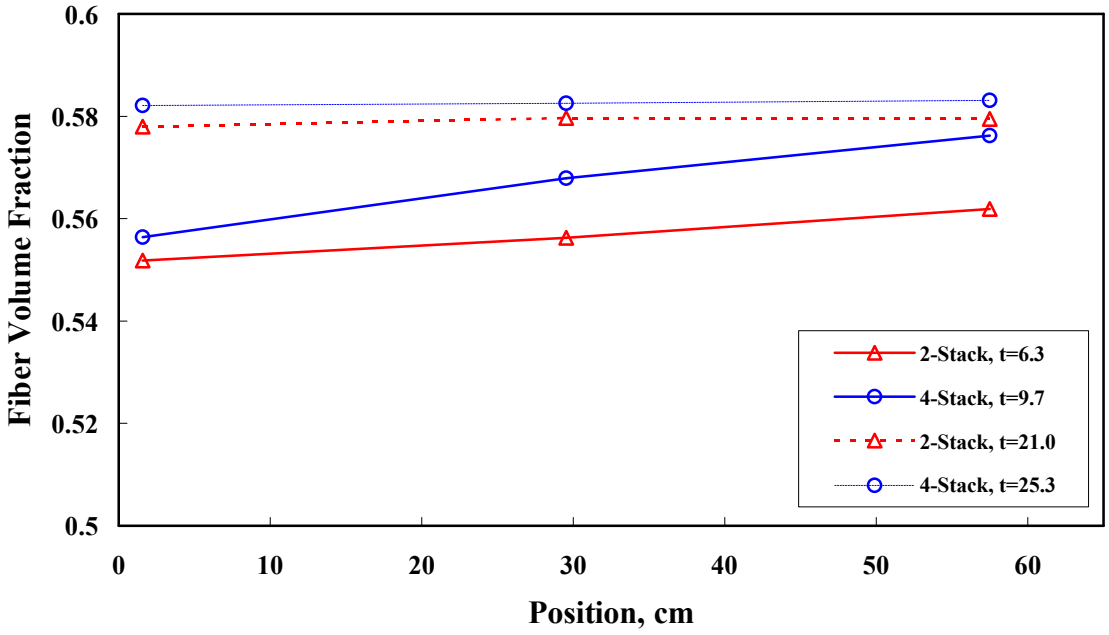

Figure 5.13: Thickness gradient of MAWK 2 and 4 stack specimens. (t is time in minutes)

In Figure 5.13, it is observed that both MAWK specimens exhibit a thickness gradient across the length of the preform at the point in time where the panel has reached full wet-out as shown by the difference in fiber volume from the resin port (position = 2 cm) and at the vacuum port (position = 59 cm). As explained previously, the resin pressure in the panel is higher near the resin inlet due to a higher volume of resin in this region. However, within fifteen minutes after clamping the resin inlet and recompaction of the infused preform under

full vacuum, the thickness gradient in both the two and four stack MAWK specimens has been nearly eliminated. This occurs in the two stack specimen without having reached a steady state of fiber volume, as was indicated in the infiltration data of Figure 5.9.

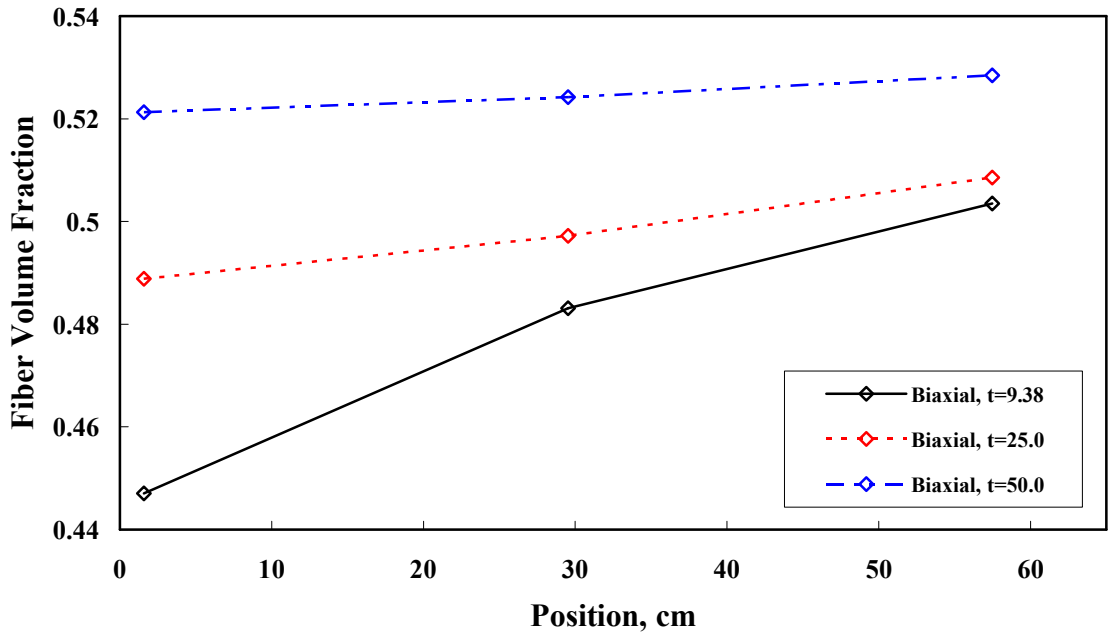

Figure 5.14: Thickness gradient of 10 layer biaxial specimen. (t is time in minutes)

In Figure 5.14, the biaxial specimen also exhibited a gradient in thickness immediately after the preform was observed to be fully wet-out (at test time, t = 9.38 min). Fifteen minutes after clamping the resin inlet, the fiber volume fraction at the inlet side was approximately 2.0 % lower than was measured in the preform near the vacuum port end of the panel. After forty minutes (at t = 50 min) under full vaccum, the tolerance improved to a gradient of 0.7%. There was also a marked increase in fiber volume fraction during the recompaction of the MAWK panels and especially the biaxial specimen. These results demonstrate that the fiber volume gradient that exists after VARTM infusion can be reduced or eliminated by closing the resin supply inlet and continuing to evacuate the part for a period of time. The preform architecture does affect the amount of time required to reduce the thickness

gradient. While it is not strictly correct to compare the two and four stack MAWK specimens to the biaxial specimen: the thickness of the biaxial is approximately equal to three stacks of MAWK material. The porosity of the woven biaxial material is greater than that of the MAWK fabric due to the difference in architecture. Hence, a higher volume of resin must flow into the biaxial material to fully wet-out the preform. Although the permeability is higher as well, the time required to remove the larger volume of resin results in greater times to reduce the thickness gradient in the biaxial fabric.

5.3.2 Glass Tool Infusion Results Figures 5.15 through 5.19 contain the flow front evolution data obtained using the glass tool (GT) for the one, two, four and eight stack MAWK preforms, as well as, the 10 layer biaxial specimen. The GT allowed visual detemination of the flow front on both the bag side as well as the tool side of the infused preform. The results of these tests are compared with the flow front data obtained in the instrumented tool (IT) tests discussed in the previous section. Because the metallic IT is not transparent, it is impossible to visually observe the tool-side flow. Therefore; the times at which the pressure sensor and LVDT react are plotted in these figures for comparison.

In Figures 5.15 through 5.19 it can be seen that in each case the flow front observed in the GT experiments moves more rapidly on the top surface (bag-side) up to the point where the distribution media stops at 2.54 cm from the end of the panel. At this point the fill rate on the bag-side decreases dramatically. In a comparison of all of the preform specimen test results, the lag increased with increasing thickness of the preform specimen, as expected. A transition in the slope of the bottom (tool-side) flow front curve was observed for the two, four and eight stack MAWK panels as well as the biaxial panel test. The slope of the flow rate for the tool-side flow front increases at approximately the time that the bag-side flow reaches the end of the media. This behavior supports the earlier stated assumption that, as the flow front on the bag side reaches the end of the media, the volume of resin flowing into the part does not change despite the decrease in observed resin flowing on the bag-side. In the case of the thicker panels, when the fluid reaches the end of the media, the fluid flows

down into the part to fill the dry, evacuated regions of preform. In the thin, one stack MAWK panel (Figure 5.15), no transition was observed because there is a smaller lag between the bag-side and tool-side flow fronts. The volumetric rate of flow of resin in this panel also remains the same after the media is saturated. However, since the unfilled region of preform in this panel is so much smaller after media saturation, the volume of resin flowing into the panel near the resin inlet is greater than is needed to fill the entire preform. The excess fluid allows further relaxation of the preform and "balloons" the vacuum bag. This excessive volume of fluid cannot be as easily removed from the panel after clamping the resin port, hence the results shown in Figure 5.8.

All of the results of the GT experiments to determine flow-front evolution on both the bag-side and tool-side are include for comparison in Figures 5.20 and 5.21, respectively. As expected, the increase in specimen thickness results in an increase in fill times. The shape of the curves is fairly consistent when comparing the different MAWK specimens as well as the biaxial material.

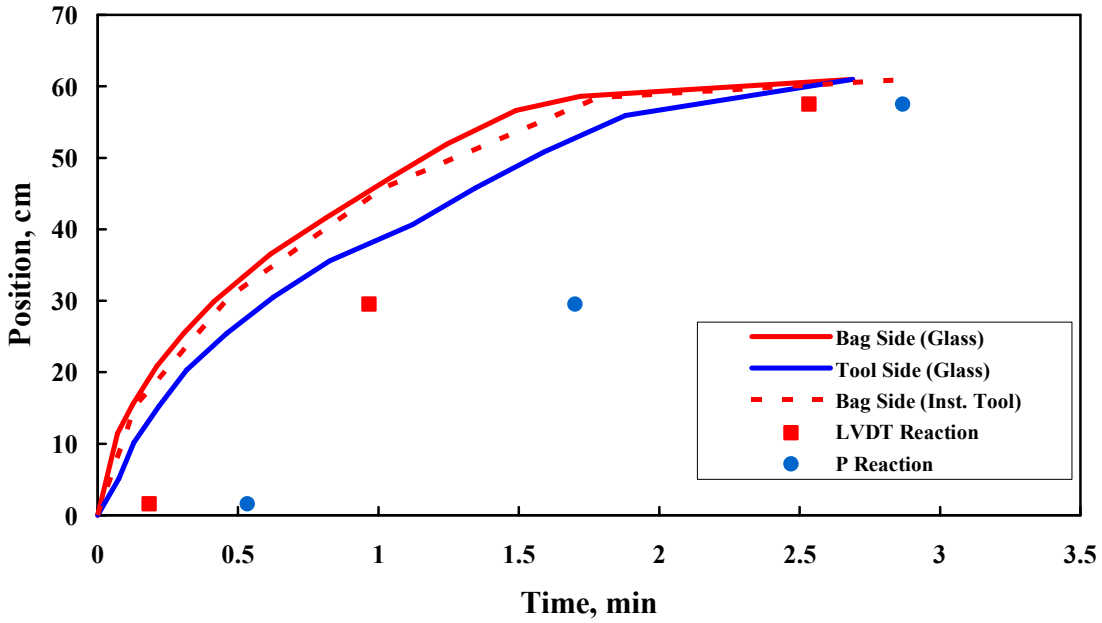

Figure 5.15: Flow front evolution in one stack MAWK panel.

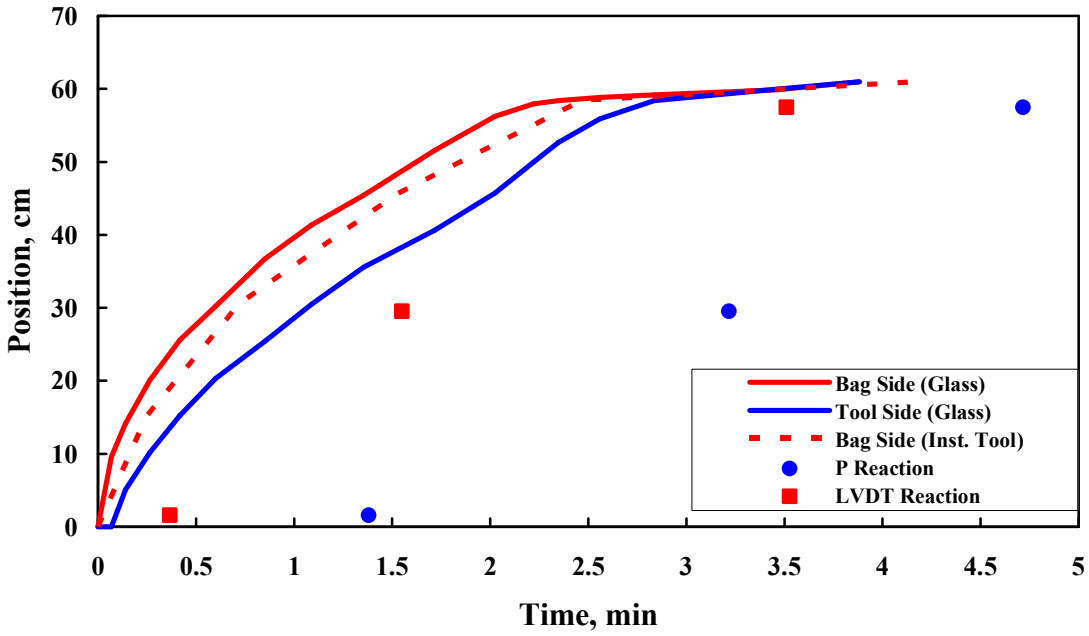

Figure 5.16: Flow front evolution in two stacks MAWK panel.

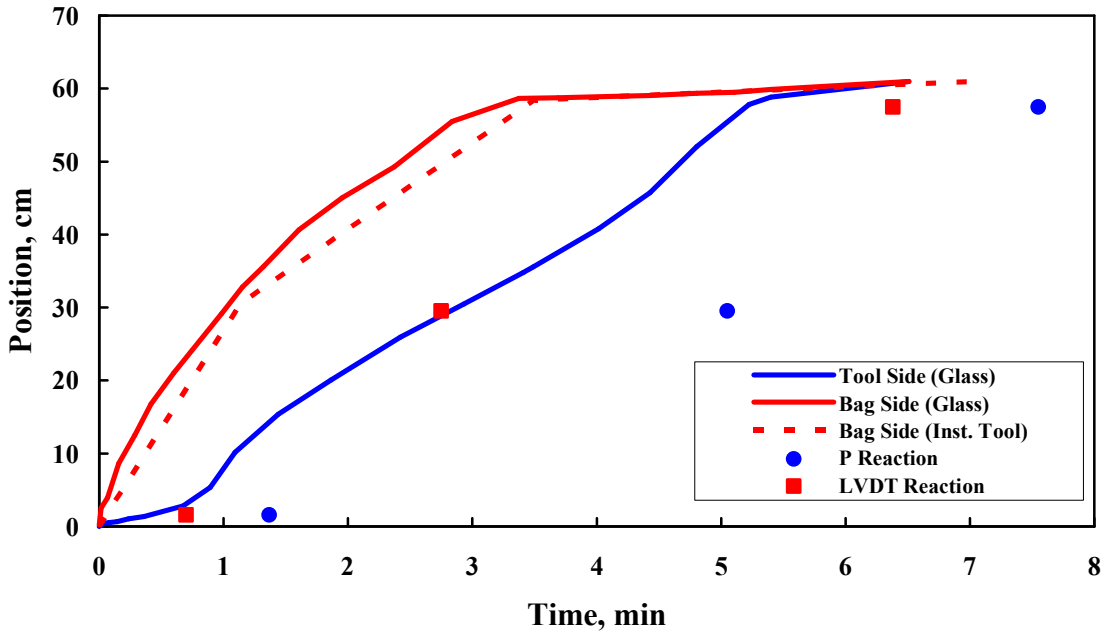

Figure 5.17: Flow front evolution in four stacks MAWK panel.

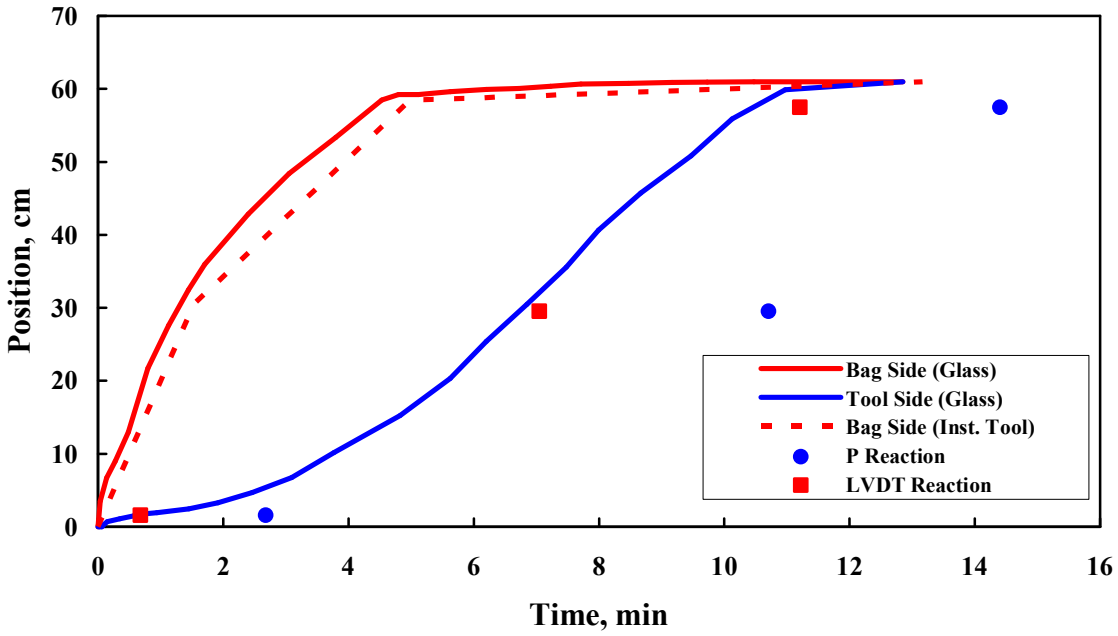

Figure 5.18: Flow front evolution in eight stacks MAWK panel.

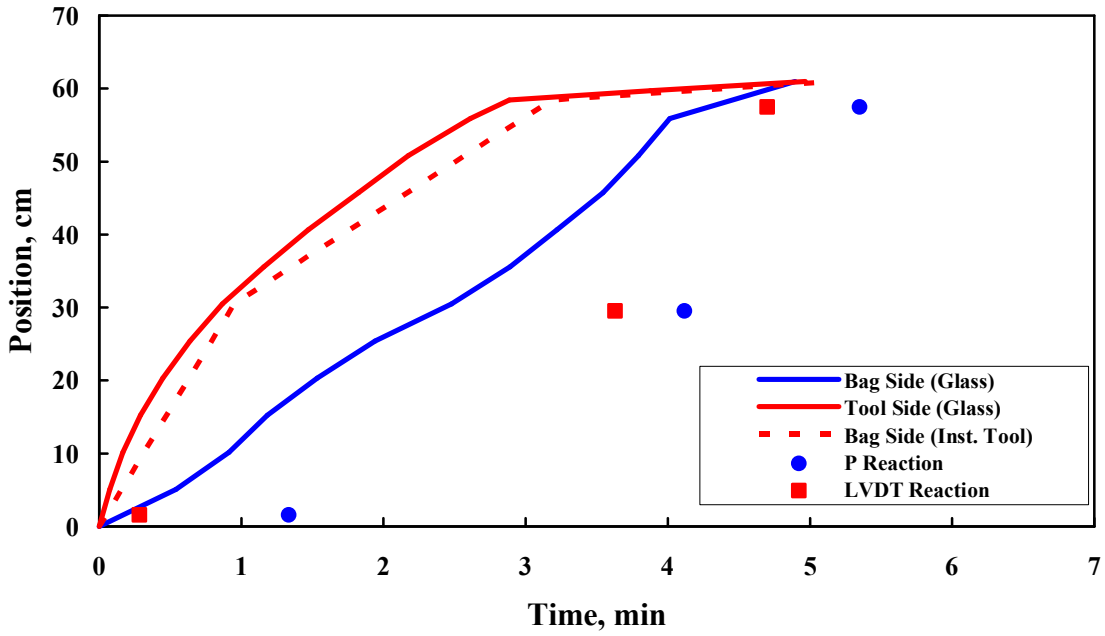

Figure 5.19: Flow front evolution in 10 layers biaxial ppreform.

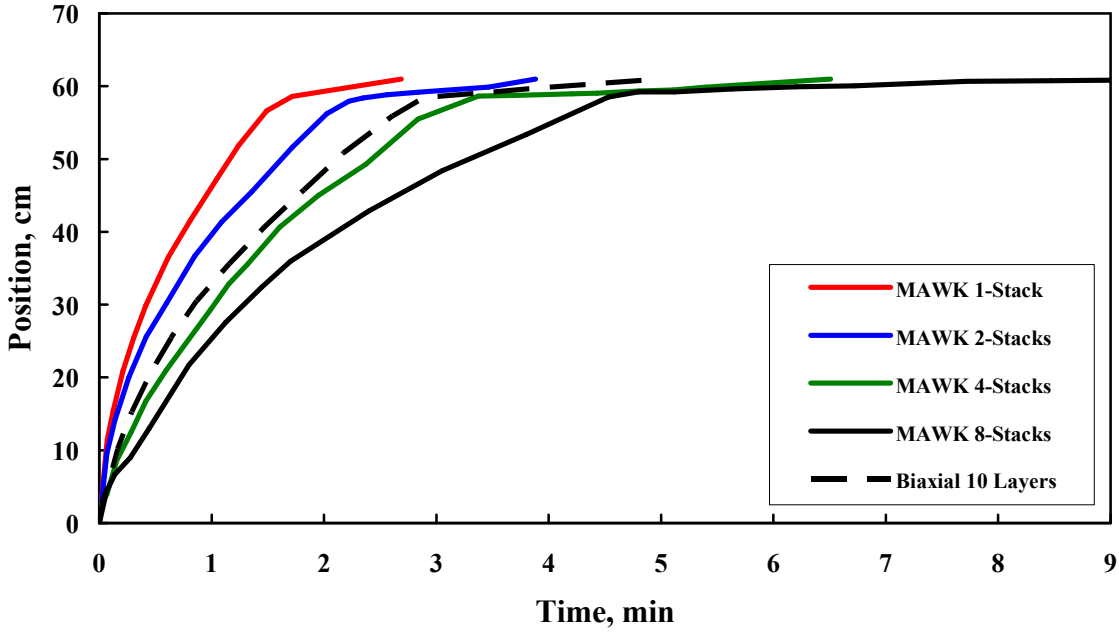

Figure 5.20: Bag side flow front evolution comparison.

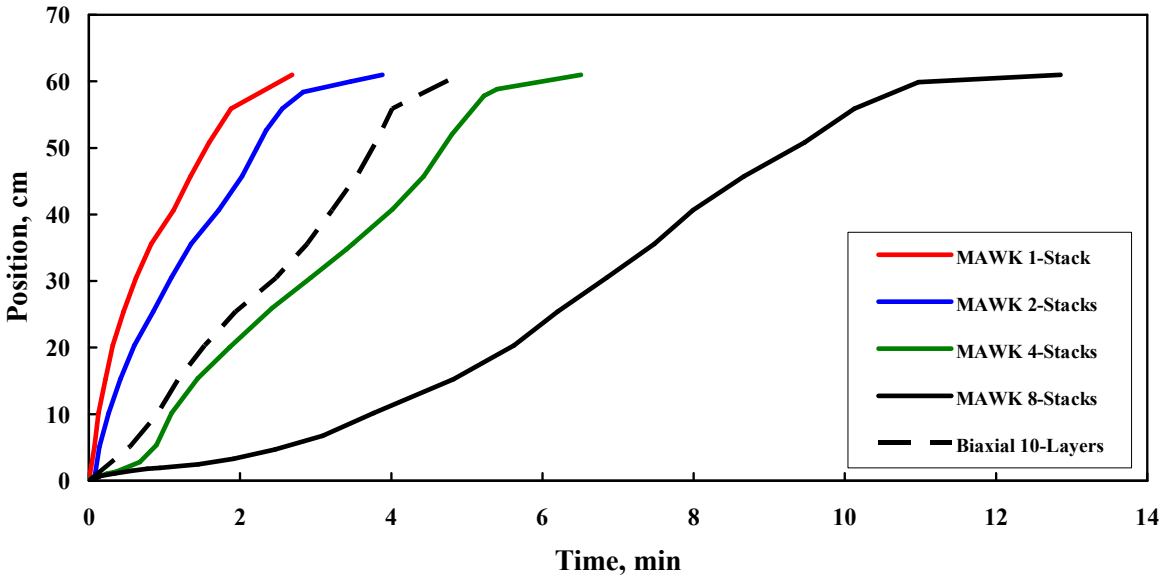

Figure 5.21: Tool-side flow front evolution comparison.

In comparing the bag-side flow front data from the IT and GT experiments there was a slight variation found for each of the experiments. The GT top flow front evolved more rapidly in each specimen. This trend is due to the viscosity of the fluid. The GT tests were performed during the summer months when the lab temperature was slightly elevated in comparison to the lab temperature during the IT tests, which were all performed in January and February. The average viscosity of the GT test fluid was measured to be 0.252 Pa·s while the IT test fluid was found to average 0.265 Pa·s. While this variation in the data is easily explained, the comparison of the pressure sensor reactions with the bottom flow front results for the GT is surprising. For every specimen, there is an unexpected difference between the flow front observed in the GT experiment and the measured reaction time of the pressure sensors used in the IT tests. The resulting times and flow front positions as well as the pressure and displacement data are included in Table 5.2.

For the middle of the panel where the flow front position is 29.5 cm, comparing the GT bag-side flow front time to the pressure sensor reaction time results in an approximately 80% difference. This was consistent for all of the specimens except for the two stack MAWK where the pressure sensor lagged the GT observed flow by 40%. This consistently large lag cannot be explained by the small difference in viscosity. Figure 5.22 shows a schematic of the flow front developing on the GT and at the site of the pressure sensor in the IT. Because these diaphram pressure sensors will not operate in a flush-mount position, the sensor must be recessed into the surface of the aluminum instrumented tool as shown in the diagram. In this test bed the sensors are recessed 0.20 cm below the surface. Recessing the sensor creates a cavity of 0.58 cm^3. If the pressure sensors do not react until some or all of this volume of fluid has entered the cavity, the resulting fill times would be greater than those found for the flow front observed on the GT. Reviewing the data in Table 5.2 shows this to be the case for all of the pressure sensor reaction times. Filling this cavity with fluid was not considered to be an issue previously. However, the results of this comparison brings into question the reliability and accuracy of this configuration. Because the pressure sensor data was also used

in the wetted preform compaction experiments of Chapter 2, this data may also be questionable. However, the compaction tests were conducted under quasi-static conditions.

Table 5.2: Flow front comparison data for the glass tool and instrument tool infusion experiments.

Specimen	Flow Front Position, cm	Time, min GT, bag-side	Time, min GT, tool-side	Time, min IT bag-side	Time, LVDT Reaction	Time, P-Sensor Reaction
One Stack	1.59	0.009	0.023	0.013	0.183	0.533
	29.5	0.411	0.603	0.461	0.967	1.667
	57.49	1.623	2.039	1.732	2.533	2.867
	End	2.689	2.689	2.883	N/A	N/A
Two Stack	1.59	0.011	0.043	0.018	0.367	1.379
	29.5	0.594	1.081	0.708	1.548	3.217
	57.49	2.219	2.815	2.397	3.509	4.717
	End	3.882	3.882	4.167	N/A	N/A
Four Stack	1.59	0.010	0.420	0.015	0.678	1.367
	29.5	0.979	2.912	1.121	2.746	5.048
	57.49	3.361	5.218	3.431	6.378	7.549
	End	6.508	6.508	7.033	N/A	N/A
Eight Stack	1.59	0.016	0.569	0.019	0.677	2.679
	29.5	1.356	6.825	1.521	7.048	10.710
	57.49	4.463	10.426	4.785	11.210	14.404
	End	12.851	12.851	13.167	N/A	N/A
Biaxial	1.59	0.024	0.168	0.036	0.283	1.533
	29.5	0.639	2.478	0.951	3.630	4.367
	57.49	2.842	4.455	3.043	4.690	5.533
	End	4.973	4.895	5.153	N/A	N/A

The Vf level for each level of compaction pressure was recorded after the pressure had reached a steady-state and held for approximately 200 seconds. The pressure was also

recorded manually from a pressure gauge to ensure reliability. Since, the pressure data found in the instrumented tool experiments is offset with respect to the time the LVDT reacts, due, presumably, to the excess volume needed to fill the sensor cavity, it is impossible to compare the results of the wet unloading empirical models found in Chapter 2 to the preform release which occurs in Figures 5.8 through 5.12.

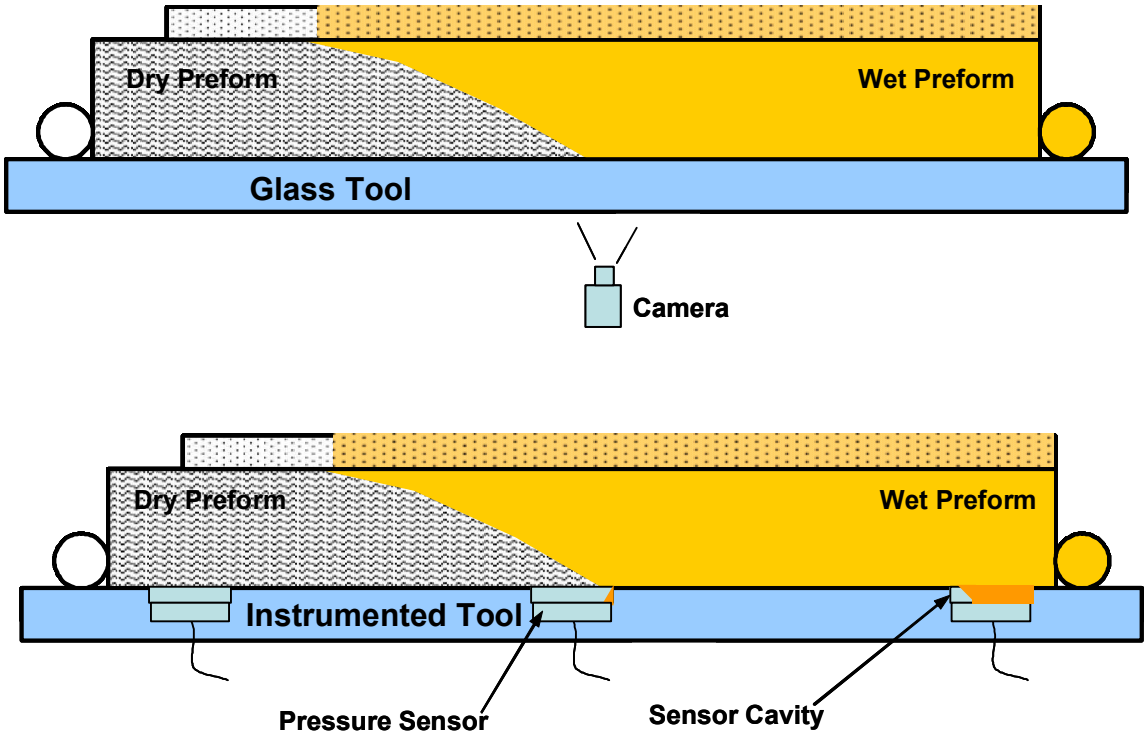

Figure 5.22: Flow front evolution and assumed cavity effects in the instrumented tool experiments.

To determine the effects of the cavity volume on sensor reaction times, an experiment was conducted on the instrumented tool using four layers of a 3k woven glass fabric. The glass fabric was used to more easily see the fluid flow front through the thickness of the preform to the tool surface. The glass fabric was laid on the tool, as described in Figure 5.3, so that pressure sensor #1 (P1) and #2 (P2) were covered with both the fabric and three layers of the Plastinet® distribution media. For the sake of this experiment, the media was stopped

approximately 5 cm short of pressure sensor #3 (P3). This would slow the flow front as it approaches the third sensor and ensure that the flow on the bottom surface of the preform matched the top surface. The results of the experiment are shown below in Table 5.3. The "observed time" was recorded when the flow front reached the front rim of the pressure sensor cavity. The pressure "sensor reaction time" was indicated as in all previous tests when the pressure increased due to the hydrostatic pressure of the entering fluid.

Table 5.3: Pressure sensor reaction during glass fabric infiltration experiment.

	P1 Reaction, sec	P2 Reaction, sec	P3 Reaction, sec
Observed flow front	2	23	215
Sensor Reaction	5	31	246
Difference	3	8	31

The results of the test indicate that a time difference exists between the observed fluid flow front and the pressure sensor reaction. The time difference observed at the P1 and P2 locations may be explained by the time required for the fluid to flow through the thickness of the preform. The thin four layer woven glass preform specimen was chosen to reduce this effect. The flow front at the P3 location was uniform with respect to top and bottom flow front. The large lag between the observed flow front and the sensor reaction at this location indicates some effect due to the pressure sensor. The increase in the time lag as the distance from the fluid source increases, i.e. P1 to P2 to P3, indicates that the volume of resin required to fill the sensor cavity becomes an issue as well. At P3, the distribution media was not present above the sensor, therefore, the volume of resin needed to fill the sensor cavity is flowing into the region at a much smaller rate, hence the large difference in time for the sensor to react.

Due to the descrepencies found between the observed bottom flow front in the GT experiments and the IT pressure sensor reaction times, an attempt to compare the compaction models developed in Chapter 2 to the relaxation of the preforms during actual VARTM infusion of the preforms may be tenuous, at best. Figures 5.23 through 5.27 show the comparison plots between the change in fiber volume fraction during the VARTM infiltration experiments and the compaction models developed from the relaxation of the wetted preforms in the compaction tests. To reduce error in making these comparisons, the relaxation data obtained from LVDT1 and P1 (Figures 5.8-5.12) of the IT experiments is presented in the figures. These sensors are the first to react with the flow front as the panel is infused and, from Figures 5.15-5.19, appear to have the smallest gap in reaction time. Given that the reaction times between pressure and LVDT are not ideal, the compaction model correlates very well with the relaxation of the preform during the VARTM infiltration.

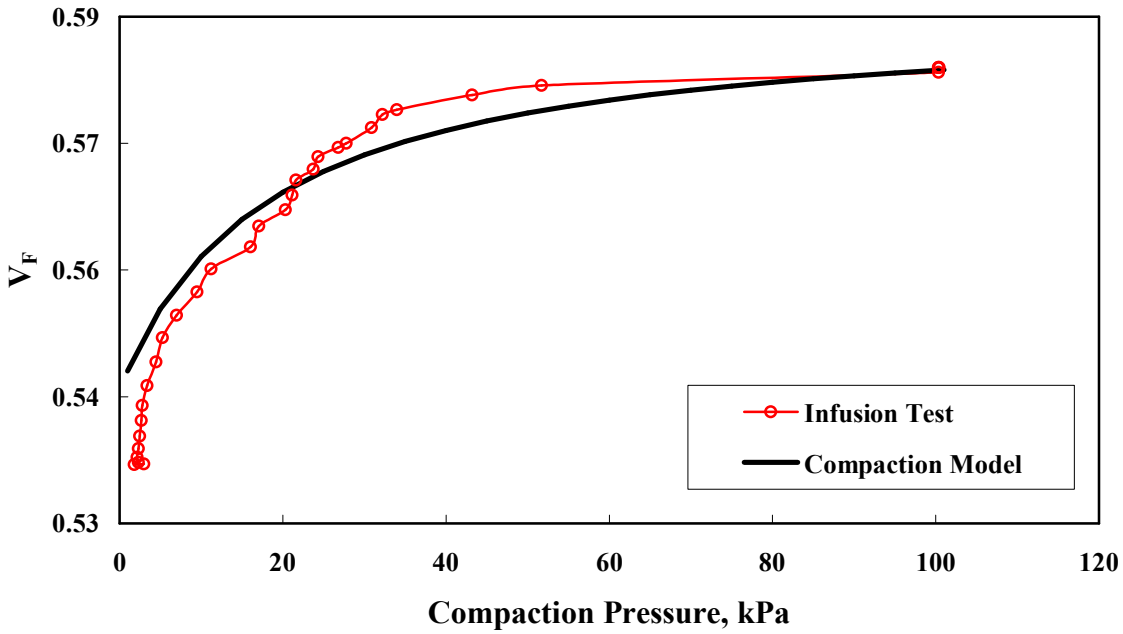

Figure 5.23: MAWK, one stack: Comparison of wet preform compaction model to preform relaxation during actual VARTM infusion relaxation.

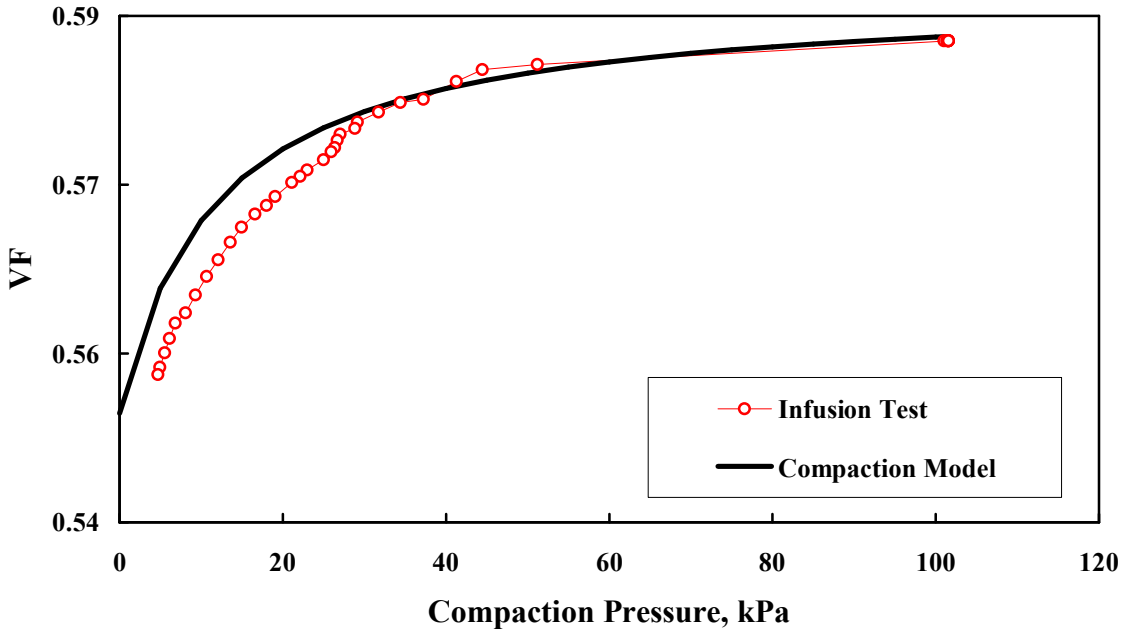

Figure 5.24: MAWK, two stack: wet-compaction model and VARTM infusion relaxation.

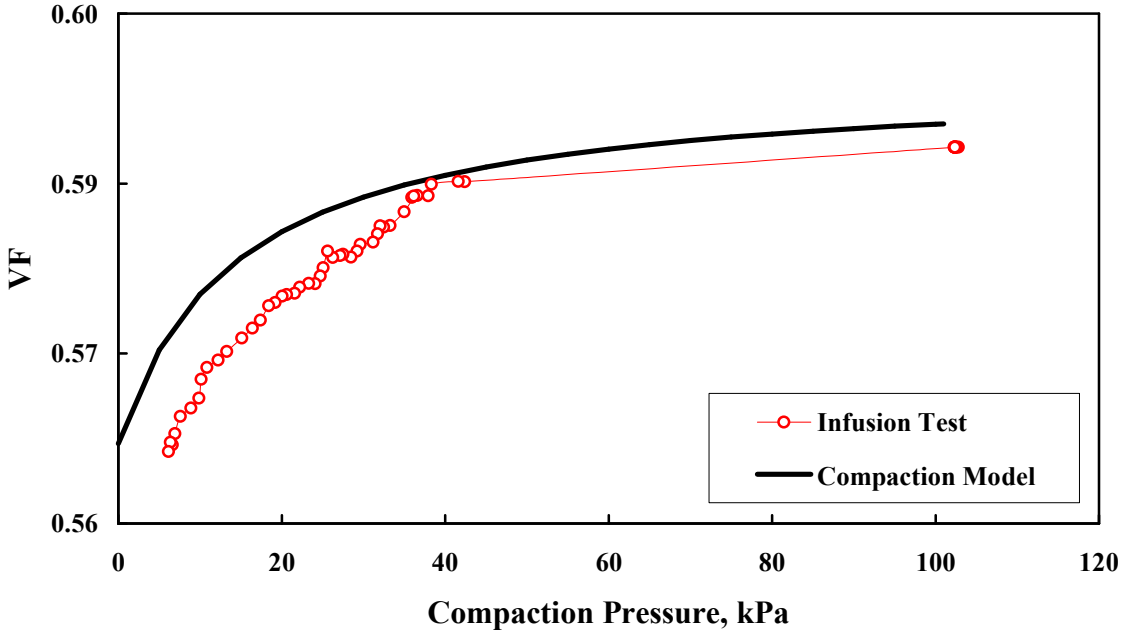

Figure 5.25: MAWK, four stack: wet-compaction model and VARTM infusion relaxation.

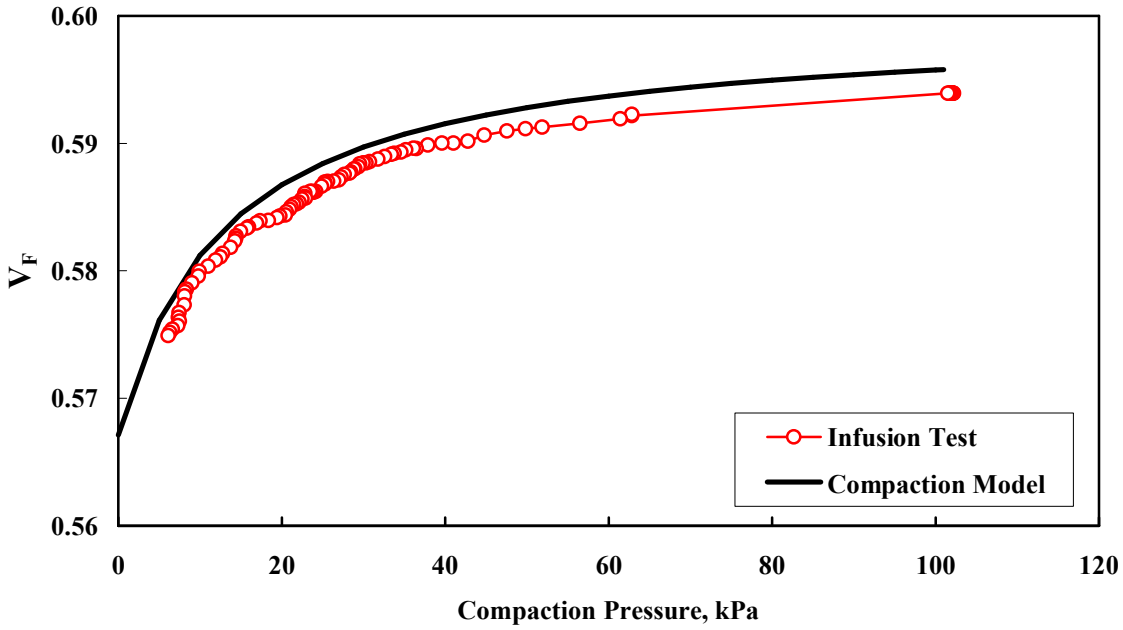

Figure 5.26: MAWK, eight stack: wet-compaction model and VARTM infusion relaxation.

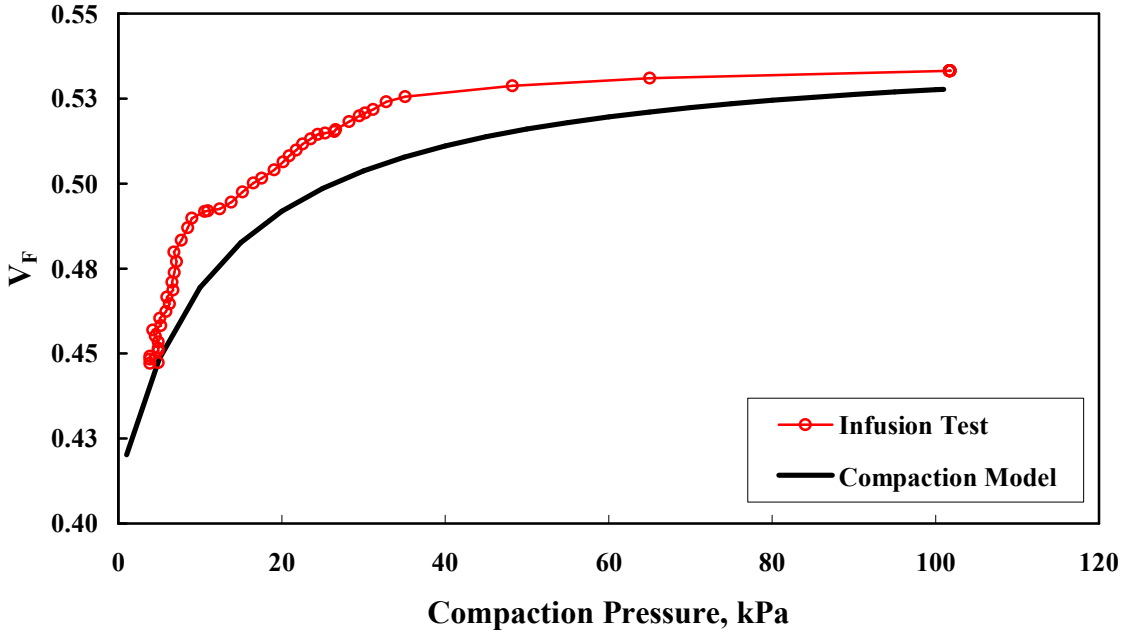

Figure 5.27: Biaxial, ten layers: wet-compaction model and VARTM infusion relaxation.

5.3.3 Fiber Volume Analysis Results The results of fiber volume analysis are included in Table 5.4 and a micrograph of the four stack panel with SI-ZG-5A epoxy matrix is included in Figure 5.28. The micrograph indicates that the fibers were well wet-out and no voids were evident in this sectioned portion of the panel. The V_f obtained in the acid digestion (AD) experiments of the resin infused panels shows that increasing the number of stacks in the MAWK preform specimens results in an increase in the maximum achievable V_f. This trend agrees with the results found in the preform compaction characterization of Chapter 2 and in the results presented previously in this chapter. This trend was evident in the results of the acid digestion experiment, regardless of the epoxy resin used in the VARTM infiltration of the composite panels. The V_f values obtained by AD were all slightly lower for the MAWK panels than were obtained in the compaction experiments for preform specimens wetted with oil from Chapter 2. The preform specimens in these experiments were wetted with oil using a proprietary method. The wetted specimens were then held under vacuum until the pressure sensors reached a steady state at or close to 760 mm Hg. The maximum fiber volume reported in the compaction experiments may be considered an "ideal" value that cannot be reached under normal VARTM process conditions. The main purpose of the compaction test was to capture the overall behavior, i.e. compaction curve, in both dry and wet environments. Therefore, the maximum V_f reported in column two of Table 5.4 is presumably the highest fiber volume attainable for the MAWK material preform specimens without long compaction holds. However, the values obtained by AD shown in column 3 are only slightly lower than those obtained in the compaction experiments. The AD values were obtained from panels infused using the conventional VARTM, or SCRIMP, process, clamping for 15 minutes after saturation and curing with a secondary bag to ensure no leaks. Given that the V_f analysis was performed using data from three specimens retreived from one panel for each category, the numbers represent the maximum V_f attainable for the MAWK preform by conventional VARTM infusion.

Table 5.4: V_f analysis results and comparison to compaction response characterization.

Specimen	Maximum Avg V_f (%), Wet(Oil) Compaction Experiments	Avg V_f (%), Acid Digestion Experiment	Void Volume (%), Acid Digestion Experiment
MAWK, 1-Stack SI-ZG-5A Epoxy	57.871 +/-0.233	57.755 +/-0.14	0.19 +/-0.04
MAWK, 2-Stack SI-ZG-5A Epoxy	58.320 +/-0.066	57.795 +/-0.13	0.175 +/-0.02
MAWK, 2-Stack VR56-4 Epoxy	58.320 +/-0.066	57.768 +/-0.20	0.15 +/-0.08
MAWK, 4-Stack SI-ZG-5A Epoxy	59.027 +/-0.196	58.035 +/-0.16	0.13 +/-0.09
MAWK, 4-stack VR56-4 Epoxy	59.027 +/-0.196	57.910 +/-0.19	0.14 +/-0.02
MAWK, 8-stack SI-ZG-5A Epoxy	59.578 +/-0.991	58.135 +/-0.13	0.235 +/-0.04
Biaxial, 10 layers SI-ZG-5A Epoxy	52.775 +/-0.297	53.951 +/-0.08	0.024 +/-0.005
Biaxial, 20 layers SI-ZG-5A Epoxy	52.852 +/-0.089	53.944 +/-0.12	0.033 +/-0.008

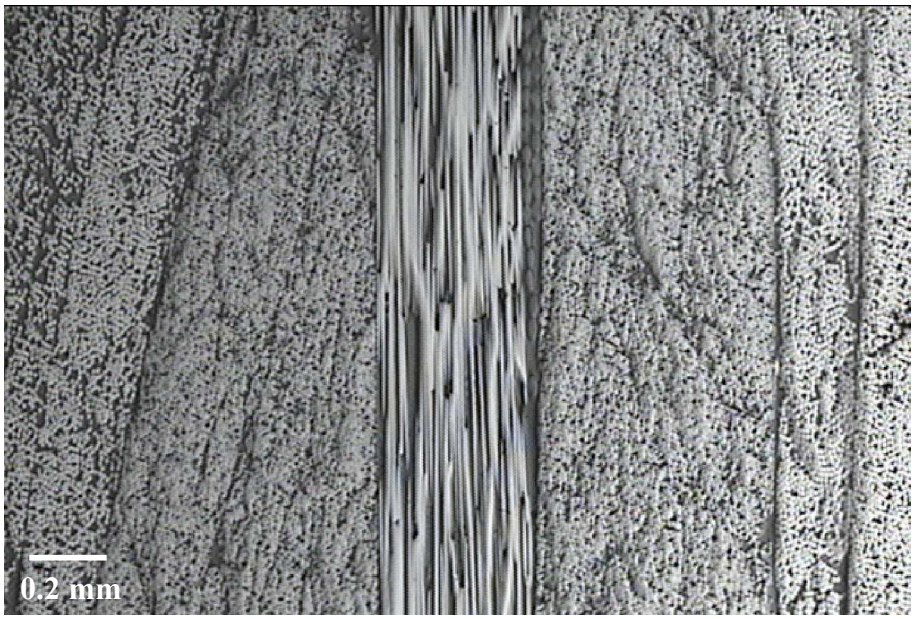

Figure 5.28: Micrograph of cross-section of four stack MAWK/SI-ZG-5A panel after cure.

As expected, specimen thickness did not influence the final V_f of the biaxial preform panel specimens. However, the resulting fiber volumes of these cured specimens were slightly higher than the results found in the compaction experiments. While both the MAWK and the biaxial preforms have exhibited a time-dependent response to compaction, as was shown in Figure 5.12, the the wetted biaxial preform requires more time to reach the maximum achievable level of fiber volume. From the end of the infusion to the time when the resin gel point is reached during oven cure, the preform may further compact and achieve a higher V_f than was attainable during the quasi-static compaction experiments despite the ideal conditions experienced in the compaction test procedures. Although these results show that the 60% fiber volume level cannot be achieved using the woven biaxial preform, the AD results also indicate that further investigation of the compaction response is needed for this biaxial preform material and its time dependent compaction behavior.

Chapter 6

Summary and Conclusions

Vacuum-assisted resin transfer molding (VARTM), a variant of the traditional resin transfer molding (RTM) process, has advantages over the conventional RTM by eliminating the costs associated with matched-metal tooling and allows for composite infusion and consolidation under pressures at or below 101.5 kPa. VARTM is typically a three-step process including lay-up of a fiber preform, impregnation of the preform with resin, and cure of the impregnated panel. The reinforcement, in the form of woven carbon or glass fabric, is laid onto a rigid tool surface. The matched metal tool commonly found in RTM is replaced in the VARTM process by a formable vacuum bag material. The resin is injected through single or multiple inlet ports, depending upon part size and shape. A vacuum port allows the fiber preform to be evacuated prior to injection and provides the mechanism for transfer of the resin into the part. The preform infiltration time is a function of the resin viscosity, the preform permeability and the applied pressure gradient. The infiltration time can be greatly reduced by utilizing a distribution medium, or SCRIMP cloth, with a higher permeability than the preform. Consequently, the resin flows in the medium first and then the infiltration process continues through the preform thickness.

One of the most significant challenges in the use of VARTM for aerospace components is improving the mechanical performance of the composite by increasing the achievable level

of fiber volume fraction to near 60%. Development of the VARTM process during the TCAT program focused on investigating and characterizing both the VARTM process and its constitutive materials to improve the performance of the resulting parts by achieving the 60% fiber volume threshold. This involved work to characterize both the compaction and flow behavior of carbon fiber preforms. The flow and curing behavior of high performance epoxy systems were characterized. In addition, infusion experiments were performed to better understand the preform compaction and fluid flow behavior during actual VARTM infiltration.

6.1 Preform Compaction

Both the dry and wet compaction behavior of preform specimens containing one, two, four, eight and sixteen stacks of the SAERTEX® multi-axial, warp-knit (MAWK) carbon fabric preforms and specimens containing ten and twenty layers of 5-harness satin, biaxial woven carbon fabric were characterized under VARTM conditions. An L-gage laser displacement sensor was used to determine the uncompacted thickness of the preform specimens. At a vacuum level of 12.7 mm Hg (1.7 kPa compaction pressure) the test was started and the specimens were compacted by step increases of the vacuum level to a maximum level of 760 mm Hg (101.5 kPa). In all of the tests performed for each of the preform specimens, increasing the level of vacuum, or compaction pressure, resulted in a decrease in thickness and, therefore an increase in fiber volume fraction.

Compaction of the MAWK and biaxial fabric under dry, quasi-static test conditions resulted in maximum achievable fiber volumes of 59.5% and 50.0%, respectively, at a compaction pressure of 101.5 kPa. Both materials exhibited a hysteresis phenomenon when the compaction pressure was released under dry conditions, which indicated a permanent deformation of the preform for the period of times tested. In addition, the V_f of MAWK fabric was found to increase with the addition of stacks of preform material, i.e., the sixteen-stack specimen was found to have the highest maximum fiber volume of 59.5% while the one stack average maximum was 57.8%. This behavior was not evident in the biaxial specimens tested. The resulting V_f versus compaction pressure curves were not linear. These

curves indicated that the majority (up to 85%) of the change in V_f occurs in the range of 0.0 to 381.0 mm Hg (50.5 kPa). Dry release of the preform indicated very little reduction in V_f until the preform compaction pressure had been reduced from 101.5 kPa to approximately 50.8 kPa.

The maximum achievable V_f of the preform specimens under wet conditions was found to reach 60.2% for the MAWK preform and 52.8% for the biaxial material. The lubrication effect found in earlier work was evident, but was also found to be dependent on the amount of time that the dry preform compacted prior to introduction of the wetting fluid. Holding the dry specimen for up to ten hours under 101.5 kPa resulted in the specimen reaching a state of maximum nesting and, therefore, for these specimens, no further increase in fiber volume was evident using the characterization techniques described in this work. The wet compaction experiments revealed the same behavior of increasing V_f with increasing stacks contained in the MAWK specimen. The reason for this behavior is not fully understood, however, it is assumed to be a result of increased nesting in the interstack region.

The V_f versus compaction pressure curves resulting from both the dry and wet experiments were fit to empirical models relating preform strain to compaction pressure. Statistical analysis of these curves for multiple compaction tests of each specimen type resulted in reasonably low deviation from the mean. It was shown that the flow behavior of the preform is dependent on the porosity and therefore the preform V_f and strain. Prediction of preform infusion is therefore dependent on its characteristic compaction behavior. The empirical models found in the compaction characterization experiments can be used as input for flow simulation models.

6.2 Preform Permeability

The flow behavior of the MAWK and biaxial preforms were characterized using well established techniques to determine the Darcy permeability. Both the in-plane and transverse permeabilities were detemined for various specimen thicknesses under steady state flow conditions. The permeability was calculated from pressure versus superficial velocity data for fiber volume fractions ranging from 35% to 55% for the biaxial specimens and 45% to

59% for the MAWK preforms. The pressure measured at the inlet point of the permeability fixtures never exceeded 101 kPa. In all of the tests performed, the calculated Darcy permeability decreased as the preform was compacted to higher fiber volume levels.

The average value for the in-plane, S_{xx}, permeability of the MAWK preform was found to range from 6.8 x 10^{-11} m^2 to 8.0 x 10^{-12} m^2 for V_f ranging from 45% to 59%. The in-plane, S_{yy}, average values were found to range from 3.5 x 10^{-11} m^2 to 4.8 x 10^{-12} m^2 over the same V_f range. The higher permeability in the *x*-direction is due to the increased number of fiber tows in the MAWK preform that are parallel to the fluid flow vector. The transverse permeability, S_{zz}, was found to vary range from 2.3 x 10^{-12} m^2 to 3.0 x 10^{-13} m^2 for the stated V_f range. The Szz value is two orders of magnitude lower than the inplane values because the fluid flow is perpendicular to all of the fiber tows, which creates a greater resistance. The thickness of the MAWK fabric was varied by adding additional stacks up to a maximum of sixteen. However, a relationship did not develop as was seen in the compaction experiments which correlated a change in permeability due to thickness changes. When comparing the results for one, two, four, eight and sixteen stack specimens, the in-plane and transverse permeability values were within the scatter, thus indicating that the interstack nesting phenomenon does not influence the permeability value. It is possible that the test procedure is not sensitive enough to determine an intersatack influence on permeability. However, because of the relationship between fiber volume fraction and permeability from Darcy's law the influence of the number of stacks could be observed in plots of permeability versus pressure. The pressure values were back-calculated from the empirical equations developed in the compaction experiments. When the data were plotted in this manner the permeabiltiy values were found to decrease with increasing number of stacks for the same value of compaction pressure. The average value of permeability for all of the MAWK thickness configurations was fit to an empirical equation for S_{xx}, S_{yy} and S_{zz} which can be used in process model simulations.

Tests were performed on biaxial preform specimens containing ten and twenty layers of fabric. The permeability was determined for both in plane and transverse flow and no thickness influence was found. The in-plane average values ranged from 3.0 x 10^{-10} m^2 to

3.5 x 10^{-11} m^2 for V_f ranging from 35% to 55% while the transverse values were found to range between 9.3 x 10^{-12} m^2 and 9.4 x 10^{-12} m^2. The permeability values were higher than the results found for the MAWK due to the higher porosity of the biaxial preform. The average values of peremability for the biaxial preform were also fit to an equation for future use in process model simulations.

6.3 Resin Characterization

The properties that govern the processing characteristics have been characterized for an amine-cured, VR-56-4, and an anhydride-cured, SI-ZG-5A, epoxy system. Relationships for resin viscosity and degree of cure were shown to accurately model the observed resin characteristics. Results of cure simulations performed using a process model show that the two resins have similar minimum viscosities but significantly different curing behaviors. The cure reaction of SI-ZG-5A occurs more quickly and at a lower temperature, but with a higher exotherm than that of the VR-56-4 resin. Both curing cycles examined show that time to resin gel and exotherm are strong functions of the cure cycle characteristics and resin properties. However, the VR-56-4 appears to be more sensitive to the cure cycle selection. Despite its higher initial viscosity, the calculated flow number, an indication of potential resin flow, for the VR-56-4 is about twice as large as that found for SI-ZG-5A.

6.4 VARTM Process Characterization

Experiments were conducted using an instrumented VARTM tool to measure the change in thickness and the hydrostatic pressure of the preform during an actual VARTM infusion. The flow front evolution on the top surface of the distribution media and preform was recorded using a digital video camera. These tests were conducted for one, two, four and eight stacks of the MAWK preform material, as well as a 10-layer biaxial specimen. It was found that holding the MAWK specimen for up to ten hours under full vacuum resulted in little or no evidence of the lubrication effect noted previously in the compaction experiments of Chapter 2 and other work. The fiber volume fraction was found to be at a maximum under full vacuum prior to infusion of the preform by a wetting fluid. The fluid flowed into

the preform due to the difference in pressure between the dry compacted preform contained within the bag at 760 mm Hg (0.0 kPa fluid pressure) and the fluid contained outside of the bag at 0.0 mm Hg (101.5 kPa). The fluid flowed into the media and preform, after opening the resin port, and the LVDTs indicated an increase in thickness due to the increase in hydrostatic pressure and subsequent decrease in compaction pressure.

In all of the instrumented tool experiments the LVDT thickness sensors on the top of the bagged preform were found to react before the pressure sensors located beneath the preform despite the identical location in relation to the advancing flow front. This indicates that the upper layers of fibers react to the hydrostatic pressure as the fluid flows transversely from the distribution media on the top surface through the preform prior to the fabric becoming fully saturated in the localized region of the pressure sensor. The LVDTs indicated the maximum thickness (minimum V_f) was reached when the hydrostatic pressure had reached a maximum. This typically occurred after the fluid had reached the end of the media on the top surface and was near to full saturation of the entire 30 cm x 60 cm preform specimen. Comparing the results of these experiments for the MAWK specimens of different thicknesses indicated that a greater reduction of the V_f occurred for the one and two stack specimens than for the four and eight stack specimens. It is postulated that this phenomenon is due to the influence of the gap left between the end of the distribution media and the end of the preform specimen. In each test the gap was 2.54 cm regardless of the thickness of the preform. When the fluid reached the end of the media, the flow front moved much more slowly, however the change in the volume flow rate of fluid does not change at the same rate. The volume of fluid entering the preform carries the hydrostatic pressure which reduces the compaction pressure on the preform. For the thinner specimens the time needed to fill the remaining 2.54 cm of preform allows enough volume of fluid to flow into the preform to cause a greater relaxation of the preform. In the thicker specimens the through-thickness flow front is more parabolic in shape due to the gap from the top surface to the bottom surface. This means that a greater volume of fiber is dry when the top flow front reaches the end of the media. The extra volume of fluid in the thinner preforms does not translate to excessive volume in the thicker preform specimens. This volume of resin fills the dry fibers

near the tool surface. It is assumed that reduction of the "end of media/end of preform" gap would improve the retention of fiber volume for the thinner preform specimens.

Comparison of the LVDT, pressure and the video data indicated that the time to fill, or fully wet-out the preform specimen increases with increased thickness, or number of stacks. After the preform specimen was fully saturated with fluid, the resin port was closed and the vacuum left open. At this point, the three LVDTs indicated a difference in thickness across the length of the specimen, i.e. the preform was thicker at the fluid inlet side than at the vacuum side. For the MAWK specimen it was found that continuing to pull vacuum on the bagged preform resulted in a reduction in thickness across the entire length of the panel, but also that the difference in thickness between the fluid and vacuum side could be greatly reduced if not eliminated within approximately fifteen minutes. In this amount of time the pressure sensors also reached a steady state. The same behavior was observed in the biaxial specimen, however; the amount of time necessary to reach the same results was much greater for this preform type due to the greater porosity and therefore greater volume of fluid present when the material was fully wet-out.

The time to reach full saturation was also investigated by observing the flow of fluid in the preform using a glass tool. These experiments showed an increase in the lag between the top and bottom surface of the preform as the MAWK specimen thickness was increased from one, two, four and eight stacks. The results of the glass tool experiments were compared with the LVDT and pressure sensor reactions from the instrumented tool experiments. The top surface flow fronts were found to match quite well, however the pressure sensor reaction times did not match those of the glass tool bottom surface. This generated concern that the mounting configuration of the pressure sensors and the resulting gap may affect their reliability for true indication of the flow front location. The results of the glass tool infusion experiments will be valuable for future validation of infusion simulations using process models such as 3DINFIL.

In an effort to validate the results of the compaction experiments, the V_f versus compaction pressure data found in the istrumented tool experiments were compared to the empirical equations developed in Chapter 2 for the wet release of the preform. The empirical

compaction models were found to capture the shape of the curve and match quite well with the magnitude as well. The maximum fiber volumes at 101.5 kPa did not vary more than 1%. The one and two stack MAWK specimen data was found to match the model fit curves better than the thicker four and eight-stack preforms. This could be due to the unsubstantiated error in the pressure sensor data which was found to be worse for the thicker specimens.

Fiber volume fraction and void content of composite panels fabricated using the MAWK and biaxial preforms and an epoxy resin were found using the acid digestion experiment technique. The resulting V_f values were found to be slightly greater than those found in the VARTM istrumented tool infiltration experiments. The preform specimens used to fabricate the composite panels underwent the identical long duration dry compaction and the fifteen minute recompaction after infusion. In addition, the composite panels were held under vacuum for an additional time during an elevated temperature cure of the epoxy resin. Therefore, the higher fiber volumes of the composite panels may be due to the additional compaction time experienced during the cure cycle. In contrast, the fiber volume fractions found in the compaction experiments were slightly greater than the panel values. This is due in part to the technique used to perform the wet compaction experiments. This technique results in an idealized value of V_f at the higher compaction levels. The average void content of each of the composite panels were found to be less than 0.5%.

6.5 Future Work

The most appropriate method to determine the effectiveness of the compaction and permeability experiments conducted in this work and therefore, the accuracy of the compaction and permeability empirical models is to use the results as input to the newest version of the 3DINFIL© process simulation software. The code has been updated [17] to include a compaction submodel which accounts for the change in thickness during VARTM infusion. The resulting permeability empirical data from Chapter 3 will also be used as input. The results of the simulations of flow in the various specimen thicknesses can be validated using the actual experimental data found using the glass tool. The process model

can also be used to determine how much influence the fluid viscosity will have on the fill time and decidely resolve the issue with the pressure sensor time delay. As part of this future work with the process model, a sensitivity analysis should be performed to determine the effect on pressure and V_f of varying the media gap at the end of the panel. In addition, the results of the preform characterization in Chapter 3 for the MAWK material showed that the increasing the number of stacks did not influence the measured permeability despite the effects found on the fiber volume fractions measured in the compaction characterization experiments. The process model can be used to determine which parameters, either the permeability or compaction behavior of the material, have the most influence on the simulated fill times.

Bibliography

1. Mazumdar, S. (2005). "Composites Growth Realizing its Global Potential," Composites Technology, 11(2), 7.
2. Hyer, M. (1998) ***Stress Analysis of Fiber-Reinforced Composite Materials***, McGraw Hill Publishing, Boston.
3. Dawson, D.K, (2005). "At the Top and Still Climbing," High Performance Composites, 13(2), 46-50.
4. Black, S., (2003). "Fighting Ships Augment Combat Readiness with Advanced Composites," High Performance Composites, 11(5), 30-33.
5. Brosius, D. (2004). "Composites Score Wins at SPE Awards Ceremony," Composites Technology, 10(6), 13.
6. Ostberg, D.T., R.S. Dunfee, G.E. Thomas and R.A. Brynsvold (1996). "Composite Armored Vehicle Advanced Technology Demonstrator," 41st International SAMPE Symposium, 41, 1459-1464.
7. Dawson, D.K. (2004). "Lockheed Martin makes Strides in Military Contracts", High Performance Composites, 12(5), 11.
8. Williams, J.G. and M.M. Mikulas (1975). "Analytical and Experimental Study of Structurally Efficient Hat-Stiffened Panels Loaded in Axial Compression," 16th ASME/AIAA/SAE Conference, AIAA Paper 75-754.

9. Rouse, M., D.C. Jegley, D.M. McGowan, H.G. Bush and W.A.Waters (2005). "Utilization of the Building-Block Approach in Structural Mechanics Research," 46th AIAA/ASME/ASCE/AHS/ASC Conference, AIAA 2005-1874.
10. Hergonrother, P., J. Connel, J. Smith (1998). "PETI-5" Composite Manufacturing, 6, 15-21.
11. Jegley, D.C., H.G. Bush and A.E. Lovejoy (2003). "Evaluation of the Structural Response and Failure of a Full-Scale Graphite-Epoxy Wing," Journal of Aircraft, 40(6), 880-886.
12. Karal, M. (2001) "AST Composite Wing Program: Executive Summary," NASA CR 2001-210650.
13. Senibi, S., R.L. Sadler and V.S. Avva (1995). "Resin Transfer Molding (RTM): Experiments with Vacuum Assisted Methods," SAMPE International Symposium Proceedings, 46, 1049.
14. Seemann, W.H., 1990. U.S. Patent 4,902,215.
15. Seemann, W.H., 1994. U.S. Patent 5,316,462.
16. Loos, A.C., J.R. Sayre, R.D. McGrane and B.W. Grimsley (2001). "VARTM Process Model Development," SAMPE International Symposium Proceedings, 46, 1049.
17. Song, X (2003). "*Vacuum Assisted Resin Transfer Molding (VARTM) Model Development and Verification*," Ph.D. Dissertation, Department of Engineering Science and Mechanics, Virginia Polytechnic Institute and State University, Blacksburg, VA.
18. Loos, A.C., B.W. Grimsley, R.J. Cano, P.H. Hubert (2005). "VARTM Processing of Tailored Composite Structures for Aerospace Applications," SAMPE Symposium and Exhibition, 49.
19. Song, X., B.W. Grimsley, R.J. Cano, A.C. Loos and P. Hubert (2002). "VARTM Process Modeling of Aerospace Composite Structures," 17th Annual Technical Conference of the American Society of Composites, 17, CD-ROM.
20. Lin, R. J., L. J. Lee, and M. J. Liou, (1993). "Mold filling and curing Analysisin Liquid Composite Molding," Polymer Composites, 14(1), 71-81.

21. Grimsley, B.W., P. Hubert, X. Song, R.J. Cano, A.C. Loos and R.B. Pipes (2001). "Flow and Compaction During the Vacuum Assisted Resin Transfer Molding Process," International SAMPE Technical Conference, 33, 140-153,
22. Hammami, A. (2001). "Compaction in the Vacuum Resin Infusion Molding Process," Polymer Composites, 22(3), 337.
23. Williams, C., S.M.Grove and J. Summerscales (1996). "Resin Infusion under Flexible Tooling: a Review," Composites Part A, 27A, 517-524.
24. Chen, B. and T. Chou (2000). "Compaction of woven-fabric preforms: nesting and multi-layer deformation," Composites Science and Technology, 60(12), 2223-2231.
25. Andersson, M., S. Lundstrom, B.R. Gebart and R. Langstrom (2000). "Development of Guidelines for the Vacuum Infusion Processes," FRC2000: 8th International Conference on Fiber Reinforced Composites, 8, 113-120.
26. Somasheka, A., S. Bickerton and D. Battacharyya (2004)." Non-Elastic Effects during Compression of Fiber Reinforcements," 7th International Conference on Flow Processes in Composite Materials, 7, 418-425.
27. Kruckenberg, T. and R. Paton (2004). 7th International Conference on Flow Processes in Composite Materials, 7, 425-432.
28. Darcy, H. (1856). *Les Fontaines publique de la ville de Dijon*. Paris, Dalmont, 1856.
29. Collins, R.E. (1961). *Flow of Fluids through Porous Materials*. New York: Reinhold Publishing.
30. Gauvin, R. and M. Chibani (1986). "The Modelling of Mold Filling in Resin Transfer Molding," International Polymer Processing, 1, 42-46.
31. Carman, P.C. (1937). "Fluid Flow through Granular Beds," Trans. Int. Chem. Eng., 15, 150-166.
32. Gebart, B.R. (1992). "Permeability of Unidirectional Reinforcements for RTM," Composite Materials, 26, 1100-1133.

33. Gutowski, T.G., T. Morigaki and Z. Cai (1987). "The Consolidation of Composite Laminates," Composite Materials, 21, 172-188.

34. Gokce, A. and S. Advani (2001). "Permeability Estimation with the Method of Cells," Composite Materials, 35, 713-728.

35. Trevino, L., K. Rupel, W. B. Young, M.J. Liou and L.J. Lee (1991), "Analysis of Resin Injection Molding in Molds with Preplaced Fiber Mats. I: Permeability and Compressability Measurements," Polymer Composites, 12, 20-28.

36. Lai, Y-H., B. Khomani and J.L. Kardos (1997). "Accurate Permeability Characterization of Preforms used in Polymer Matrix Composite Fabrication Processes," Polymer Composites, 18, 368-377.

37. Hammami, A (2001). "Key Factors affecting Permeability Measurement in the Vacuum Infusion Molding Process," Polymer Composites, 22, 337-353.

38. Sommerscales, J. (2004). "The Effect of Permeant on the Measured Permeability of a Reinforcement," 7th International Conference on Flow Processes in Composite Materials, 471-475.

39. Steenkamer, D.J., D.J.Wilkins and V.M. Karbhari (1993). Influence of Test Fluid on Fabric Permeability Measurements and Implications for Processing of Liquid Molded Composites," Jounal of Material Science Letters, 12, 971-973.

40. Luo, Y., I. Verpoest, K. Hoes, M. Vanheule, H. Sol and A. Cardon (2001). "Permeability Measurement of Textile Reinforcements with Several Test Fluids," Composites: Part A, 32, 1497-1504.

41. Hammond, V.H. and A.C. Loos (1997). "The Effects of Fluid Type and Viscosity on the Staedy-State and Advancing Front Permeability Behavior of Textile Preforms," Reinforced Plastic Composites, 16(1), 50-72.

42. B.W. Grimsley, P.Hubert, T.H.Hou, R.J.Cano, A.C.Loos, R.B.Pipes (2001). "Matrix Characterization and Development for the Vacuum Assisted Resin Transfer Molding Process," 16th ASC Technical Conference, CD-ROM.

43. H. Lee and K. Neville (1967). *Handbook of Epoxy Resins*, McGraw-Hill Book Company, New York, 5.2-5.13.

44. George Odian (1991). *Principles of Polymerization*, John Wiley and Sons, New York, 134.

45. K.J. Saunders (1988). *Organic Polymer Chemistry*, Chapman and Hall, London, 1988, 424-427.

46. Lee, W.I., A.C. Loos and G.S. Springer (1982) "Heat of Reaction, Degree of Cure, and Viscosity of Hercules 3501-6 Resin," Journal of Composite Materials, 16, 511-520

47. Yousefi, A., P.G. Lafleur and R. Gauvin (1997). "Kinetic Studies of Thermoset Cure Reactions: A Review," Polymer Composites, 18(2), 157-167.

48. Hubert, P., A. Johnston, A. Poursartip and K. Nelson, (2001). "Cure Kinetics and Viscosity Models for Hexcel 8552 Epoxy Resin," SAMPE International Symposium Proceedings, 46, 23-41.

49. Hou, T.H., J.Y. Huang and J.A. Hinckley (1990). "Chemorology of an Epoxy Resin System under Isothermal Curing," Journal of Applied Polymer Science, 41, 819-834.

50. G. Fernlund, A. Poursartip, K. Nelson, M. Wilenski and F. Swanstrom, 1999. "Process Modeling for Dimensional Control – Sensibility Analysis of a Composite Spar Process," SAMPE International Symposium Proceedings, 44, 1744.

51. Williams, C., J. Sommerscales, and S. Grove (1996). "Resin Infusion Under Flexible Tooling (Rift): A Review," Composites Part A: Applied Science and Manufacturing, 27A, 517-524.

52. Gilbert, E.N., B.S. Hayes, and J.C. Seferis (2001) "Charcterization of VARTM Resin Candidates for Commercial Airplane Applications," SAMPE International Technical Conference Proceedings,

53. Brouwer, W.D., E.C. VanHerpt, and M. Labordus (2003). "Vacuum Injection Moulding for Large Structural Applications," Composites Part A: Applied Science and Manufacturing, 34A, 551-558.

54. Chen, B. and Chou, T.W. (1999). "Compaction of Woven-fabric Preforms in Liquid Composite Molding Process: Single-Layer Deformation," Composites Science and Technology, 59, 1519-1526.
55. Gama, B.A., H. Li, W. Li, A.Paesano, D. Heider and J.W. Gillespie (2004). "Improvement of Dimensional Tolerances During VARTM Processing," SAMPE International Symposium, 46,
56. Pearce, N. and J. Sommerscales (1995). "The Compressibility of a Reinforcement Fabric," Composite Manufacturing, 6, 15-21.
57. Kelly, P.A., R. Umer, and S. Bickerton (2005). "Viscoelastic Response of Dry and Wet Fibrous Materials During Infusion Processes," Composites Part A: Applied Science and Manufacturing, (in press).
58. Terzaghi, K. and R. Peck (1943). ***Soil Mechanics in Engineering Practice,*** John Wiley and Sons, New York.

Appendix

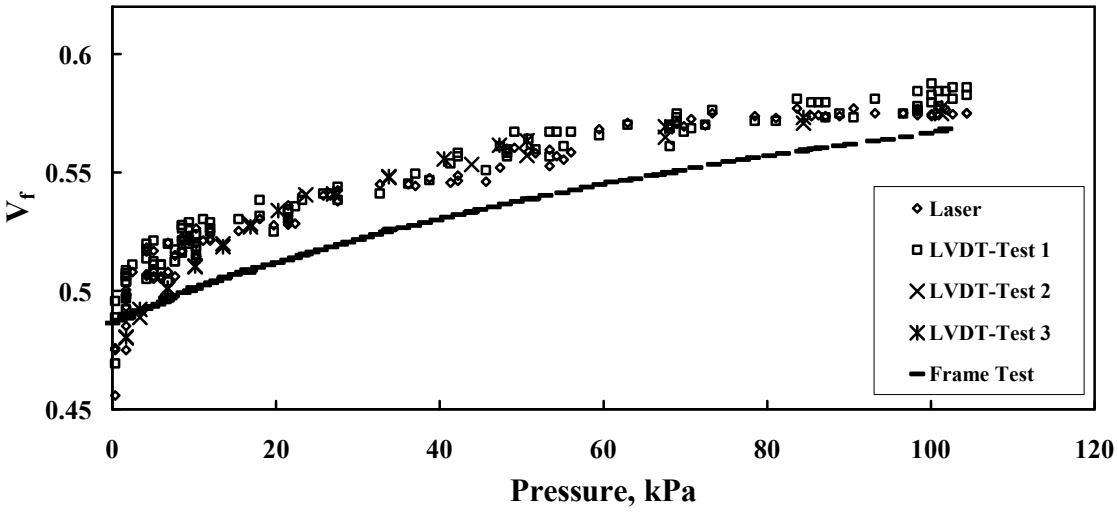

Figure A1: Dry compaction results for MAWK one stack.

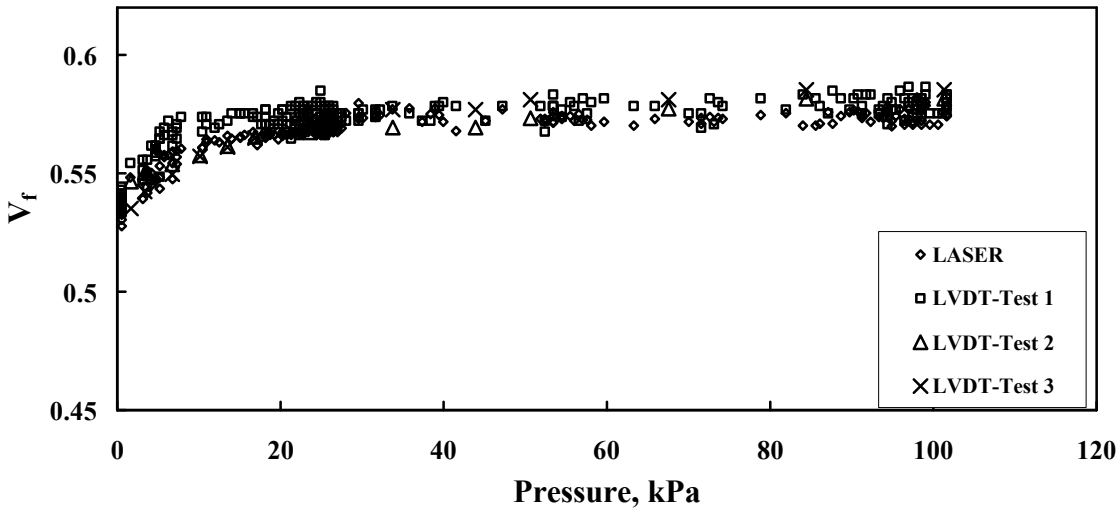

Figure A2: Wet unloading results for MAWK one stack.

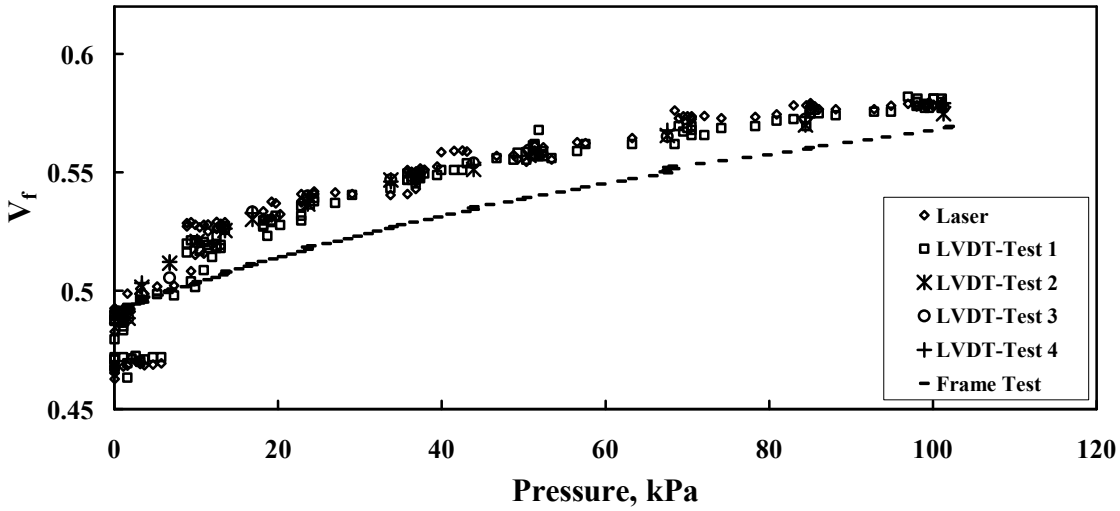

Figure A3: Dry compaction results for MAWK two stacks.

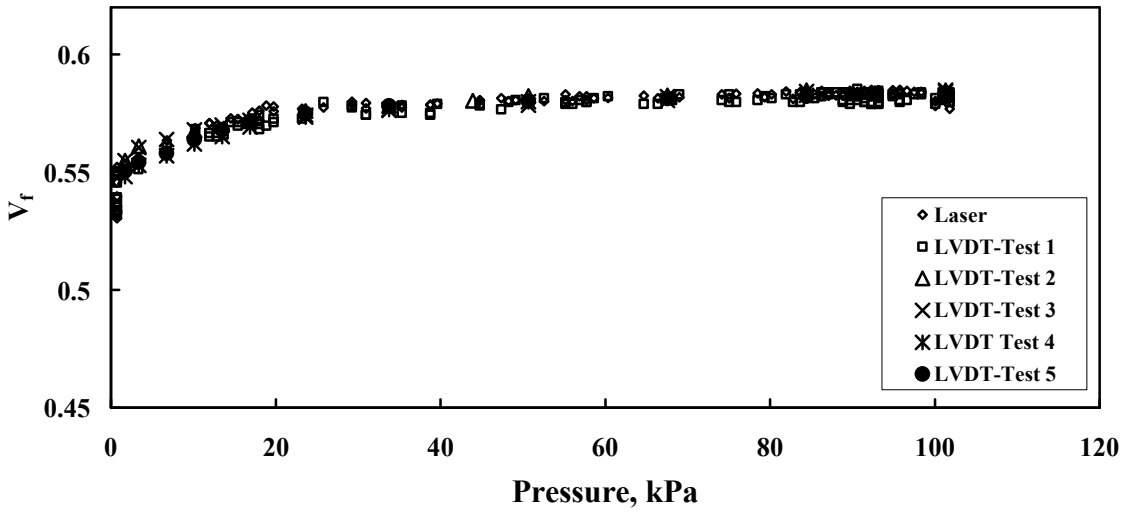

Figure A4: Wet unloading results for MAWK two stacks.

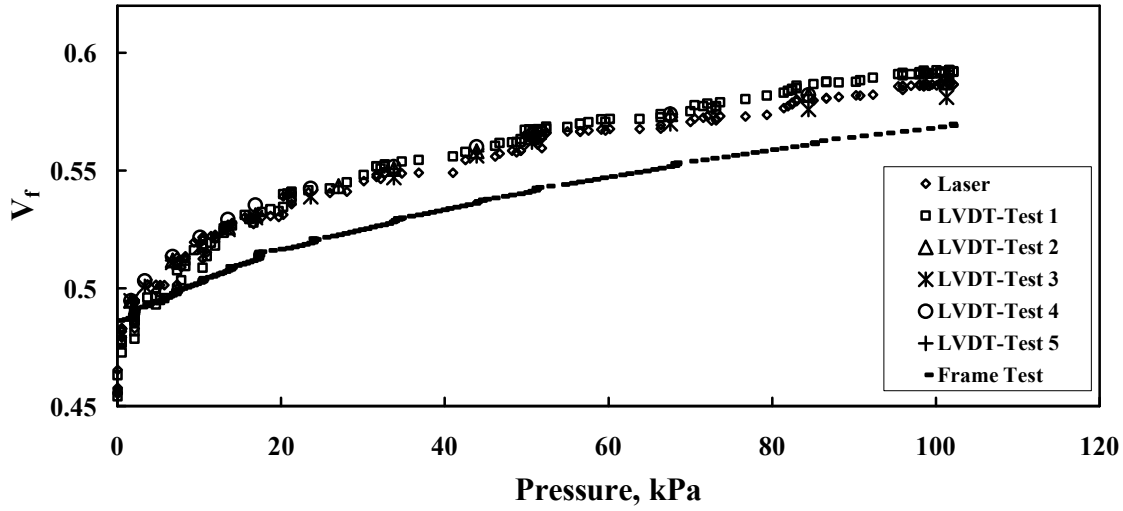

Figure A5: Dry compaction results for MAWK four stacks.

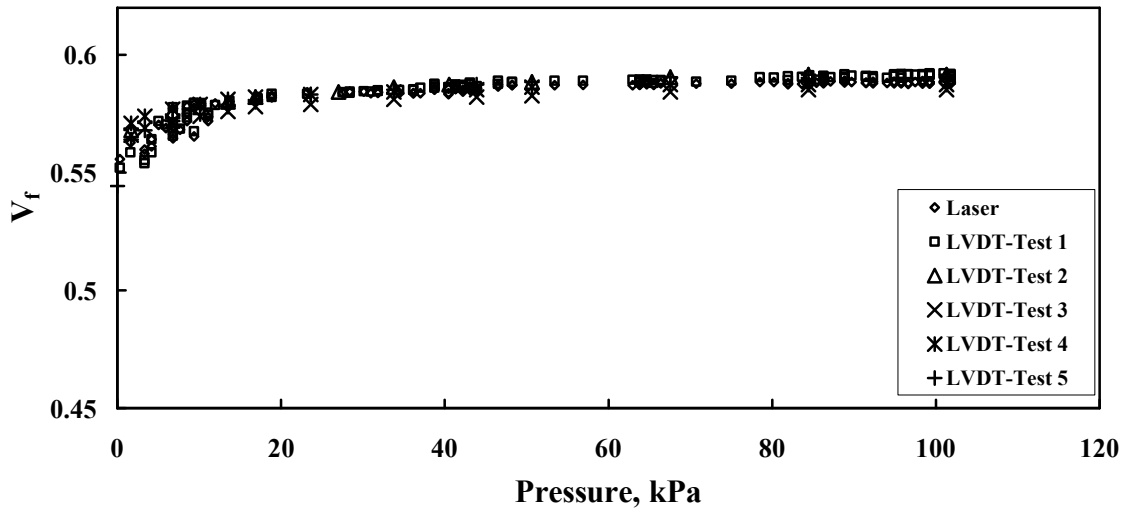

Figure A6: Wet unloading results for MAWK four stacks.

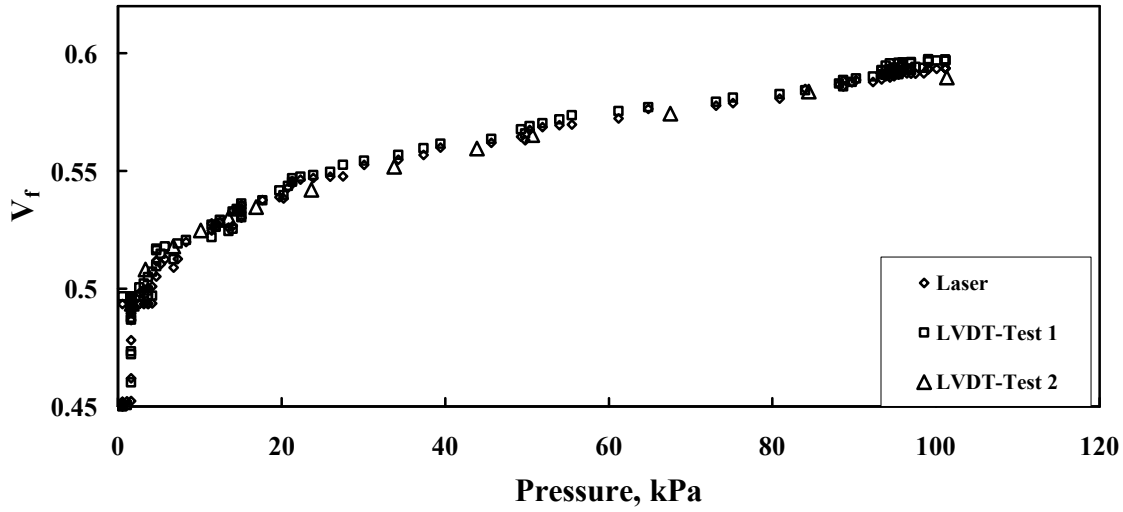

Figure A7: Dry compaction results for MAWK eight stacks.

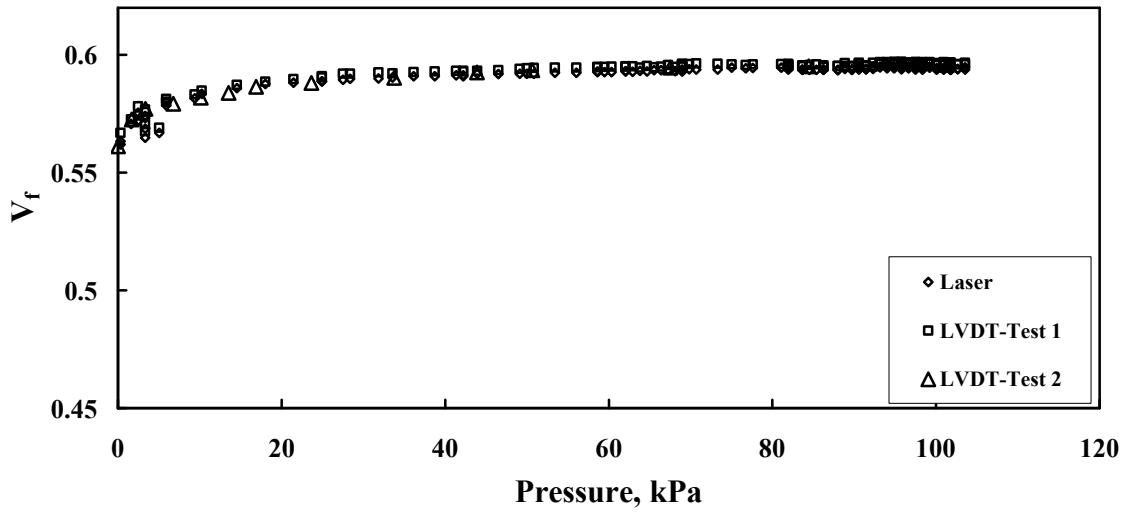

Figure A8: Wet unloading results for MAWK eight stacks.

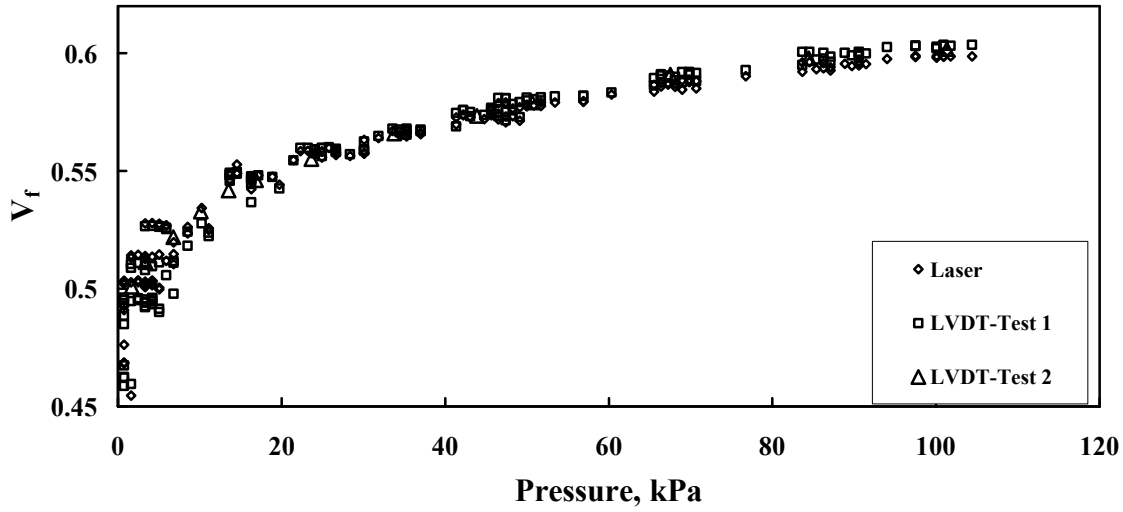

Figure A9: Dry compaction results for MAWK sixteen stacks.

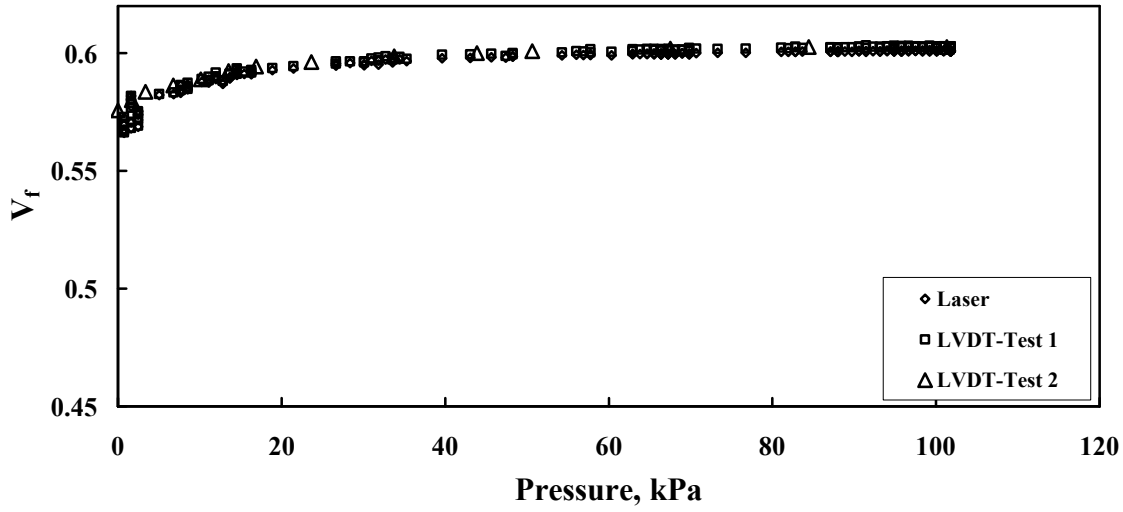

Figure A10: Wet unloading results for MAWK sixteen stacks.

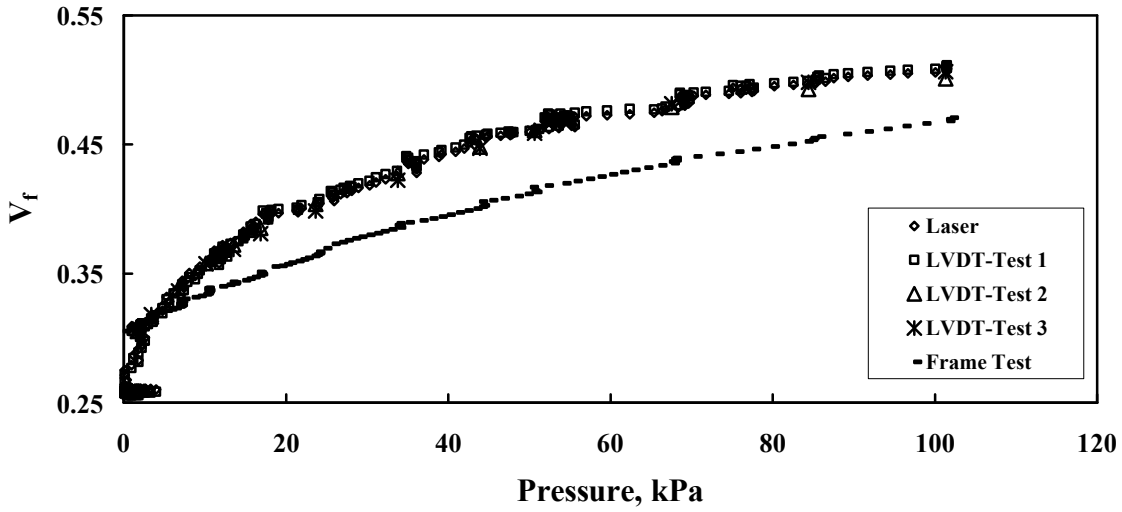

Figure A11: Dry compaction results for biaxial 10-layers.

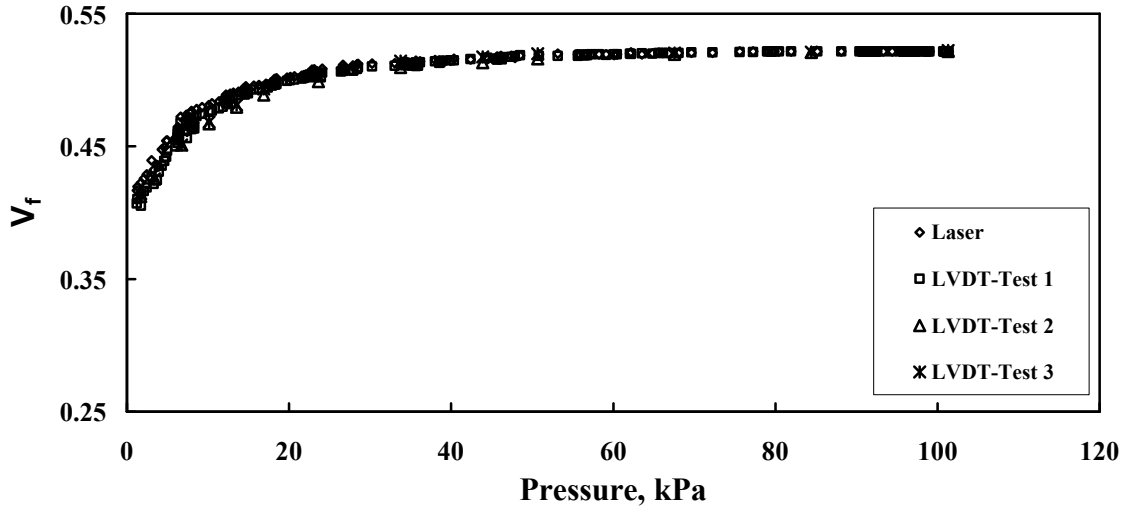

Figure A12: Wet unloading results for biaxial 10-layers.

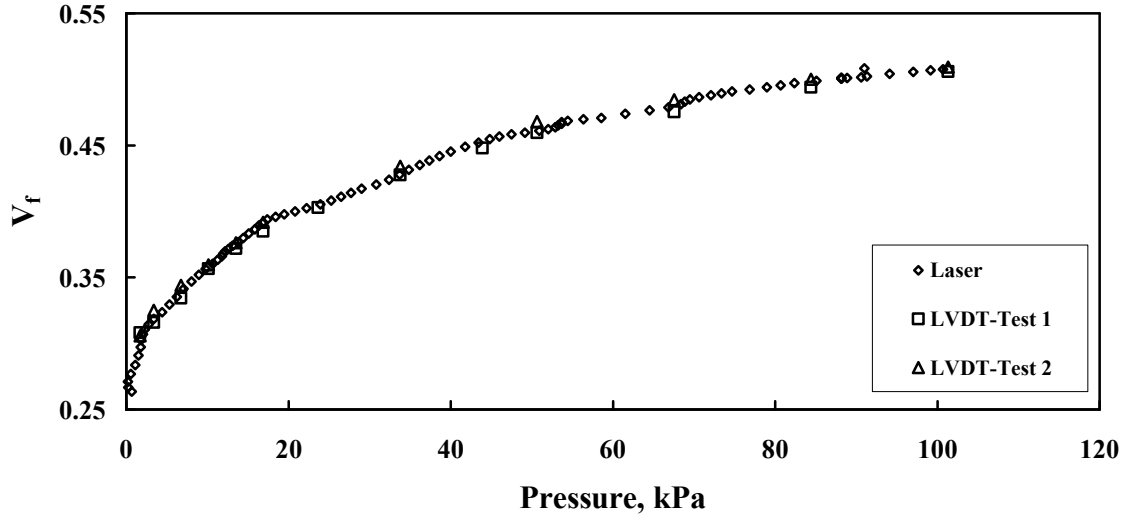

Figure A13: Dry compaction results for biaxial 20-layers.

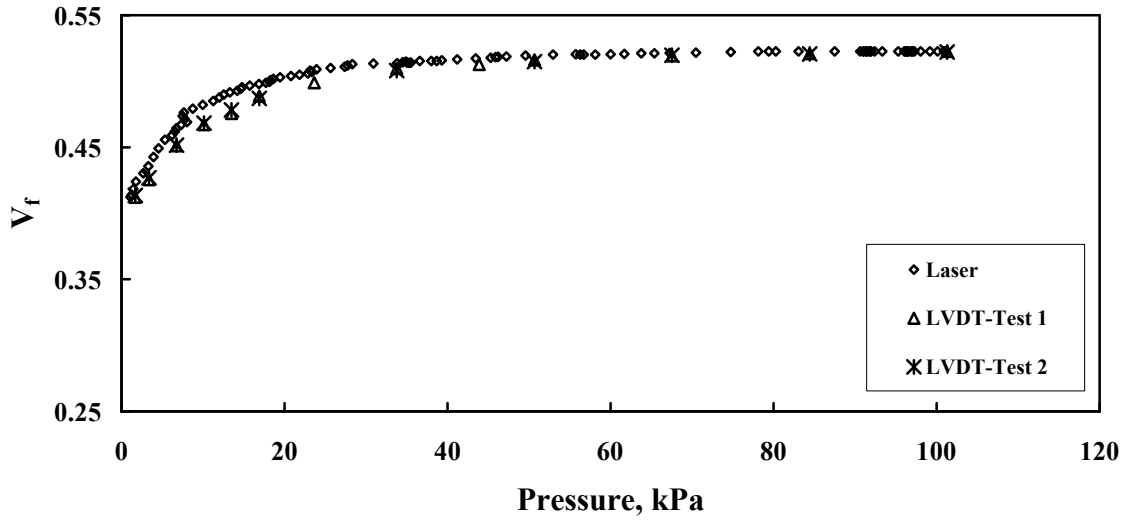

Figure A14: Wet unloading results for biaxial 20-layers.

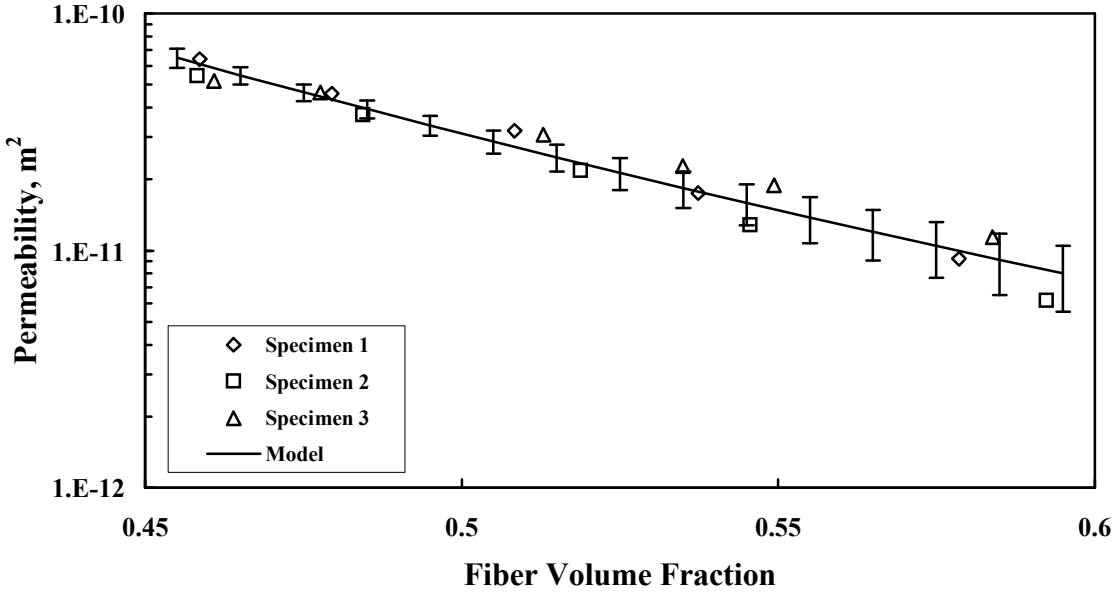

Figure A15: Measured in-plane permeability, S_{xx}, as a function of fiber volume fraction and resulting empirical model curve fit analysis for MAWK – one stack.

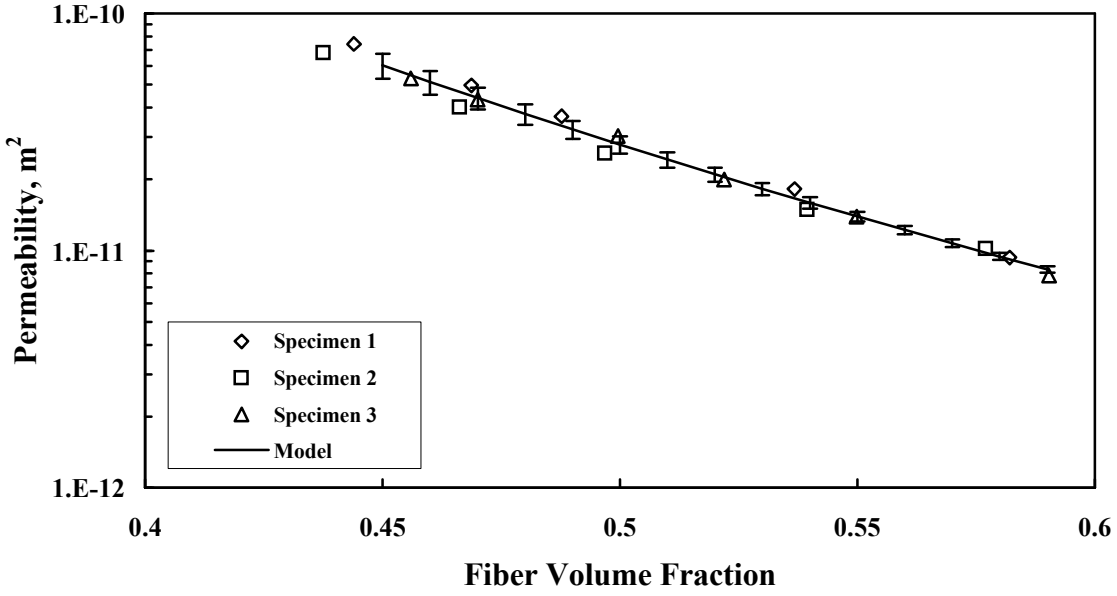

Figure A16: Measured in-plane permeability, S_{xx}, as a function of fiber volume fraction and resulting empirical model curve fit analysis for MAWK – two stacks.

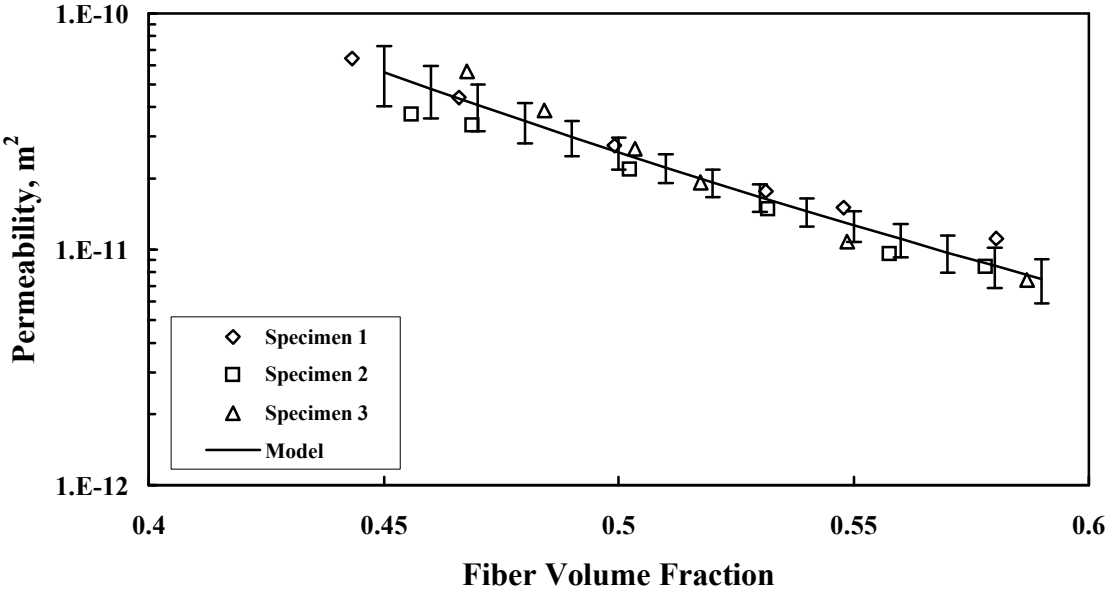

Figure A17: Measured in-plane permeability, S_{xx}, as a function of fiber volume fraction and resulting empirical model curve fit analysis for MAWK – four stacks.

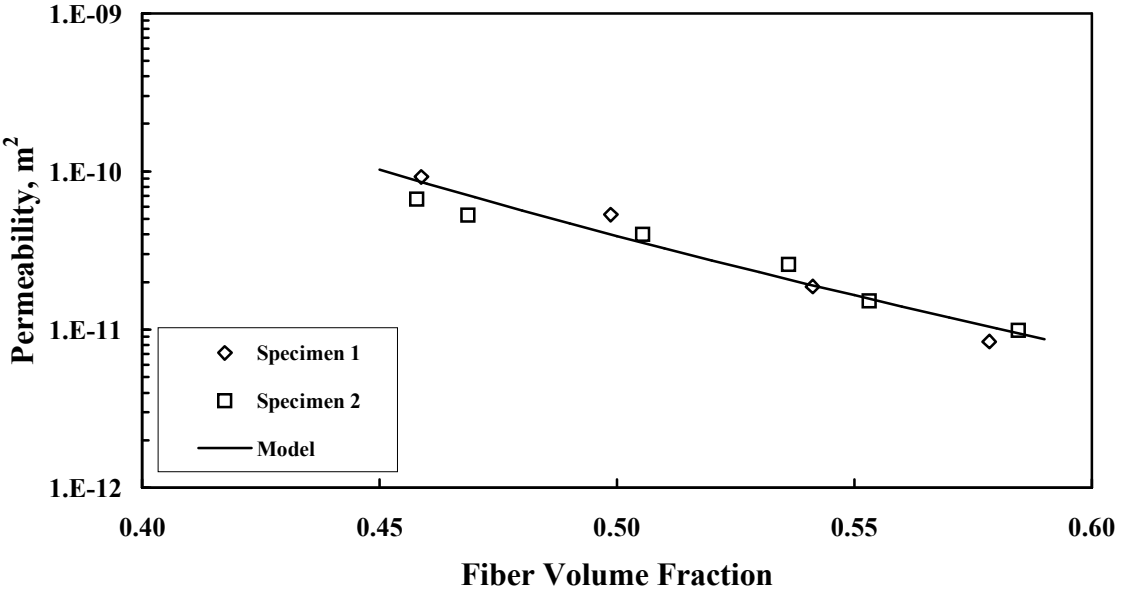

Figure A18: Measured in-plane permeability, S_{xx}, as a function of fiber volume fraction and resulting empirical model curve fit analysis for MAWK – eight stacks.

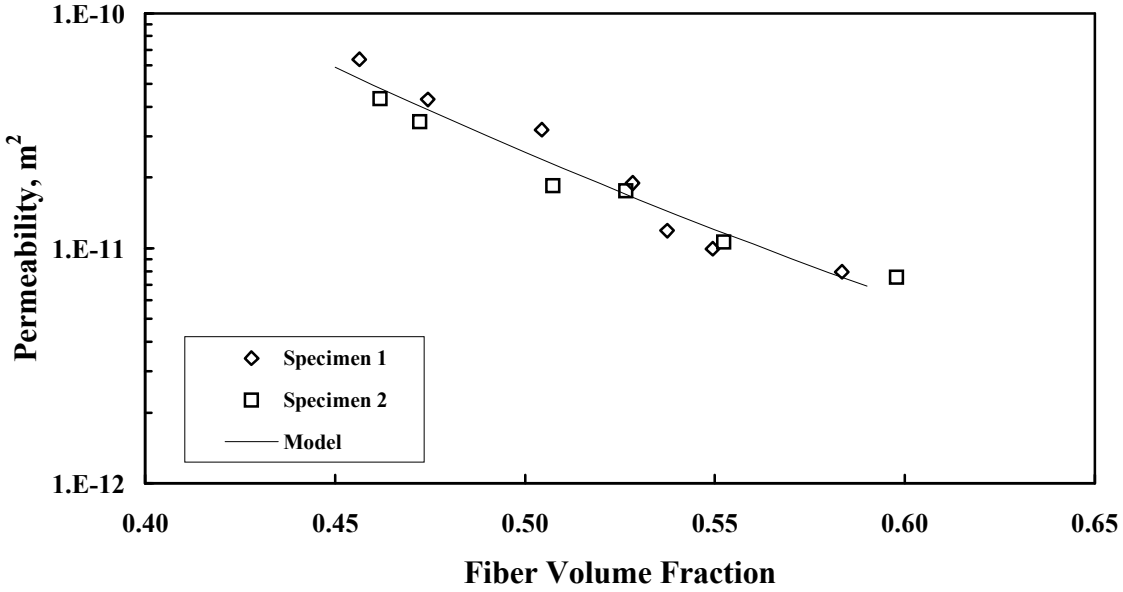

Figure A19: Measured in-plane permeability, S_{xx}, as a function of fiber volume fraction and resulting empirical model curve fit analysis for MAWK – sixteen stacks.

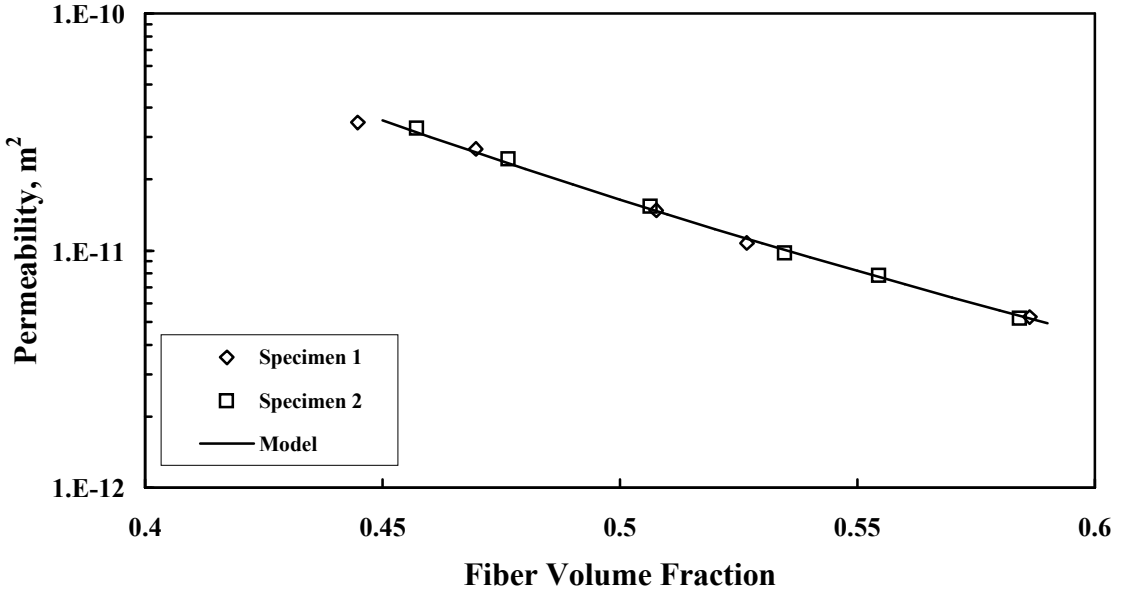

Figure A20: Measured in-plane permeability, S_{yy}, as a function of fiber volume fraction and resulting empirical model curve fit analysis for MAWK – one stack.

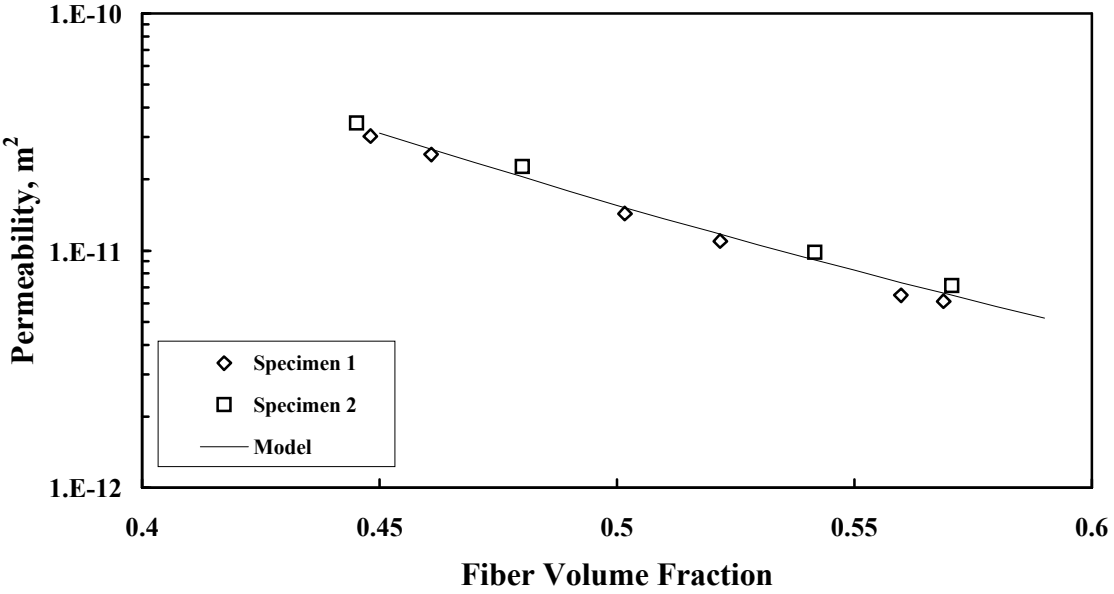

Figure A21: Measured in-plane permeability, S_{yy}, as a function of fiber volume fraction and resulting empirical model curve fit analysis for MAWK – two stacks.

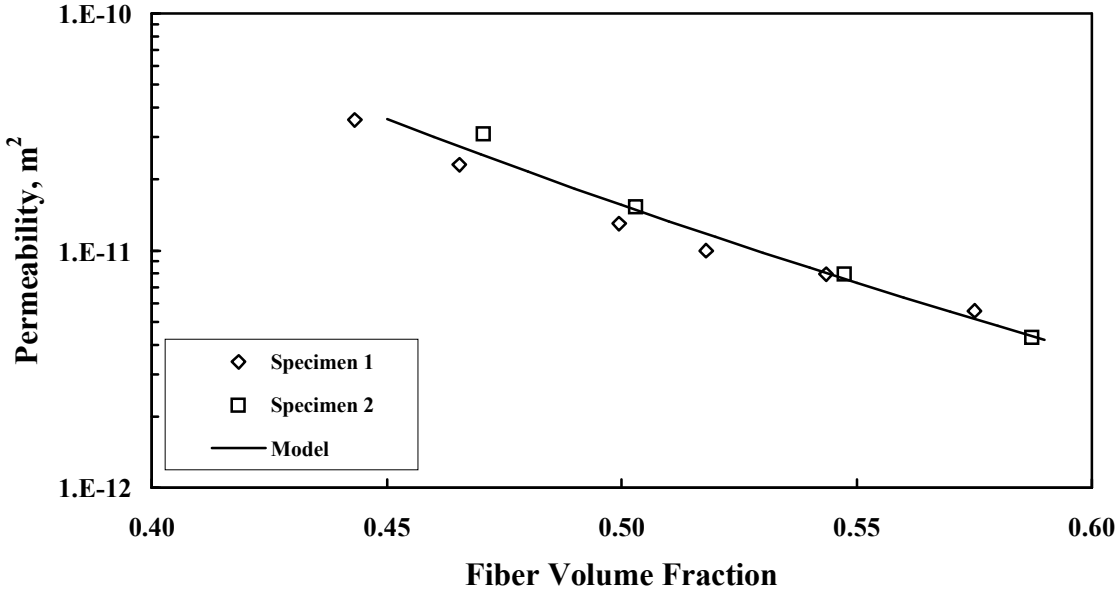

Figure A22: Measured in-plane permeability, S_{yy}, as a function of fiber volume fraction and resulting empirical model curve fit analysis for MAWK – four stacks.

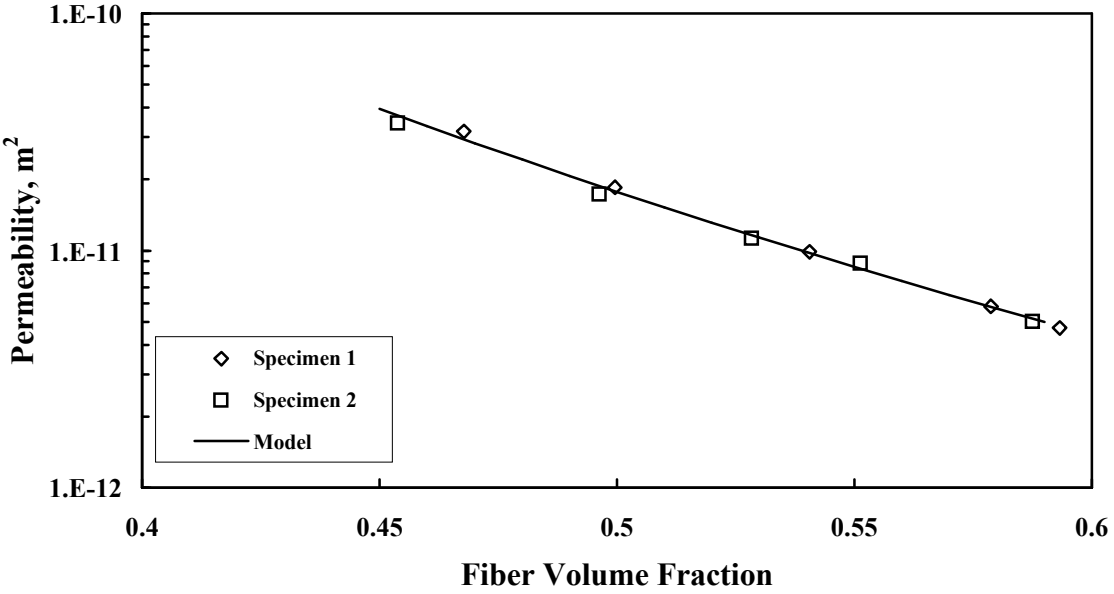

Figure A23: Measured in-plane permeability, S_{yy}, as a function of fiber volume fraction and resulting empirical model curve fit analysis for MAWK – eight stacks.

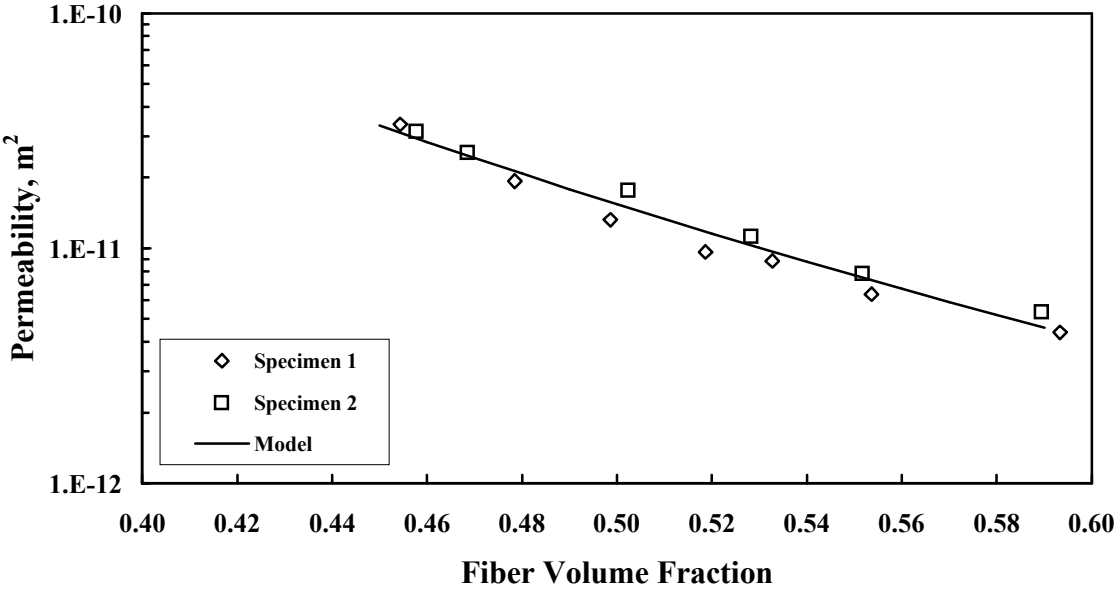

Figure A24: Measured in-plane permeability, S_{yy}, as a function of fiber volume fraction and resulting empirical model curve fit analysis for MAWK – sixteen stacks.

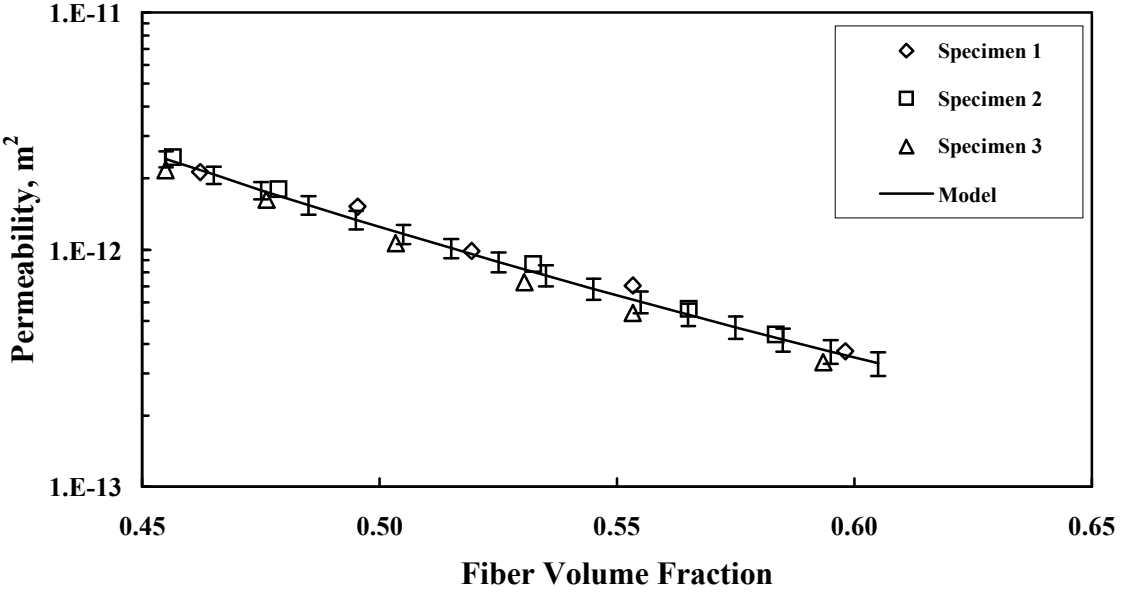

Figure A25: Measured transverse permeability, S_{zz}, as a function of fiber volume fraction and resulting empirical model curve fit analysis for MAWK – one stack.

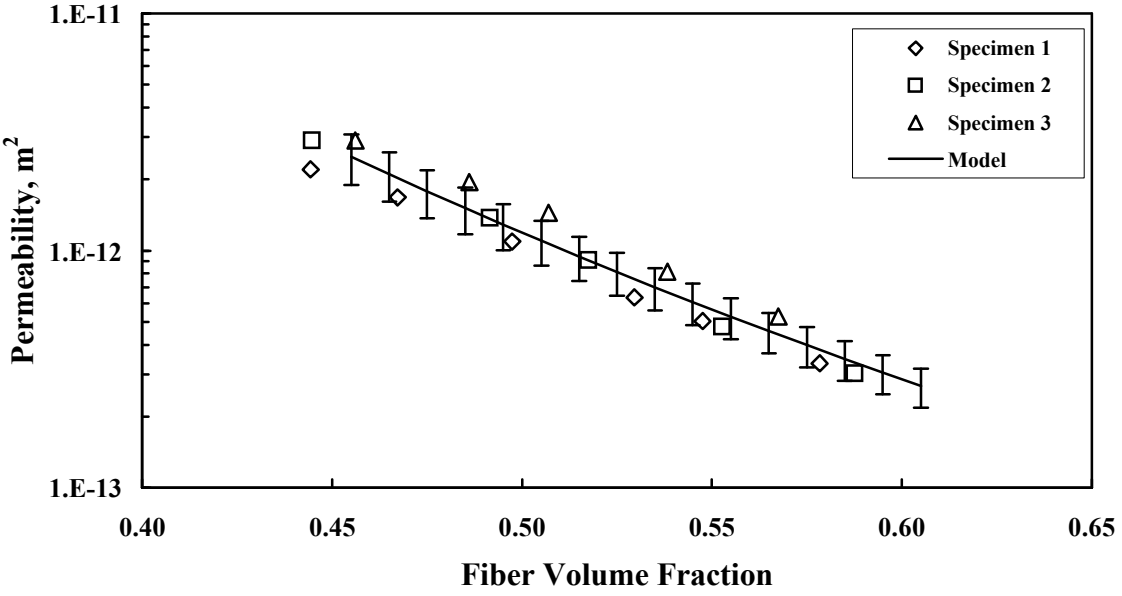

Figure A26: Measured transverse permeability, S_{zz}, as a function of fiber volume fraction and resulting empirical model curve fit analysis for MAWK – two stacks.

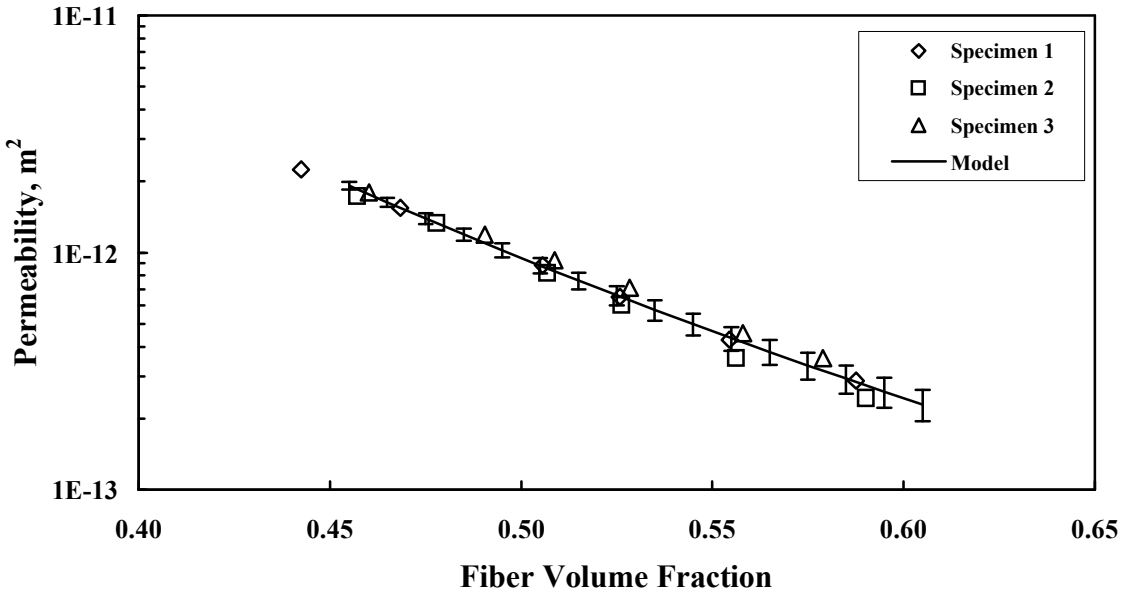

Figure A27: Measured transverse permeability, S_{zz}, as a function of fiber volume fraction and resulting empirical model curve fit analysis for MAWK – four stacks.

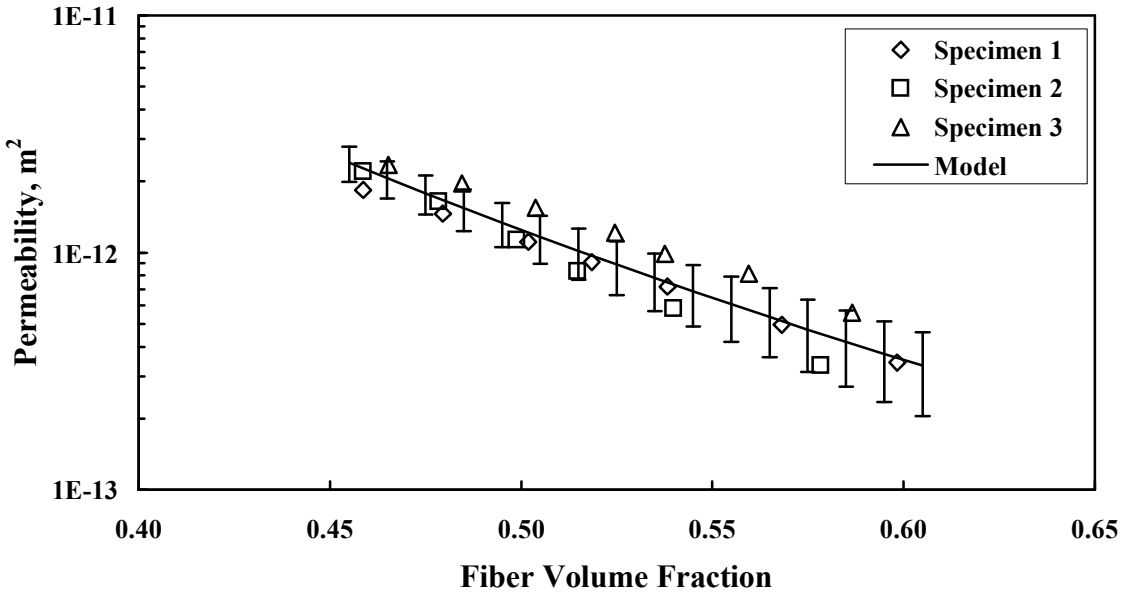

Figure A28: Measured transverse permeability, S_{zz}, as a function of fiber volume fraction and resulting empirical model curve fit analysis for MAWK – eight stacks.

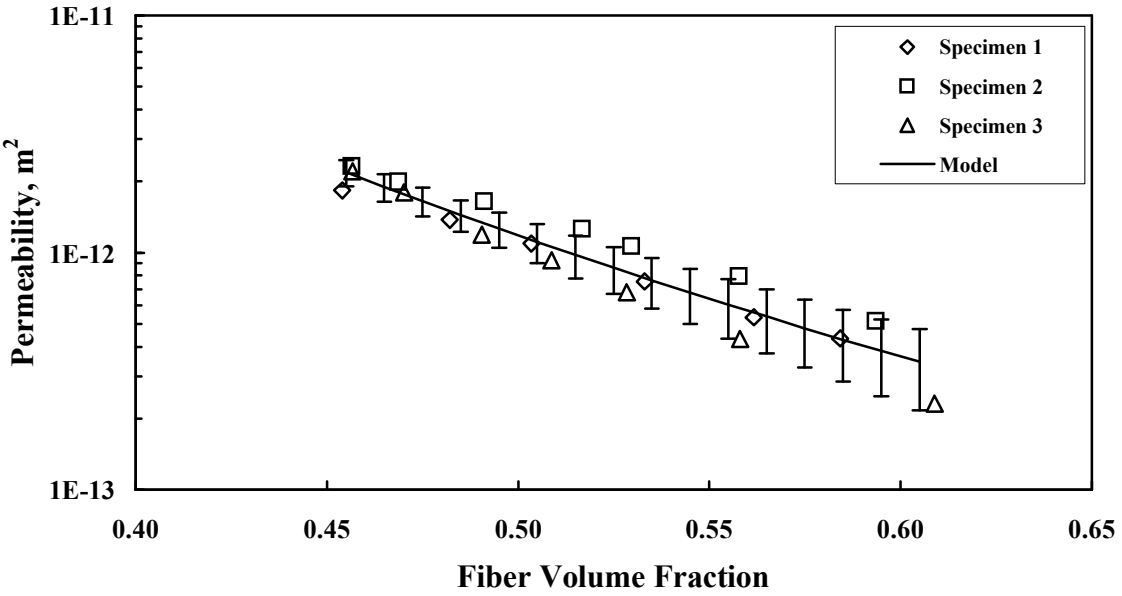

Figure A29: Measured transverse permeability, S_{zz}, as a function of fiber volume fraction and resulting empirical model curve fit analysis for MAWK – sixteen stacks.

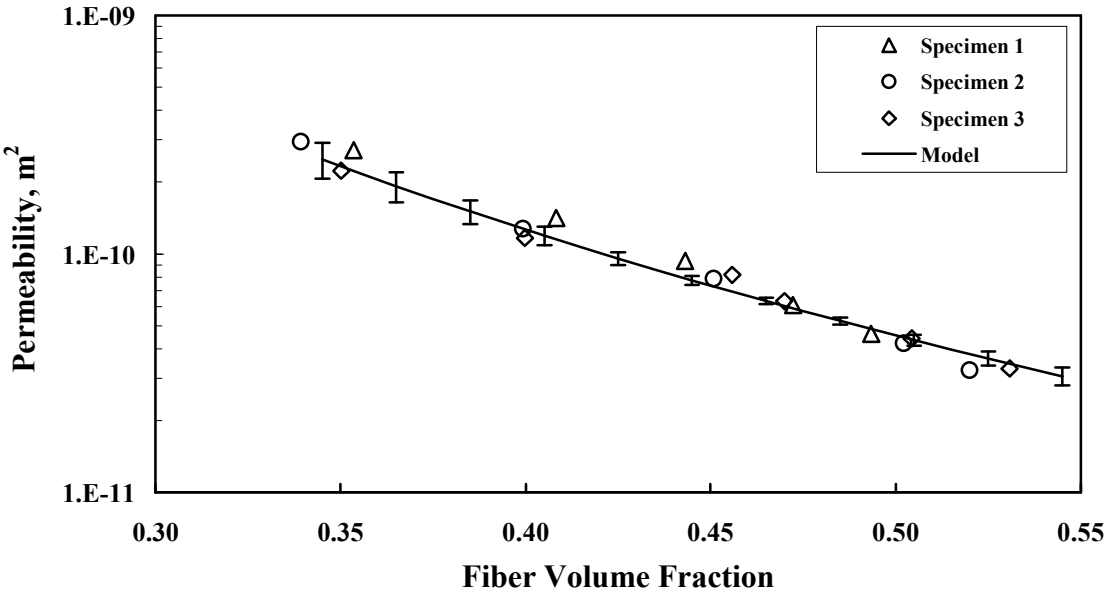

Figure A30: Measured in-plane permeability, S_{xx} or S_{yy}, as a function of fiber volume fraction and resulting empirical model curve fit analysis for biaxial 10-layers.

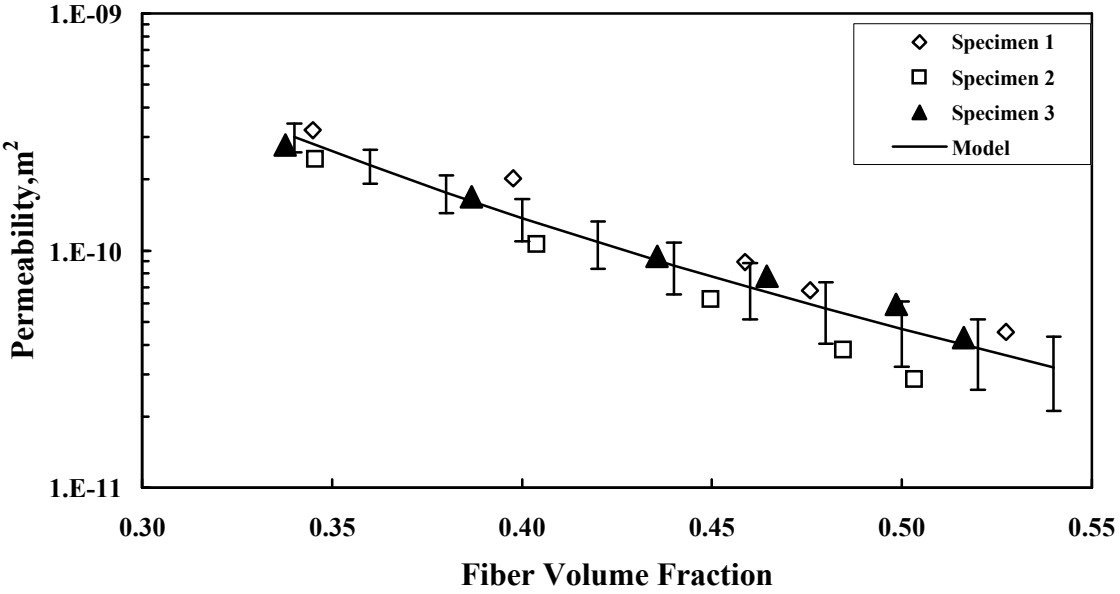

Figure A31: Measured in-plane permeability, S_{xx} or S_{yy}, as a function of fiber volume fraction and resulting empirical model curve fit analysis for biaxial 20-layers.

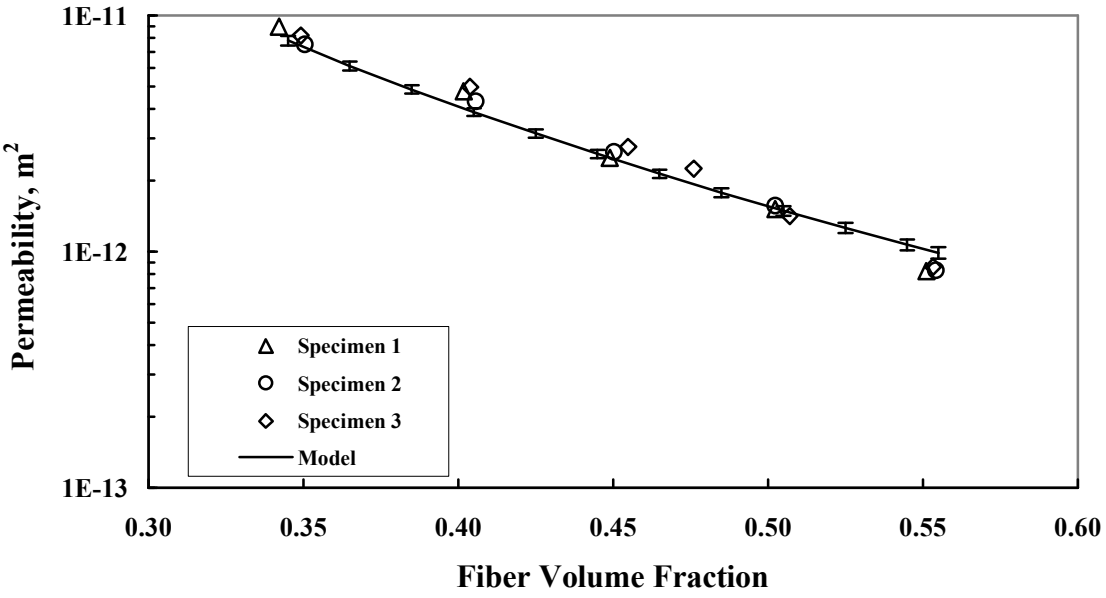

Figure A32: Measured transverse permeability, S_{zz}, as a function of fiber volume fraction and resulting empirical model curve fit analysis for biaxial 10-layers.

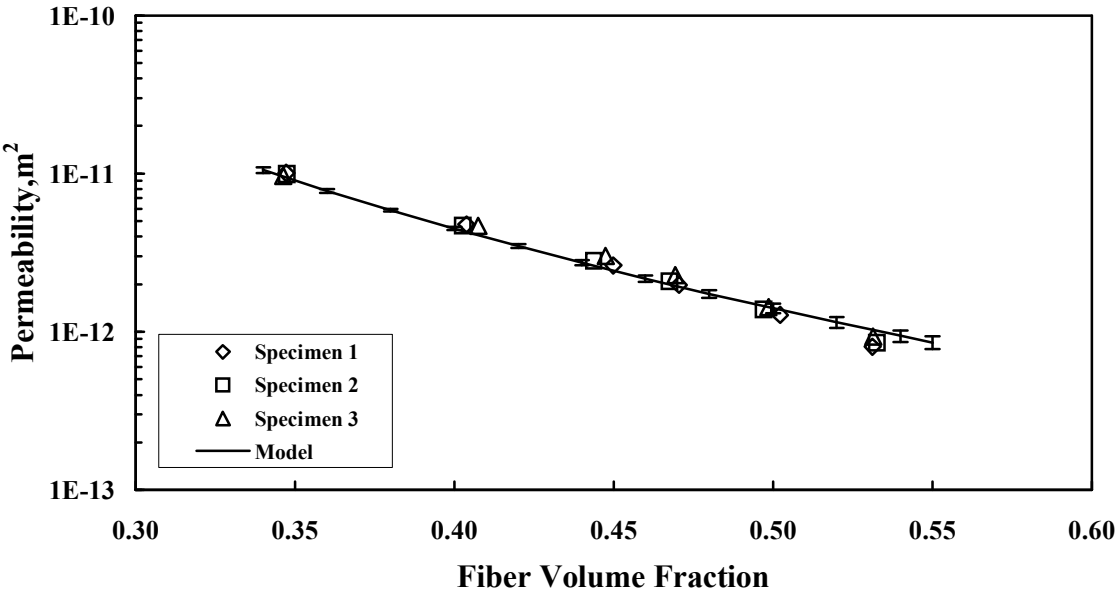

Figure A33: Measured transverse permeability, S_{zz}, as a function of fiber volume fraction and resulting empirical model curve fit analysis for biaxial 20-layers.

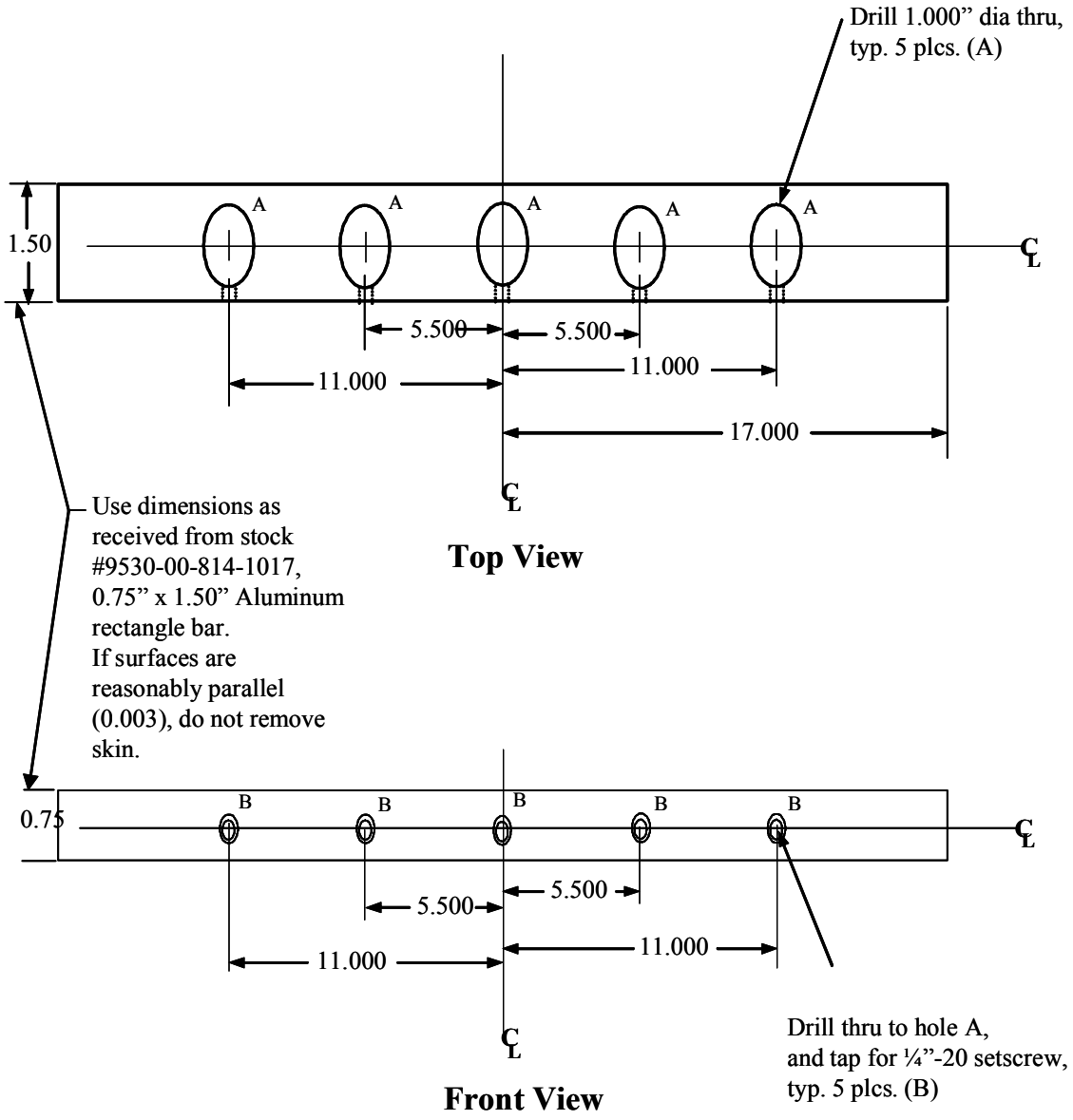

Figure A34: Original shop drawing of instrumented tool LVDT span grip.

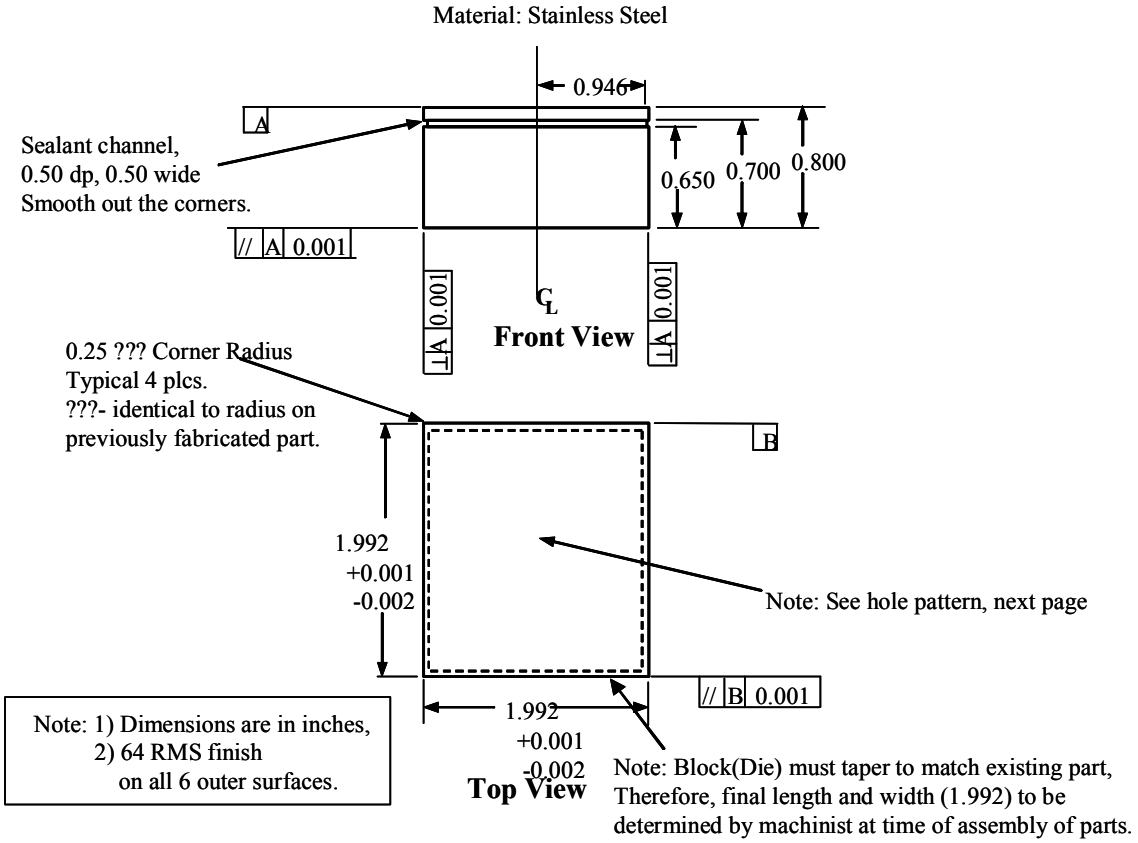

Figure A35: Original shop drawing of transverse permeability fixture shim for one-stack MAWK characterization.

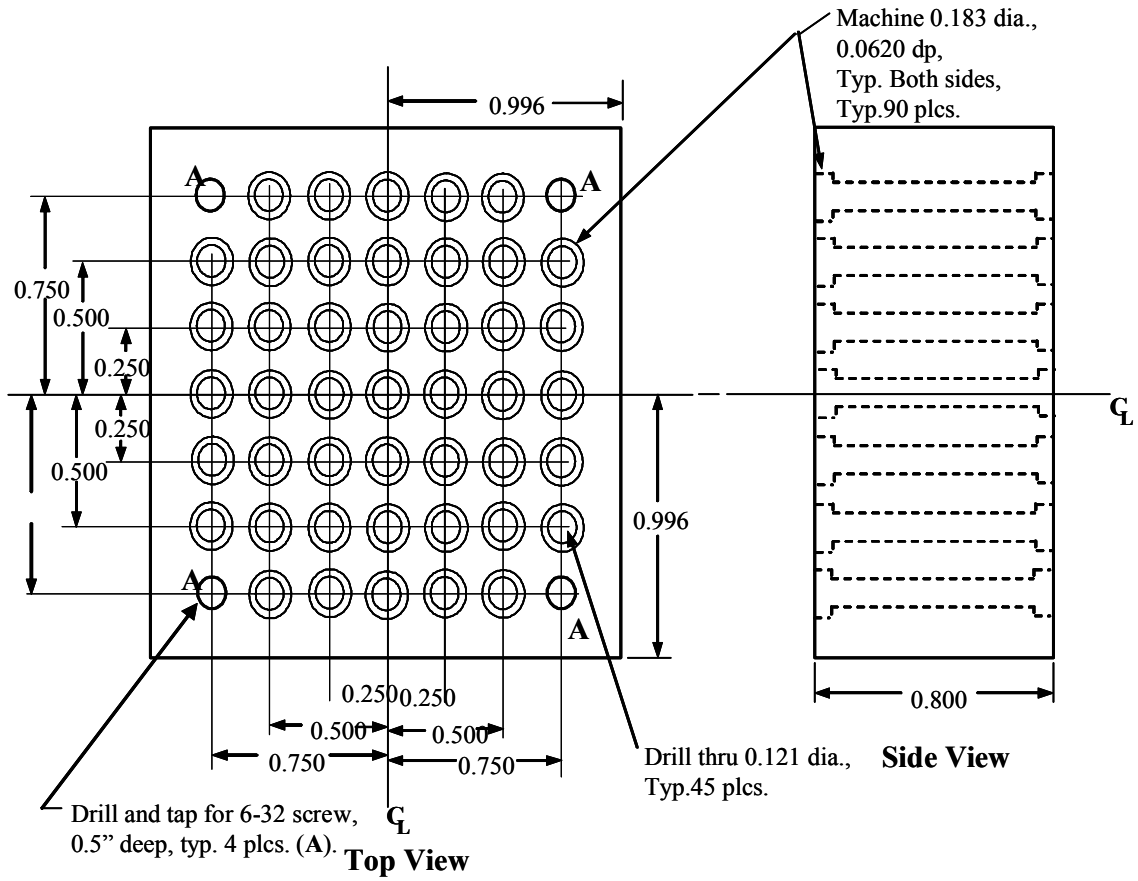

Figure A36: Original shop drawing of of transverse permeability fixture shim hole pattern.

VITA

Brian William Grimsley was born on May 20, 1969 in New London, Connecticut to Roberta A. and George M. Grimsley. He lived in the Tidewater area of Virginia for almost 33 years graduating from Denbigh High School in Newport News. He obtained his Bachelor of Science in Mechanical Engineering from Old Dominion University in Norfolk, Virginia in 1999. In 1997, he was hired under a research grant to work at the NASA Langley Research Center in Hampton, Virginia. For the next eight years, he worked on various projects at NASA to develop and characterize materials for aerospace vehicles. He was married to Stacey J. Thompson on May 20th of 2000 in Norfolk. Brian and Stacey were blessed with the birth of their daughter Olivia Lucille Grimsley on May 29th of 2004. Olivia, Stacey, and Brian currently live in Scottsdale, Arizona, where Brian works as a package development engineer for Intel Corporation.